Coherence and collective oscillations of a two-component Bose-Einstein condensate

Mikhail Egorov

Centre for Atom Optics and Ultrafast Spectroscopy

Swinburne University of Technology, Melbourne, Australia.

A thesis submitted for the degree of Doctor of Philosophy.

March 2, 2012

Coherence and collective oscillations of a two-component Bose-Einstein condensate

Mikhail Egorov

Centre for Atom Optics and Ultrafast Spectroscopy
Swinburne University of Technology, Melbourne, Australia.

A thesis submitted for the degree of Doctor of Philosophy.

Supervisory Committee:
Professor Andrei Sidorov (chair),
Doctor Brenton Hall,
Professor Peter Hannaford.

Abstract

Ultracold atoms and Bose-Einstein condensates represent a burgeoning and ever exciting area of research which has produced numerous breakthroughs in the last 15 years. Ultracold atoms at nano-Kelvin temperatures, isolated in atom traps from the hot, room temperature environment, exhibit ultimate quantum properties and can serve as pure samples for testing quantum mechanics and performing precision measurements. The research described in this thesis investigates, both theoretically and experimentally, the coherence and dynamical evolution of a two-component Bose-Einstein condensate (BEC). The studies are performed on the $|1\rangle \equiv |F = 1, m_F = -1\rangle$ and $|2\rangle \equiv |F = 2, m_F = +1\rangle$ hyperfine ground states of a ^{87}Rb BEC trapped on an atom chip.

Conventional understanding has been that the fringe contrast in interferometric experiments on a BEC is limited by the mean-field dephasing due to strong interatomic interactions which lead to inhomogeneous collisional shifts. We have discovered using Ramsey interferometry a mean-field driven self-rephasing effect in a trapped two-component BEC. When combined with a spin-echo technique, we find that the self-rephasing leads to a coherence time of 2.8 s, the longest ever recorded for an interacting BEC.

Secondly, we have developed a new technique based on periodic collective oscillations for precision measurements of the interspecies and intraspecies scattering lengths and derived an analytic mean-field theory for the phase and density dynamics in the two-component BEC. This technique has been applied to the measurements of the scattering lengths for the two components, $|1\rangle$ and $|2\rangle$, in ^{87}Rb with a precision of 0.016%. Additionally, the two-body loss coefficients for these states have been measured.

Thirdly, we have developed and applied a new, interferometric method for calibrating the detection system, in order to determine the total atom number precisely for Ramsey interferometric measurements. The calibration coefficient is found to be in a good agreement with that obtained using a conventional calibration technique based on the critical BEC temperature.

Finally, we have detected predicted RF-induced Feshbach resonances by monitoring changes in the two-body loss coefficients in the two-component BEC. Conventional Feshbach resonances have been used in many works to tune the s-wave interactions; however, there is no achievable magnetic Feshbach resonance for magnetically trappable states of ^{87}Rb. The RF-induced resonances which we have detected can provide a way to tune the scattering lengths which is important for interferometry and entanglement experiments. The positions of the resonances may provide useful information for predicting the atomic scattering properties of ^{87}Rb.

Acknowledgements

During the completion of this project, I had the valuable help and support of various people.

First of all, I would like to thank Prof. Andrei Sidorov, who has been the primary supervisor, providing the vital guidance and help in the project. Andrei provided the crucial help in writing this thesis and articles reporting the research results in scientific journals or conferences. His contribution was extremely important for me to develop researcher skills. Apart from being an excellent scientist and project leader, Andrei always was a very kind and supportive person.

The help of Prof. Peter Hannaford was also extremely important. Apart from very useful discussions about the project, Peter provided vital help in writing articles, conferences abstracts and the thesis. Without his help the thesis would not be as well readable as it is now. Also Peter always taught and showed a good example how to communicate well with people and to be a real gentleman.

I thank Dr. Brenton Hall for his timely help with the experimental setup. His help with writing articles and the thesis was also very important. Apart from that, Brenton has provided many interesting ideas about the experiment, for example, the development of the interferometric technique for atom number calibration was encouraged mainly by him.

It is hard to describe the importance of the help of the PhD student who worked on this experiment previously, Dr. Russell Anderson. Russell taught me how to operate the experiment. He provided the idea of using a spin echo technique for BECs, and we implemented that together. This made possible the achievement of very long coherence

times with trapped BECs. Russell continued to help after moving to Monash University and provided extremely useful help with the theory of RF-induced Feshbach resonances.

I would also like to thank Dr. Shannon Whitlock who built the experimental setup together with Andrei and Brenton in the past. Shannon devoted a couple of months of his time to collaboration with CAOUS and helped with virtually all the ultracold experiments in our Centre. For this particular work, Shannon provided the idea of fringe removal by the "eigenface" method and showed how the analytical description of two-component BEC dynamics can be derived. He showed a good example of how researchers should collaborate with different groups.

Prof. Peter Drummond helped a lot with the rephasing article and made many useful suggestions about the theory behind the experiment. I would like to thank him for many useful discussions on the topics of the thesis.

Next, I thank the current PhD students, theorists and experimentalists, who work with the experiment and its theoretical description at the moment. Bogdan Opanchuk created a fast simulator of the BEC dynamics employing the power of GPU computing; without that most of the experimental data in this thesis would not have been processed as effectively. Valentin Ivannikov worked on the experiment together with me, always helping to fix all the issues that appeared; he also made valuable contributions to the rephasing article. Iurii Mordovin, a new PhD student, has managed to learn how to operate the experiment very quickly and continues with the further development of this work.

I would also like to thank Prof. Russell McLean, Smitha Jose, Ba Khuong Dinh, Dr. Leszek Krzemien and Mark Kivinen for their support. I devote special thanks to Evelyn Cannon who helped me and my wife with our baby near the end of my PhD; I appreciated this help very much.

It is hard to overestimate the help of my wife Anna who devoted all of these three years to providing support during this important period. The whole PhD would not have been possible without that help.

Declaration

I declare that this thesis

- contains no material which has been accepted for the award of any other degree or diploma;
- to the best of my knowledge, contains no material previously published or written except where the reference is given;
- the thesis discloses the relative contributions of collaborators in the case of joint research.

Mikhail Egorov _____

Date _____

Contents

List of Figures

Chapter 1

Introduction

1.1 Physics with two-component condensates

A Bose-Einstein condensate (BEC) is a state of a bosonic gas where a large fraction of atoms occupy the lowest quantum state. In a BEC, the de Broglie wavelength of the atoms becomes comparable to the interatomic separation and indistinguishable bosons form a macroscopic matter wave if the temperature of the Bose-gas is lower than the critical temperature, similar to the processes which occur in superfluid liquid ^{4}He. The first observation of Bose condensation in dilute cold atomic vapours was realised in 1995 by the groups of Eric Cornell and Carl Wieman [1] and Wolfgang Ketterle [2]. Apart from confirming the original Bose and Einstein prediction, it has provided a unique tool for studying atomic properties and fundamental quantum-mechanical effects. A BEC can be obtained in magnetic traps (time-orbiting potential (TOP) trap [1], Ioffe-Pritchard trap [3], on-chip trap [4, 5, 6]) or optical dipole traps [7] by evaporative cooling techniques starting from laser cooled or buffer-gas cooled [8] atoms.

Inter-particle interactions play an important role in BECs [9]. The strongest interactions in BECs are s-wave interactions. The interaction strength is proportional to the s-wave scattering length which is usually expressed in terms of the Bohr radius a_0. The static and dynamic properties of pure BECs are well described by the Gross-Pitaevskii equation (GPE) [10]. The s-wave interactions determine the size of the BEC

ground state which is well described by the Thomas-Fermi approximation. Collective oscillation frequencies of BECs are also affected by the s-wave interactions [11]. The interactions also determine the formation of dark [12] and bright [13] solitons in BECs.

Multi-component BECs have a notable place among BEC experiments. The group of Eric Cornell made a significant contribution to multi-component BEC physics in the late 1990s. The first two-component BEC composed of ^{87}Rb atoms in the states $|F = 2, m_F = 2\rangle$ and $|1\rangle \equiv |F = 1, m_F = -1\rangle$ was produced in a Ioffe-type magnetic trap by sympathetic cooling [14]. It was first noticed in that work that the intraspecies s-wave scattering length of atoms in state $|1\rangle$ is positive, the rate constant for binary inter-species inelastic collisions was measured and it was observed that there is a repulsive interaction between two components. Later, Cornell's group produced a BEC in state $|1\rangle$ and transferred all atoms to state $|2\rangle \equiv |F = 2, m_F = 1\rangle$ by two-photon microwave and radiofrequency radiation [15], as was originally proposed in theoretical work [16]. This process rapidly changed inter-particle interactions through a difference in the scattering length of the two states. It was changed from a_{11}, the scattering length characterizing collisions between $|1\rangle$ atoms, to a_{22}, the scattering length for collisions between atoms in state $|2\rangle$, and excited ringing in the BEC width. The quantum dynamics of a two-component BEC was first observed in the same group in 1998 [17]. Half of the condensed ^{87}Rb atoms initially prepared in the $|1\rangle$ state were transferred into the $|2\rangle$ state. The dynamics was significantly damped and the two-component BEC quickly relaxed to its ground state, where the component $|2\rangle$ was surrounded by a shell of the component $|1\rangle$. This result implies that a two-component BEC with atoms in states $|1\rangle$ and $|2\rangle$ is immiscible. The dynamics of two macroscopic wavefunctions describing the evolution of both components was simulated by solving coupled Gross-Pitaevskii equations. However the simulations showed that the dynamics should not be damped for a pure BEC [18]. The damping present in the experiment might be explained by finite temperature effects in the BEC. Later on, in David Hall's group the collective oscillations in a two-component BEC composed of states $|1\rangle$ and $|2\rangle$ without significant damping were first observed [19].

The phase dynamics of two-component BECs is no less important than the number

density dynamics. The evolution of the relative phase of the BEC components can be probed by Ramsey interferometry where the coherent superposition of two BECs is created by a preparation, usually $\pi/2$, pulse and the phase information is read out by the second $\pi/2$-pulse. Ramsey interferometry of a two-component BEC was first performed in Cornell's group [20]. The Ramsey fringe frequency measured at different BEC densities [21] allowed one to determine the collisional shift and to measure $a_{11} - a_{22} = 4.85(31)\, a_0$. Also it was confirmed that at the same densities non-condensed atomic clouds have a larger collisional shift than BECs. Spatially non-uniform evolution of the relative phase in a two-component BEC was observed by the Swinburne group in 2009 [22].

In atom interferometry, it is beneficial to have long interrogation times as it allows the sensitivity of an interferometric measurement to be increased. It was believed for a long time that the coherence time in trapped atomic ensembles (condensed or not) is limited by the spatially inhomogeneous collisional shift induced by inter-particle interactions. Indeed, the coherence time in trapped BECs was limited to $\sim$ 200 ms [23] or $\sim$ 0.6 s in a selected central region of a BEC [24]. The reported coherence time in trapped non-condensed ensembles was close to 2 s [21, 25]. Eliminating the collisional shift by tuning the scattering length to zero allowed the visibility of Bloch oscillations in an optical lattice to be maintained for about 11 s [26]. Recently it was discovered that the coherence time in cold, non-condensed ensembles can be prolonged to about 1 minute due to rephasing via the identical spin-rotation effect [27]. We have discovered a completely different mean-field rephasing effect in two-component BECs originated from collective oscillations (Ch. 5). Applying the spin-echo technique [28] simultaneously with the self-rephasing effect, we obtained a coherence time of 2.8 s, the longest coherence time reported for an interacting BEC. Truncated Wigner simulations which include quantum noise showed that the coherence time in the absence of technical noise in this experiment should be more than 10 s [29]. Among all decoherence mechanisms finite temperatures effects are of fundamental importance [30] and require further experimental and theoretical investigations. Our results are published in PRA as a Rapid Communication [31]. The mean-field rephasing mechanism is slightly similar to the mechanism responsible for revival

of Rabi oscillations in a two-component BEC [32].

There has been a number of approaches using different experimental techniques to measure scattering properties of ^{87}Rb in its lowest hyperfine states. The scattering length for the state $|1\rangle$ $a_{11} = 87(21)\,a_0$ was first measured with ultracold atoms using the dependence of the rethermalization rate on the elastic cross-section [33]. The use of this measurement and the results of the first two-component ^{87}Rb condensate for the two-body loss rate in a mixture of states $|1\rangle$ and $|F = 2, m_F = 2\rangle$ [14] allowed one to estimate the singlet and triplet scattering lengths in ^{87}Rb. The two-body loss rate from [14] was also used by Vogels et al. [34] to place bounds on the value of $a_{11} = 106(6)\,a_0$. Later on, inter-atomic interaction potentials and scattering properties of ^{87}Rb were predicted by S. Kokkelmans' group [35] analyzing the results of measurements of highest rovibrational levels in $^{87}Rb_2$ molecules [36], characterization of elastic scattering near a Feshbach resonance in atomic ^{85}Rb [37] and transition frequencies in $^{85}Rb_2$, $^{87}Rb_2$ and ^{85}Rb^{87}Rb molecules [38]. The results reported in [21] are $a_{11} = 100.44\,a_0$, $a_{12} = 98.09\,a_0$ and $a_{22} = 95.47\,a_0$. The theoretical publication [35] also suggests the interspecies two-body loss rate $\gamma_{12} = 1.9 \times 10^{-20}$ cm^3/s and the existence of a weak Feshbach resonance for states $|1\rangle$ and $|2\rangle$ at 1.9 G which, however, hasn't yet been observed. The modelling of inter-atomic interaction potentials was slightly changed recently which led to a change in the calculated scattering lengths: $a_{11} = 100.40(10)\,a_0$, $a_{12} = 98.13(10)\,a_0$ and $a_{22} = 95.68(10)\,a_0$ [39, 40, 41].

Experiments with two-component BECs provided the most precise direct measurements of the ^{87}Rb scattering properties. The difference in the scattering lengths is especially hard to measure because all the scattering lengths in the ^{87}Rb $5^2S_{1/2}$ hyperfine levels are very close to each other. This is explained by the very close values of the singlet and triplet scattering lengths in ^{87}Rb [35]. A number of different approaches were used to measure the ratios or differences in the values of the scattering lengths. The first experiment [15] employed a discontinuous change of the condensate mean-field repulsion [16] via a quick transfer of the entire population from the state $|1\rangle$ into the state $|2\rangle$. This rapid change of the s-wave interaction strength excited residual ringing of the con-

densate width. Comparison of the experimentally obtained width with GPE simulations yielded $a_{11}/a_{22} = 1.062(12)$. Another method employed precision Ramsey interferometry of ultracold ^{87}Rb atoms above and below the condensation temperature performed at the magnetic field $B = 3.23$ G [21]. The measured collisional shift of the transition frequency for both condensates and thermal clouds yielded $a_{22} - a_{11} = -4.85(31)\, a_0$. The scattering properties of different spin states in ^{87}Rb were measured in 2006 by Widera et al. [39] by observation of the coherence in the collisionally driven spin dynamics of ultracold atom pairs trapped in optical lattices. The analysis inferred bare scattering lengths $a_{f=2} - a_{f=0} = -1.07\, a_0$ for atoms in the $F = 1$ lowest hyperfine state and $a_{f=2} - a_{f=0} = 3.51\, a_0$ and $a_{f=4} - a_{f=2} = 6.95\, a_0$ for atoms in the $F = 2$ lowest hyperfine state (lower indices denote channels with total spin f) from Rabi-type oscillations between two spin states. Observation of the non-equilibrium component separation dynamics in the form of oscillating ring-like structures in a binary ^{87}Rb condensate [19] allowed one to deduce the values of scattering lengths $a_{12} = 97.66\, a_0$ and $a_{22} = 95.0\, a_0$ at the magnetic field of 8.32 G by comparing numerically computed and experimentally measured density profiles. Experimental investigations of the time evolution of binary ^{87}Rb condensates were also recently used [42] to characterise the scattering length between the components $|F = 1, m_F = +1\rangle$ and $|F = 2, m_F = -1\rangle$ in the vicinity of a 9.1 G Feshbach resonance in ^{87}Rb.

Atoms in dense ultracold clouds and BECs undergo two-body and three-body collisions. In three-body collisions, atoms are lost due to three-body recombination process; the loss rate in this case is proportional to the cube of the cloud density. In two-body collisions, atoms are lost due to change in their spin-states. The loss rate in two-body collisions is proportional to the density squared in the case of a single component, or to the product of the interacting components densities for mixed spin scattering channels. The coefficient of proportionality is called two-body loss coefficient γ. The two-body loss coefficient can be thought of as the imaginary part of the s-wave scattering length: $\gamma = 2h/\mu\, \mathrm{Im}(a)$, where h is Planck's constant and μ is the reduced mass of two colliding atoms. The group of D. Hall has reported [19] two-body loss coefficients for states $|1\rangle$

and $|2\rangle$: $\gamma_{22} = 1.194(19) \times 10^{-19}$ cm^3/s and $\gamma_{12} = 7.80(19) \times 10^{-20}$ cm^3/s. The two-body loss rates within the state $F = 2$ were recently characterized in the experimental work from Ueda's group [43]; the loss rates reported are $\gamma_{-1,-1} = 1.04(10) \times 10^{-19}$ cm^3/s and $\gamma_{0,0} = 8.9(9) \times 10^{-20}$ cm^3/s for collisions between two atoms with $m_F = -1$ and with $m_F = 0$ Zeeman quantum numbers, respectively.

We have performed precision measurements of the s-wave scattering lengths a_{12} and a_{22} and the two-body loss coefficients in ^{87}Rb (Ch. 6). We have found that when the density of the component $|2\rangle$ is much less than that of $|1\rangle$ and $a_{12} < a_{11}$, the frequency of the collective oscillations in a two-component BEC depends only on trapping potential parameters and the ratio a_{12}/a_{11}. We also derived a one-dimensional theory closely describing the quantum dynamics in this case (Sec. 2.4). This analytic theory predicts the frequency of collective oscillations in a two-component BEC to a very high accuracy, unlike the method based on small perturbations to the Thomas-Fermi two-component ground state [44]. Therefore, we have measured $a_{12} = 98.006(16)\, a_0$ assuming that $a_{11} = 100.40\, a_0$ is known. Relying on the evaluated value of a_{12}, we carried out Ramsey interferometry with $\pi/2$ and $\pi/10$ preparation pulses and determined $a_{22} = 95.44(7)\, a_0$. The measured values of a_{12} and a_{22} are in a good agreement with the first theoretical prediction: $a_{12}^{\mathrm{th}} = 98.09\, a_0$ and $a_{22}^{\mathrm{th}} = 95.47\, a_0$ [21] (Tab. 6.2). The two-body loss coefficients measured by the atom number decay in single-component and two-component BECs are $\gamma_{22} = 8.1(3) \times 10^{-20}$ m^3/s and $\gamma_{12} = 1.51(18) \times 10^{-20}$ m^3/s. The value of γ_{22} is in reasonable agreement with experimental measurements [19, 43]; however the value of γ_{12} is in much better agreement with theoretical investigations [35] rather than the previous experimental measurements [19]. This might be caused by a different value of the magnetic field in the system. Precision measurements of a_{12} can be useful to evaluate long-term drifts in the proton to electron mass ratio, as suggested by Chin and Flambaum [45].

It is very important in precision experiments to calibrate correctly the detection system. The total number of atoms can be evaluated using the conventional absorption imaging technique [46]. However the atom number calibration in the vicinity of an atom chip can significantly differ from the calculated value for two reasons. Firstly, some part of the

probe beam can scatter from the chip surface and reach the imaging area occupied by the shadow of atoms bypassing the atoms. This artificially reduces the atomic absorption and is difficult to account for because the amount of scattered light depends on the distance of the atoms from the chip surface. Secondly, during switching off the current in coils, the magnetic field changes its direction and absolute value. This affects the absorption in an unpredictable way. One of the calibration techniques using the scaling of quantum projection noise with total number of atoms for the calibration was employed in recent spin-squeezing experiments [47, 48]. The second technique employs the scaling of the ratio of the number of condensed atoms to the total number of atoms in a Bose gas with temperature below the critical point [49, 50]. This method requires careful measurement of temperature. We have developed a new interferometric technique for the calibration of the total number of atoms (Ch. 4). We have compared this with the calibration given by condensation temperature, and the results of both methods agree with each other.

The precision of a conventional Ramsey atom interferometer is usually limited by the standard quantum limit for which the phase uncertainty is $1/\sqrt{N}$, where N is the total number of atoms. The use of squeezed rather than coherent spin states allows one to overcome this limit and, in principle, to reach the Heisenberg limit of $1/N$ for the interferometer precision. In 2010 spin-squeezed states were first obtained in multi-component BECs using a one-axis twisting scheme proposed in 1993 [51]. In order to produce squeezing, the nonlinearity was created by splitting the two components spatially [47] or by manipulating the inter-species scattering length via a magnetic Feshbach resonance [48]. The use of spin-squeezed states can drastically increase the sensitivity of atom interferometers making possible even gravitational waves detection [52]. It was recently proposed that the two-axis twisting scheme which allows one to ultimately reach the Heisenberg-limited squeezed state can be also realized in BECs [53].

Another recently emerging area in the field of multi-component ultra-cold atomic systems is RF-induced Feshbach resonances. Magnetic Fano-Feshbach resonances have been known for a long time [54, 55] and have been employed for tuning atomic interactions [48]. However it is not always possible to tune the magnetic field appropriately

as, for example, with $|F=1, m_F=-1\rangle$ and $|F=2, m_F=1\rangle$ states in ^{87}Rb. Apart from that, a Feshbach resonance can be accessed by applying optical fields [56]. Recent theoretical works have predicted RF-induced Feshbach resonances [57, 58] at near-zero magnetic fields in ^{87}Rb. That might be extremely useful for making fast collisional gates with neutral atoms for quantum information processing or for tuning interactions for creating entangled states. RF-induced Feshbach resonances were demonstrated in the vicinity of magnetic resonances [59]; however they were not observed at near-zero magnetic fields before the present work. In this thesis the detection of previously unobserved RF-induced Feshbach resonances between the ^{87}Rb states $|F=1, m_F=-1\rangle$ and $|F=2, m_F=1\rangle$ is reported (Ch. 7). The information provided might be very useful for characterization of inter-atomic interaction potentials [40].

Some of the experiments not directly related to this thesis are also important to mention. One of them opened a new field in multi-component BECs: spin-orbit coupled BECs [60]. This might allow one to simulate solid state condensed matter systems in degenerate quantum gases. The other newly emergent field is BECs with magnetic dipole interactions [61, 62]. It also worth mentioning that a new record of the lowest temperature (~ 0.4 nK) was established using adiabatic cooling with a two-component BEC in an optical lattice [63].

1.2 Thesis outline

This thesis describes three research outcomes produced using precision measurements with a two-component ^{87}Rb BEC. The introductory chapter (Ch. 1) places our work in context among other experiments with two-component BECs.

Chapter 2 describes the spatial evolution of a trapped two-component BEC prepared in a non-equilibrium state. Firstly, it contains a derivation of the coupled Gross-Pitaevskii equations from the variational principle. Secondly, we discuss a simplified "constant collisional shift" model which was widely used beforehand for understanding the phase dynamics of BECs. An effective single-component model which incorporates collective oscillations and mean-field rephasing in 1D BECs is discussed. Next, we derive an

analytical single-component model of a three-dimensional two-component BEC in cigar-shaped traps which is in much better agreement with the GPE simulations than the 1D model, correctly describing collective oscillations and rephasing in two-component BECs. This theory is widely used throughout the thesis.

Chapter 3 briefly describes the main features of the atom chip apparatus. We carefully characterise parameters of trapping potential such as trap frequencies and anharmonicities. Microwave and RF spectroscopy of a trapped BEC is used to measure parameters of the microwave and RF fields. We measure the noise of imaging laser and derive its relation to the noise for the measured total number of atoms. The optical resolution is improved and characterized. We improve the efficiency of dual-state imaging of two states with the same magnetic moment, initially implemented by Russell Anderson [22, 64], from 44% to 99%. We apply an "eigenface" fringe-removal algorithm, which was first proposed to be used for imaging of ultracold atoms by M. Erhard [65], to process the experimental images.

In chapter 4, we present our method of interferometric atom number calibration. We compare this with the existing method of calibration using the condensation temperature and find very good agreement when the latter includes the finite atom number and first order mean-field corrections.

In chapter 5, we describe our finding that two-component BECs do not irreversibly dephase but periodically rephase with the frequency of collective oscillations. We apply a spin-echo technique and obtain a significantly improved interferometric contrast which implies a coherence time of 2.8 s, the highest coherence time of an interacting BEC to our knowledge. We also characterize the phase noise in the system and discuss possible ways of observing the coherence fundamentally limited by quantum noise. The results have been published in [31].

We present measurements of the ^{87}Rb scattering lengths and the two-body loss coefficients of states $|1\rangle$ and $|2\rangle$ in chapter 6. Firstly, we measure a_{12} by fitting collective oscillations of a two-component BEC with coupled GPE simulations. Then, we measure a_{22} in Ramsey interferometry with $\pi/2$ and $\pi/10$ preparation pulses. We observe the two-body decay of a single component BEC in state $|2\rangle$ and a two-component BEC composed

of 10% state $|2\rangle$ and 90% state $|1\rangle$ and obtain the two-body loss coefficients γ_{22} and γ_{12}. We also employ the interferometric atom number calibration. We obtain results which have the best precision reported for scattering length measurements (0.016% for a_{12}).

Magnetic Feshbach resonances are not experimentally available at low magnetic fields for the system of states $|1\rangle$ and $|2\rangle$ in ^{87}Rb. Therefore, in the last chapter 7, we detect and characterize RF-induced Feshbach resonances at a magnetic field of 3.25 G with two-body losses. The resulting positions of the resonances are in a good agreement with theoretical predictions [58]. We also attempt to observe small variations of the scattering length a_{12} using the measurement technique we have developed. However this requires reduction of technical noise.

Chapter 2

Quantum dynamics of a two-component Bose-Einstein condensate

A binary Bose-Einstein condensate represents a quantum system composed of two interpenetrating BECs. It can consist of condensates of two different elements, the condensate of the same element being prepared in two different internal states, or the condensate in a double-well potential. In this thesis we focus on the evolution and interferometry of a two-component condensate magnetically trapped in two hyperfine states $|1\rangle$ and $|2\rangle$. Different hyperfine states are further labelled in terms of their quantum numbers as $|F, m_F\rangle$, where F is the hyperfine quantum number and m_F is the magnetic quantum number of a Zeeman sublevel. Using the Bloch vector formalism the two-component system can be treated as a pseudospin-1/2 system [66, 64].

When a two-component BEC is in its ground state, it is in equilibrium, i.e. no density dynamics occur for any of the components, and the phase dynamics are homogeneous. An important property of a two-component ground state is its miscibility. Miscible BECs spatially overlap in their ground states; however immiscible condensates are spatially separated. The miscibility is defined by the sign of $a_{11}\,a_{22} - a_{12}^2$ (where a_{11} and a_{22} are

the intraspecies scattering lengths, a_{12} is the interspecies scattering length). The two-component condensate is immiscible and the two condensates no longer overlap when $a_{11}\,a_{22} - a_{12}^2 < 0$ [67]. Nevertheless, the Thomas-Fermi approximation does not describe the separation of the two components in the ground state ideally when the miscibility parameter $a_{11}\,a_{22} - a_{12}^2$ is close to 0 and the kinetic energy term becomes comparable with the difference in collisional energies of both components [68, 64]. Being prepared out of equilibrium, two-component BECs exhibit collective oscillations [19] which are modified and damped by the collisional loss of atoms. Additionally, two-component BECs out of equilibrium exhibit dephasing [22] and rephasing [31] processes.

2.1 Mean-field and hydrodynamic description

In the mean-field approximation, the state of each BEC component is represented by a complex order parameter $\Psi_i(\mathbf{r})$ so that the BEC atom number density $n_i(\mathbf{r}) = |\Psi_i|^2$ and the phase of each component is defined by $\arg(\Psi_i) = \phi_i$. The mean-field energy functional of a two-component BEC in the frame rotating with the frequency of the energy splitting between the two levels is [10]

$$\begin{aligned} E = \int d\mathbf{r} \Bigg[& \frac{\hbar^2}{2m} |\nabla\Psi_1|^2 + \frac{\hbar^2}{2m} |\nabla\Psi_2|^2 + V(\mathbf{r}) |\Psi_1|^2 + V(\mathbf{r}) |\Psi_2|^2 \\ & + \frac{1}{2} U_{11} |\Psi_1|^4 + \frac{1}{2} U_{22} |\Psi_2|^4 + U_{12} |\Psi_1|^2 |\Psi_2|^2 \Bigg], \end{aligned} \tag{2.1}$$

where $U_{kn} = 4\pi\hbar^2 a_{kn}/m$ is the effective interaction potential expressed in terms of the s-wave scattering length a_{kn} for collisions involving states k and n, m is the particle mass and $V(\mathbf{r})$ is the external trapping potential. A pair of Coupled Gross-Pitaevskii equations (CGPE) can be derived from Eq. 2.1 from the variational principle $i\hbar\partial\Psi_j/\partial t = \delta E/\delta\Psi_j^*$:

$$\begin{aligned} i\hbar\frac{\partial\Psi_1}{\partial t} &= \left[-\frac{\hbar^2\nabla^2}{2m} + V(\mathbf{r}) + U_{11}|\Psi_1|^2 + U_{12}|\Psi_2|^2 \right] \Psi_1, \\ i\hbar\frac{\partial\Psi_2}{\partial t} &= \left[-\frac{\hbar^2\nabla^2}{2m} + V(\mathbf{r}) + U_{12}|\Psi_1|^2 + U_{22}|\Psi_2|^2 \right] \Psi_2. \end{aligned} \tag{2.2}$$

These equations do not contain loss terms yet. The CGPE with the inclusion of losses are

$$\begin{aligned} i\hbar\frac{\partial\Psi_1}{\partial t} &= \left[-\frac{\hbar^2\nabla^2}{2m} + V(\mathbf{r}) + U_{11}|\Psi_1|^2 + U_{12}|\Psi_2|^2 - i\Gamma_1\right]\Psi_1, \\ i\hbar\frac{\partial\Psi_2}{\partial t} &= \left[-\frac{\hbar^2\nabla^2}{2m} + V(\mathbf{r}) + U_{12}|\Psi_1|^2 + U_{22}|\Psi_2|^2 - i\Gamma_2\right]\Psi_2, \end{aligned} \tag{2.3}$$

where the loss rates of the species 1 and 2 are $\Gamma_1 = \frac{\hbar}{2}(\gamma_{111}\left|\Psi_1\right|^4 + \gamma_{12}\left|\Psi_2\right|^2)$ and $\Gamma_2 = \frac{\hbar}{2}(\gamma_{12}\left|\Psi_1\right|^2 + \gamma_{22}\left|\Psi_2\right|^2)$ [19], γ_{12} and γ_{22} are two-body loss coefficients and γ_{111} is a three-body loss coefficient. In the case of our experiment state $|1\rangle \equiv |F=1, m_F=-1\rangle$ does not experience two-body losses from inelastic collisions between atoms in state $|1\rangle$ because of angular momentum conservation, whereas the two-body loss rates in the state $|2\rangle \equiv |F=2, m_F=1\rangle$ are so high that three-body losses are negligible.

The treatment with the CGPE equations is equivalent to the hydrodynamic description [9]. The continuity equation is

$$\frac{\partial n_j}{\partial t} + \nabla\cdot(n_j\mathbf{v}_j) = 0, \tag{2.4}$$

where the BEC velocity of the j-th component is proportional to the gradient of the phase of the complex order parameter Ψ_j:

$$\mathbf{v_j} = \frac{\hbar}{m}\nabla\phi_j. \tag{2.5}$$

The equation of motion for the velocity is:

$$m\frac{\partial\mathbf{v}_j}{\partial t} = -\nabla\left(\bar{\mu}_j + \frac{1}{2}mv_j^2\right), \tag{2.6}$$

where

$$\bar{\mu}_j = V(\mathbf{r}) + n_1U_{1j} + n_2U_{j2} - \frac{\hbar^2}{2m\sqrt{n_j}}, \tag{2.7}$$

and j labels the number of the BEC component. The final term (quantum pressure) in this equation is often neglected for large numbers of atoms; however in this approximation the hydrodynamic treatment is not fully equivalent to the CGPE.

2.2 Interferometry of a two-component BEC

A two-component pseudospin-1/2 system [51, 66, 64] can be represented by a vector on a Bloch sphere (Fig. 2.1b). The phase dynamics of a two-component BEC prepared in two

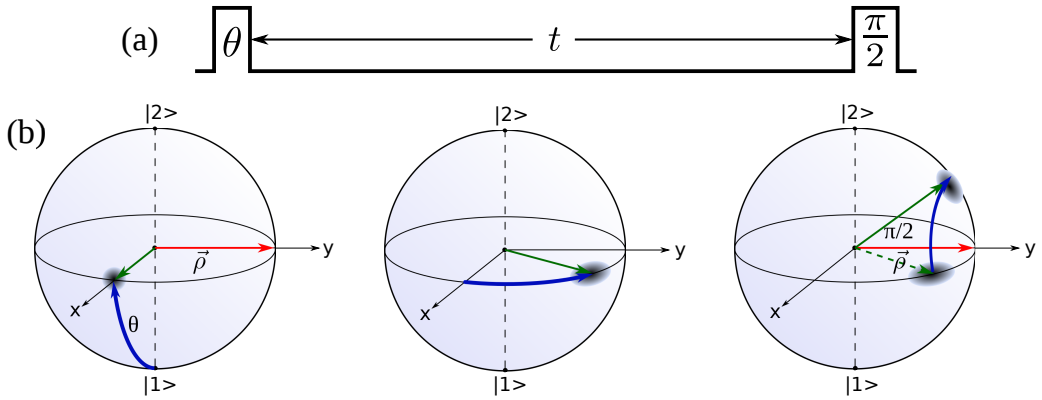

Figure 2.1: The phase dynamics of the two-component BEC is studied by a Ramsey interferometric sequence (a). A coherent superposition is prepared by an initial θ-pulse. A relative phase is accumulated during an evolution time t. Finally, the phase information is interrogated by a $\pi/2$-pulse. The corresponding pseudospin-1/2 dynamics is represented on a Bloch sphere (b).

internal states can be interrogated by Ramsey interferometry (Fig. 2.1a). A superposition of atoms is prepared by a radiation pulse with area θ which rotates the Bloch vector by the angle θ around the vector $\vec{\rho}$ in the equatorial plane of the Bloch sphere which direction coincides with the axis y if the phase of the second pulse is the same as the phase of the first pulse (Fig. 2.1b). After an evolution time t, the rotation of the Bloch vector around the vertical axis is measured by the interrogating $\pi/2$-pulse.

In Ramsey interferometry the standard measurable is the relative atom number difference obtained after the second, $\pi/2$ radiation pulse. Its value can be derived from the wavefunctions obtained in the CGPE (Eqs. 2.2). In the frame rotating with the atomic transition frequency, the operator of $\pi/2$-pulse is [64]

$$\hat{U}_{\pi/2} = \frac{1}{\sqrt{2}} \begin{bmatrix} 1 & -ie^{-i\delta\varphi} \\ -ie^{i\delta\varphi} & 1 \end{bmatrix}, \tag{2.8}$$

where $\delta\varphi$ is the phase of the second $\pi/2$-pulse relative to the first θ-pulse. The measurable is $P_z = (N_2' - N_1')/(N_2' + N_1')$, where N_1' and N_2' are the numbers of atoms in states $|1\rangle$ and $|2\rangle$ after the $\pi/2$-pulse. It can be expressed in terms of the known wavefunctions Ψ_1

and Ψ_2 before the last $\pi/2$-pulse:

$$\begin{pmatrix} \Psi_1' \\ \Psi_2' \end{pmatrix} = \hat{U}_{\pi/2} \begin{pmatrix} \Psi_1 \\ \Psi_2 \end{pmatrix}, \qquad N_1' = \int \Psi_1'^* \Psi_1' \, d^3\mathbf{r}, \qquad N_2' = \int \Psi_2'^* \Psi_2' \, d^3\mathbf{r}. \tag{2.9}$$

Substitution of N_1' and N_2' from Eq. 2.9 into the definition of P_z leads to $P_z = \mathrm{Im}(\mathcal{P})$ where

$$\mathcal{P} = \frac{\int 2e^{i\delta\varphi} \Psi_2^* \Psi_1 \, d^3\mathbf{r}}{\int \left(\Psi_2^* \Psi_2 + \Psi_1^* \Psi_1\right) d^3\mathbf{r}}. \tag{2.10}$$

When the phase $\delta\varphi$ is varied, P_z forms a sinusoidal fringe with the amplitude of $\mathcal{V} = |\mathcal{P}|$. As follows from Eq. 2.10, P_z is proportional to the sine of the phase difference between the wavefunctions Ψ_1 and Ψ_2, the amplitude of this sinusoidal dependence is determined by the spatial overlap of the wavefunctions.

At short evolution times the kinetic energy terms in Eq. 2.2 can be neglected as there is no superfluid flow initially and the dynamics of the order parameter will be governed by the collisional shift *between* the two components ($\Delta\nu_{12}$). For non-condensed clouds and BECs composed of two components with densities n_1 and n_2 the collisional shift is [21]

$$\Delta\nu_{12}(\mathbf{r}) = \frac{\alpha\hbar}{m} n(\mathbf{r}) \left[a_{22} - a_{11} + s\left(2a_{12} - a_{11} - a_{22}\right)\right], \tag{2.11}$$

where $n = n_1 + n_2$ is the density of the cloud, $s = (n_1 - n_2)/n$, and the exchange symmetry parameter $\alpha = 2$ for non-condensed atoms and $\alpha = 1$ for a coherently prepared two-component BEC.

We consider the process of Ramsey interferometry and derive the evolution of Ramsey fringes in a coherent superposition prepared by a coupling pulse with splitting angle θ in a trap with cigar-shaped geometry where the z axis is the weak confinement direction, r is a radial coordinate perpendicular to the z axis. A simple semi-quantitative model can be developed based on neglecting the kinetic energy contribution and assuming that the total atom number densities in each component n_1 and n_2 retain the same initial parabolic Thomas-Fermi (TF) profile. In the TF approximation the three-dimensional density of the single-component condensate is:

$$n(r, z) = n_0 \left(1 - \frac{r^2}{R_\mathrm{r}^2} - \frac{z^2}{R_\mathrm{ax}^2}\right), \tag{2.12}$$

where n_0 is the peak density of the condensate, $R_{\rm ax}$ is the TF radius in the direction of the lowest trap frequency, and $R_{\rm r}$ is the TF radius in the tight (radial) direction of the cigar-shaped cloud. The phase evolution of a two-component BEC in a cigar-shaped trap in which the radial trap frequency ω_r is much higher than the axial trap frequency ω_z occurs predominantly in one dimension as long as the radial dynamics is energetically unfavourable [69, 70, 22]. If we assume that the density profiles of two components do not change with time and the condensate maintains TF profile, the collisional shift between the two components therefore does not depend on r and can be expressed as

$$\Delta\nu_{12}(z) = \frac{\hbar}{m} n(z) \left[a_{22} - a_{11} + s\left(2a_{12} - a_{11} - a_{22}\right)\right], \tag{2.13}$$

where $n(z)$ is the radially averaged total density of BEC. The radially averaged density is

$$n(z) = \frac{\int\limits_0^{R_{\rm r}\sqrt{1-z^2/R_{\rm ax}^2}} 2\pi r\, n(r,z)^2\, dr}{\int\limits_0^{R_{\rm r}\sqrt{1-z^2/R_{\rm ax}^2}} 2\pi r\, n(r,z)\, dr} = \frac{2}{3} n_0 \left(1 - \frac{z^2}{R_{\rm ax}^2}\right). \tag{2.14}$$

For a two-component BEC prepared by a $\pi/2$-pulse, $s = 0$. The approximation of an unmodified density TF profile for each component holds well for short evolution times when the components separation can be neglected and the effective 1D wavefunctions of the BEC components are

$$\begin{aligned} \psi_1(z,t) =& \sqrt{\frac{1+s}{2} n_{1D}(z)}\, e^{i\varphi_1(z,t)}, \\ \psi_2(z,t) =& \sqrt{\frac{1-s}{2} n_{1D}(z)}\, e^{i\varphi_2(z,t)}, \end{aligned} \tag{2.15}$$

where the difference of phases is

$$\varphi_2(z,t) - \varphi_1(z,t) = 2\pi\Delta\nu_{12}(z)t + \Delta\cdot t + \pi/2, \tag{2.16}$$

where Δ is the detuning of the coupling radiation from the atomic transition frequency and $n_{\rm 1D}$ is the one-dimensional BEC density:

$$n_{\rm 1D}(z) = \int\limits_0^{R_{\rm r}\sqrt{1-z^2/R_{\rm ax}^2}} 2\pi r\, n(r,z)\, dr = \frac{\pi R_{\rm r}^2 n_0}{2} \left(1 - \frac{z^2}{R_{\rm ax}^2}\right)^2. \tag{2.17}$$

The measurable quantity in Ramsey interferometry is the relative atom number difference $P_z = (N_2' - N_1')/(N_1' + N_2')$ after the interrogating $\pi/2$ pulse. After the application of the $\pi/2$ pulse a measurable $P_z = \mathrm{Im}(\mathcal{P}(t)) \propto \sin(\varphi_1 - \varphi_2)$ is retrieved, where t is the time between two pulses in Ramsey interferometry and

$$\mathcal{P}(t) = \frac{2}{N} \int_{-R_{\mathrm{ax}}}^{R_{\mathrm{ax}}} \psi_2^*(z,t)\psi_1(z,t)\, dz. \tag{2.18}$$

Substituting Eqs. 2.15 into this equation and changing the variable $z/R_{\mathrm{ax}} = \sin\beta$ we obtain

$$\begin{aligned} \mathcal{P}(t) &= \frac{15}{16} i\sqrt{1-s^2} \int_{-\frac{\pi}{2}}^{\frac{\pi}{2}} (\cos\beta)^5 \; e^{i\kappa\,(\cos\beta)^2} d\beta, \\ \text{where } \kappa &= 2\pi\frac{\hbar}{m} \times \frac{2}{3} n_0 \times \left[a_{22} - a_{11} + s\,(2a_{12} - a_{11} - a_{22})\right] t. \end{aligned} \tag{2.19}$$

After the integration is performed

$$\begin{aligned} \mathcal{P}(\kappa) =& i\frac{\sqrt{1-s^2}}{64\,\kappa^2\,\sqrt{i\,\kappa}} \Big\{ e^{i\,\kappa}\,\sqrt{\pi}\,\mathrm{erf}\left(\sqrt{i\,\kappa}\right)\,\left(60\,\kappa^2 + 60 i\,\kappa - 45\right) \\ & - 60\,i\,\kappa\,\sqrt{i\,\kappa} + 90\,\sqrt{i\,\kappa}\Big\}, \end{aligned} \tag{2.20}$$

where $\mathrm{erf}(\xi)$ is the complex error function (Faddeeva function). In the limit $\kappa \gg 1$, the function oscillates with a period of $\kappa_T = 2\pi$ (Fig. 2.2):

$$\lim_{\kappa\to+\infty} \left(\frac{P_z(t)}{|\mathcal{P}(t)|} - \cos\left(\kappa - \pi/4\right) \right) = 0. \tag{2.21}$$

Thus, the radial frequency of a Ramsey fringe in the time domain can be written as:

$$\omega_{\mathrm{Ramsey}} = 2\pi\frac{\kappa}{t\,\kappa_T} = 2\pi \times \frac{2}{3}\frac{\hbar}{m} n_0 \left[a_{22} - a_{11} + s\,(2a_{12} - a_{11} - a_{22})\right], \tag{2.22}$$

or

$$\begin{aligned} \omega_{\mathrm{ramsey}} &= \alpha N^{2/5}, \quad \text{where} \\ \alpha &= \frac{1}{3}\left(\frac{2\times 15^2 \times \pi^6 (f_{\mathrm{r}} f_{\mathrm{ax}}^2)^2 m}{\hbar a_{11}^3}\right)^{1/5} \left[a_{22} - a_{11} + s\,(2a_{12} - a_{11} - a_{22})\right]. \end{aligned} \tag{2.23}$$

For short evolution times the approximation of unmodified total density profile holds reasonably well and the analytical estimate (Eq. 2.23) yields a value of the fringe frequency

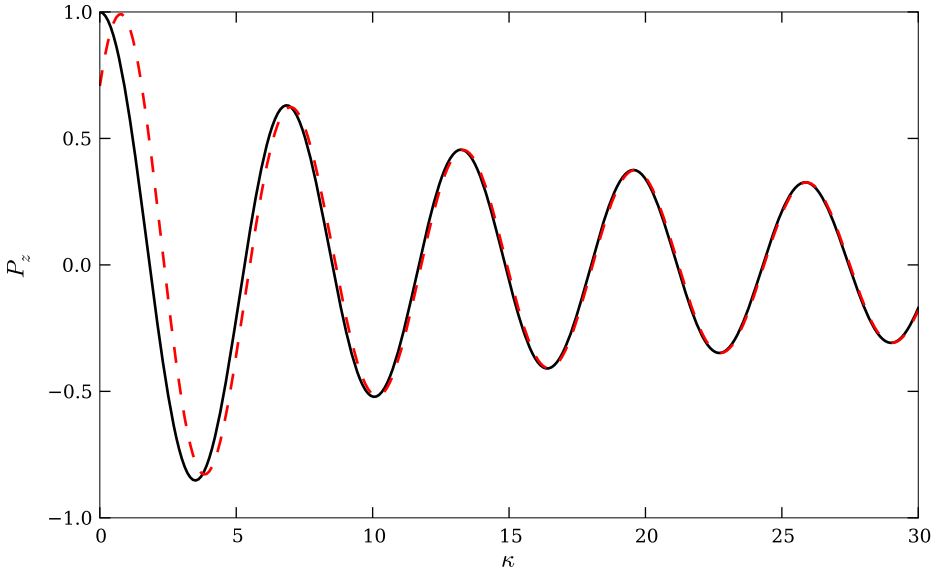

Figure 2.2: The fringe measurable $P_z(\kappa)$ obtained analytically (black solid line) (Eq. 2.20) has a period of 2π. In the limit $\kappa \to \infty$ the fringe $P_z(t)$ is close to the function $A(t)\cos(\kappa - \pi/4)$ (red dashed line), where the fringe amplitude is $A(t) = |\mathcal{P}(t)|$.

ω_{Ramsey} close to the one obtained from the full GPE simulations. For example, for our trap frequencies ($\omega_z = 2\pi \times 11.69$ Hz, $\omega_r = 2\pi \times 97.0$ Hz) and $N = 44 \times 10^4$, the value $\alpha = 0.72$ s^{-1} given by the formula is in good agreement with $\alpha = 0.79$ s^{-1} obtained from the simulations of Eq. 2.2 at $t = 20$ ms, even though the condition $\kappa \to \infty$ is not satisfied ($\kappa = 1.1$). The Ramsey fringe in this case can be approximated (for zero detuning Δ) by:

$$P_z(t) = \cos\left(\alpha N^{2/5} t - \frac{\pi}{4}\right). \tag{2.24}$$

2.3 Effective single-component description for a 1D two-component BEC

We derive an analytical description for the 1D two-component BEC dynamics which is valid for long evolution times repeating the treatment given by Z. Dutton and C. Clark [71]. It is derived in the approximation that the fluctuations (high-frequency oscillations) of the total density are smaller and faster than the evolution of each individual component. The

idea is based on the approximation that the effective "external" potential for one of the components is represented as the sum of a parabolic trapping potential $V(\mathbf{r})$ and the collisional interaction potential with the other component $U_{ij}\, n_j(\mathbf{r}) = 4\pi n_j(\mathbf{r})\hbar^2 a_{ij}/m$ which also has a parabolic shape and is very close to the trapping potential but has opposite sign. The resultant sum of the two terms $V + U$ for a two-component BEC also yields a parabolic potential, but much weaker than the initial potential, and the "effective trap frequency" corresponding to this potential defines the dynamics of the two-component BEC. In this section we derive expressions for this model for a one-dimensional BEC which can be realised at low total atom number N [72] and in the next section we derive expressions for a similar theory for large atom numbers.

2.3.1 One-dimensional coupled Gross-Pitaevskii equations

We consider a one-dimensional BEC which can be experimentally realized in a cigar-shaped trap with trap frequencies $\omega_{\rm ax} \ll \omega_r$ and a Thomas-Fermi (TF) radius R_r in the tight direction which is much less than the healing length $\xi = (4\pi n a_{ij})^{1/2}$ and a TF radius in the weak $R_{\rm ax}$ direction which is much more than ξ [72]. In this case the dynamics of the two-component BEC is described by 1D coupled Gross-Pitaevskii equations [71]:

$$\begin{aligned} i\hbar\frac{\partial\psi_1}{\partial t} &= \left[-\frac{\hbar^2}{2m}\frac{\partial^2}{\partial z^2} + V(z) + g_{11}|\psi_1|^2 + g_{12}|\psi_2|^2\right]\psi_1, \\ i\hbar\frac{\partial\psi_2}{\partial t} &= \left[-\frac{\hbar^2}{2m}\frac{\partial^2}{\partial z^2} + V(z) + g_{12}|\psi_1|^2 + g_{22}|\psi_2|^2\right]\psi_2, \end{aligned} \tag{2.25}$$

where $V(z) = \frac{1}{2}m\omega_z^2 z^2$ is the external harmonic trapping potential in the weak direction of the trap and the wavefunctions are normalized $\int(|\psi_1|^2 + |\psi_2|^2)\, dz = 1$. The effective interaction parameter $g_{ij} = U_{ij}N/A$ includes the total number of condensed atoms N and the effective transverse area $A = 2\pi\xi_{\rm ho}^2$, where $\xi_{\rm ho} = (\hbar/m\omega_{\rm r}^2)^{1/2}$ is the radial waist of the wavefunction [73]. The relative scattering length differences $\delta_c = (a_{12} - a_{11})/a_{11}$ and $\delta_2 = (a_{22} - a_{11})/a_{11}$ are the key parameters in the evolution process. For the case of the $|1,-1\rangle$ and $|2,+1\rangle$ states of ^{87}Rb, $a_{11} = 100.40\, a_0$ [39, 41], $a_{22} = 95.44\, a_0$, $a_{12} = 98.006\, a_0$ (Ch. 6), $\delta_c < 0$, $\delta_2 < 0$ and $\delta_2 - 2\delta_c \ll |\delta_2|$. We should note that Eqs. 2.25 are not valid in the case of a 3D BEC in a harmonic trap when $R_{\rm r} > \xi$. This case will be discussed in

Sec. 2.4.

Despite the fact that the total density n of the two-component BEC remains almost unchanged [17], small density fluctuations $\delta n = n - n_0 \ll n_0$, where n_0 is the initial total density of the BEC, still should be taken into account. From Eq. 2.25 we obtain:

$$i\hbar\frac{\partial\psi_2}{\partial t} = \left[-\frac{\hbar^2}{2m}\nabla^2 - \delta_c V(z) + g_{11}\left(\delta_2 - \delta_c\right)|\psi_2|^2 + g_{11}\delta n\right]\psi_2. \tag{2.26}$$

The effective trapping potential $-\delta_c V(z)$ defines the effective confinement and the period of the dynamics described by this equation as will be seen further.

2.3.2 Fluctuations of the total density

In order to derive density fluctuations, we start from hydrodynamic equations which are equivalent to the CGPE (Eqs. 2.4 – 2.7). In the one-dimensional case we define the operator $\nabla = \partial/\partial z = '$. Defining $f = n_2/n$, $v_c = (v_1 n_1 + v_2 n_2)/n$ [71], equations of "common" motion can be obtained. Summing up algebraically the continuity equations for both components we obtain:

$$\dot{n} = -(n v_c)'. \tag{2.27}$$

From the equations of motion

$$n\dot{v}_c = n(1-f)\dot{v}_1 + nf\dot{v}_2 + \left(\frac{\dot{n}_1}{n} - \frac{n_1\dot{n}}{n^2}\right)v_1 + \left(\frac{\dot{n}_2}{n} - \frac{n_2\dot{n}}{n^2}\right)v_2. \tag{2.28}$$

Here $\dot{v}_i$ is substituted from the corresponding equations of motion (Eq. 2.6) and $\dot{n}_1 = -((1-f)nv_1)'$, $\dot{n}_2 = -(fnv_2)'$. The last two kinetic energy terms in Eq. 2.28 are neglected for simplicity:

$$\begin{aligned} mn\dot{v}_c = &- n(1-f)\left(V + n_1 g_{11} + n_2 g_{12}\right)' - \\ &nf\left(V + n_2 g_{22} + n_1 g_{12}\right)', \end{aligned} \tag{2.29}$$

where the g_{ij} are interaction parameters, the kinetic energy and quantum pressure terms are neglected. We then obtain after labelling the effective trapping potential $V' = -\delta_c V$:

$$\begin{aligned} \dot{v}_c &= -\frac{1}{m}\left[V' + (1-f)\left(n_1 g_{11}\right)' + (1-f)\left(n_2 g_{12}\right)' + f\left(n_1 g_{12}\right)' + f\left(n_2 g_{22}\right)'\right] \\ &= -\frac{1}{m}\left[V' + \left((1-f)\,n\right)'\left((1-f)\,g_{11} + f g_{12}\right) + (fn)'\left((1-f)\,g_{12} + f g_{22}\right)\right]. \end{aligned} \tag{2.30}$$

Introducing relative scattering length differences δ_c and δ_2, and making the mean field replacements

$$\begin{aligned}
\epsilon'_{MF1} &= ((1-f)\,n)'\,((1-f)\,g_{11} + f g_{12}) \\
&= ((1-f)\,n)'\,g_{11}\,(1-f+\delta_c f + f) = ((1-f)\,n)'\,g_{11}\,(1+\delta_c f)\,, \\
\epsilon'_{MF2} &= (fn)'\,((1-f)\,g_{12} + f g_{22}) \\
&= (fn)'\,g_{11}\,(1+\delta_c - f - f\delta_c + f + f\delta_2) \\
&= (fn)'\,g_{11}\,(1+\delta_c - f\delta_c + f\delta_2)\,,
\end{aligned} \tag{2.31}$$

and using

$$\begin{aligned}
n =& n_0 + \delta n, \\
m\ddot{\delta n} =& -\dot{\delta n} v'_c - \dot{\delta n}' v_c - (n_0+\delta n)\dot{v}'_c - (n_0+\delta n)'\dot{v}_c,
\end{aligned} \tag{2.32}$$

we obtain assuming $\delta n \ll n_0$

$$\begin{aligned}
m\ddot{\delta n} =& -n_0\left[V' + g_{11}\left(n'_0 + \delta n'\right) + \epsilon'_{MF1} + \epsilon'_{MF2} + \ldots\right]' - \\
& n'_0\left[V' + g_{11}\left(n'_0 + \delta n'\right) + \epsilon'_{MF1} + \epsilon'_{MF2} + \ldots\right].
\end{aligned} \tag{2.33}$$

The second term can be neglected at very large N since n' has very small effect on the total energy in that case, n_0 will have a TF profile. Also n_0 obtained in the TF approximation implies $(V' + g_{11} n'_0) = \mu'_1 = 0$. Thus, the second time-derivative of δn is

$$\begin{aligned}
\ddot{\delta n} &= -\frac{n_0}{m}\left[V + \epsilon'_{MF1} + \epsilon'_{MF2} + \ldots\right]' \\
&= -\frac{n_0}{m}\left[V + g_{11} n_0\left(\delta_2 f f' + \delta_c f'\,(1-2f)\right) + g_{11}\delta n' + g_{11} n'_0\right]'.
\end{aligned} \tag{2.34}$$

When the mean-field contribution ϵ'_{MF1} dominates the kinetic energy, we set $\ddot{\delta n} = 0$ for the steady-state solution and obtain

$$\delta n = -n_0\left(\frac{f^2}{2}\,(\delta_2 - 2\delta_c) + f\delta_c\right). \tag{2.35}$$

For the special case of the states $|1\rangle \equiv |1,-1\rangle$ and $|2\rangle \equiv |2,+1\rangle$ in ^{87}Rb ($a_{11} = 100.40\,a_0$, $a_{22} = 95.44\,a_0$ and $a_{12} = 98.006\,a_0$) the relative scattering length differences follow the relation: $|\delta_2 - 2\delta_c| \ll |\delta_c|$. Taking this into account and substituting Eq. 2.35 into

Eq. 2.26, the single-component Schrödinger equation for the state $|2\rangle$in a one-dimensional BEC is obtained:

$$i\hbar\frac{\partial\psi_2}{\partial t} = \left[-\frac{\hbar^2}{2m}\frac{\partial^2}{\partial z^2} - \delta_c V(z)\right]\psi_2. \tag{2.36}$$

We clearly see that this equation is identical to the harmonic oscillator equation with the scaled frequency $\omega_{\text{eff}} = \sqrt{1 - a_{12}/a_{11}}\omega_z$. According to this equation, the component $|2\rangle$ periodically focuses if $\delta_c < 0$ and $\delta_2 - 2\delta_c \gtrsim 0$. In the derivation of this equation we neglected the kinetic energy and quantum pressure terms. This condition requires the component considered (component 2 in this case) to spend most of the time far from the BEC boundaries. This works well for state $|2\rangle$ since it focuses; however this condition is not satisfied for the component $|1\rangle$ because the larger value of the scattering length a_{11} forces the component $|1\rangle$ to go to the BEC boundaries. It was also numerically shown [71] that neglecting quantum pressure and kinetic energy is not valid when n_2 is comparable with n_0. Practically, if Eq. 2.36 gives $n_2 > n_0$ it is a good signature that the quantum pressure terms should not be neglected.

2.4 Effective single-component description for a 3D BEC

Even though Eq. 2.36 is in an excellent agreement with the one dimensional GPE simulations, it disagrees with the three-dimensional GPE simulations if the BEC is not 1D, i.e., R_r is more than the healing length. Our goal is to derive an effective single-component description [71] for a two-component BEC in a cigar-shaped geometry for the high atom number limit. It is known that for this geometry the reduced 1D Schrödinger equation does not coincide with the 1D Gross-Pitaevskii equation [70]. We also consider the transfer of a small fraction of atoms from state $|1\rangle$ to state $|2\rangle$ ($n_2 \ll n_1$). We first derive a system of one-dimensional non-polynomial equations for the two component system, in analogy with the single component [70] and then proceed with the effective single-component (harmonic oscillator) theory.

2.4.1 Effective 1D coupled Euler-Lagrange equations

We consider the case of a tight transverse confinement ($\omega_r \gg \omega_z$) where the 3D dynamics of a two-component BEC can be conveniently described by the effective 1D treatment. We use the variational method and follow the procedure developed for single-component condensates [70, 74, 75]. The action functional of a two-component BEC can be written in a similar way to [76]:

$$S = \int \left(\mathcal{L}_1 + \mathcal{L}_2 - U_{12} \left|\Psi_1\right|^2 \left|\Psi_2\right|^2 \right) d^3\mathbf{r}\, dt, \tag{2.37}$$

where the Lagrangian density of the component $|j\rangle$ is

$$\begin{aligned} \mathcal{L}_j = & i\frac{\hbar}{2}\left(\Psi_j^* \frac{\partial}{\partial t}\Psi_j - \Psi_j \frac{\partial}{\partial t}\Psi_j^*\right) \\ & - \frac{\hbar^2}{2m}\left|\nabla\Psi_j\right|^2 - V\left|\Psi_j\right|^2 - \frac{1}{2}U_{jj}\left|\Psi_j\right|^4. \end{aligned} \tag{2.38}$$

The three-dimensional GPE (Eq. 2.2) can be obtained using $\partial S/\partial\Psi_j^* = 0$ [10]. In order to reduce the 3D treatment to the 1D case, we factorize the wavefunctions in the form [70]

$$\Psi_j(\mathbf{r}, t) = \phi_j\left(r; \sigma_j\left(z,t\right)\right) f_j\left(z,t\right), \tag{2.39}$$

where f_j is normalized to the atom number in component j and ϕ_j is a trial Gaussian function normalized to 1:

$$\phi_j\left(r, \sigma_j\left(z,t\right)\right) = \frac{1}{\sqrt{\pi}\sigma_j\left(z,t\right)} e^{-\frac{r^2}{2\sigma_j(z,t)^2}}. \tag{2.40}$$

The use of the trial Gaussian functions for the radial dependence of the condensate is justified [77, 70] because we are interested in small changes of interaction potentials and a Gaussian function represents the wave function of the linear Schrödinger equation with a harmonic potential. In the experiments we describe, we start with all atoms condensed in state $|1\rangle$. Then, we transfer a small fraction of the atoms to state $|2\rangle$ by a radiation pulse with the area $\theta \ll \pi$ (Fig. 2.1a). This changes the interactions for both components. However this modification is small and the density of component $|1\rangle$ stays almost constant, in agreement with GPE simulations. A typical Thomas-Fermi (TF) radius of a BEC in our experiments along the tight trap direction is 4 μm, four times larger than the size of the

corresponding harmonic oscillator ground state. However a trial Gaussian wavefunction is known to give consistent results for 1D reduction even in the case of a TF radial profile of a BEC [70]. We assume that ϕ_j is slowly varying along the axial coordinate relative to the radial direction and obtain

$$\nabla^2\phi_j \approx \left(\frac{\partial^2}{\partial x^2}+\frac{\partial^2}{\partial y^2}\right)\phi_j. \tag{2.41}$$

Using the Euler-Lagrange equations

$$\frac{\partial S}{\partial f_j^*}=0, \qquad \frac{\partial S}{\partial \sigma_j}=0, \tag{2.42}$$

we obtain

$$\begin{aligned} i\hbar\frac{\partial}{\partial t}f_1 = \Bigg[&-\frac{\hbar^2}{2m}\frac{\partial^2}{\partial z^2}+\frac{m\omega_z^2 z^2}{2}+\left(\frac{\hbar^2}{2m\sigma_1^2}+\frac{m\omega_r^2\sigma_1^2}{2}\right)\\ &+\frac{U_{11}}{2\pi\sigma_1^2}\left|f_1\right|^2+\frac{U_{12}}{\pi\left(\sigma_1^2+\sigma_2^2\right)}\left|f_2\right|^2\Bigg]f_1, \end{aligned} \tag{2.43}$$

$$\begin{aligned} i\hbar\frac{\partial}{\partial t}f_2 = \Bigg[&-\frac{\hbar^2}{2m}\frac{\partial^2}{\partial z^2}+\frac{m\omega_z^2 z^2}{2}+\left(\frac{\hbar^2}{2m\sigma_2^2}+\frac{m\omega_r^2\sigma_2^2}{2}\right)\\ &+\frac{U_{22}}{2\pi\sigma_2^2}\left|f_2\right|^2+\frac{U_{12}}{\pi\left(\sigma_1^2+\sigma_2^2\right)}\left|f_1\right|^2\Bigg]f_2, \end{aligned} \tag{2.44}$$

$$-\frac{\hbar^2}{2m}\sigma_1^{-3}+\frac{m\omega_r^2\sigma_1}{2}-\frac{1}{2}\frac{U_{11}}{2\pi\sigma_1^3}\left|f_1\right|^2-\frac{U_{12}\sigma_1}{\pi\left(\sigma_1^2+\sigma_2^2\right)^2}\left|f_2\right|^2=0, \tag{2.45}$$

$$-\frac{\hbar^2}{2m}\sigma_2^{-3}+\frac{m\omega_r^2\sigma_2}{2}-\frac{1}{2}\frac{U_{22}}{2\pi\sigma_2^3}\left|f_2\right|^2-\frac{U_{12}\sigma_2}{\pi\left(\sigma_1^2+\sigma_2^2\right)^2}\left|f_1\right|^2=0. \tag{2.46}$$

Eqs. 2.43-2.46 are the effective one-dimensional coupled Euler-Lagrange equations describing the dynamics of a cigar-shaped two-component BEC. Equations 2.45 and 2.46 do not contain an imaginary part as long as ϕ_j is real and the radial dynamics are neglected. The inclusion of the radial dynamics for the single-component case is described in [75].

In the limit $|f_2| \ll |f_1|$

$$\sigma_1^4 = \left(\frac{\hbar}{m\omega_r}\right)^2\left(1+2a_{11}\left|f_1\right|^2\right), \tag{2.47}$$

$$\sigma_2^4 = \left(\frac{\hbar}{m\omega_r}\right)^2\left(1+\frac{8a_{12}}{\left(1+\frac{\sigma_1^2}{\sigma_2^2}\right)^2}\left|f_1\right|^2\right). \tag{2.48}$$

In the limit of low densities $2a_{11}\left|f_1\right|^2 \ll 1$ the condensate has a radial Gaussian profile and becomes quasi-1D. We focus on the opposite limit $2a_{11}\left|f_1\right|^2 \gg 1$ where the equations for the widths of the two components are

$$\sigma_1^4 = \left(\frac{\hbar}{m\omega_r}\right)^2 2a_{11}\left|f_1\right|^2, \tag{2.49}$$

$$\sigma_2^4 = \left(\frac{\hbar}{m\omega_r}\right)^2 \frac{8a_{12}}{\left(1+\frac{\sigma_1^2}{\sigma_2^2}\right)^2}\left|f_1\right|^2. \tag{2.50}$$

From Eqs. 2.49 and 2.50 we obtain σ_2 in terms of σ_1:

$$\frac{\sigma_2^4}{\sigma_1^4}\left(1+\frac{\sigma_1^2}{\sigma_2^2}\right)^2 = \frac{4a_{12}}{a_{11}}, \tag{2.51}$$

$$\sigma_2^2 = \sigma_1^2\left(2\sqrt{\frac{a_{12}}{a_{11}}}-1\right). \tag{2.52}$$

2.4.2 Effective single-component equation

The Schrödinger equation for component 2 in the limit $\left|f_2\right|^2 \ll \left|f_1\right|^2$ is

$$i\hbar\frac{\partial}{\partial t}f_2 = \left[-\frac{\hbar^2}{2m}\frac{\partial^2}{\partial z^2} + V + \left(\frac{\hbar^2}{2m\sigma_2^2}+\frac{m\omega_r^2\sigma_2^2}{2}\right) + \frac{U_{12}}{\pi\left(\sigma_1^2+\sigma_2^2\right)}\left|f_1\right|^2\right] f_2. \tag{2.53}$$

In the limit of high density

$$\sigma_{1,2} \gg \sqrt{\frac{\hbar}{m\omega_r}}, \quad \text{and} \tag{2.54}$$

$$\frac{\hbar^2}{2m\sigma_{1,2}^2} \ll \frac{m\omega_r^2\sigma_2^2}{2}. \tag{2.55}$$

the radial kinetic energy term can be neglected. The density of component 1 can be obtained in the TF limit when $n_2 \ll n_1$ (in accordance with [70]):

$$\left|f_1\right|^2 = \frac{2}{9\hbar^2\omega_r^2 a_{11}}\left(\mu - V\right)^2, \tag{2.56}$$

$$\mu = \left(\frac{135Na_{11}\hbar^2\omega_r^2\omega_z\sqrt{m}}{2^{\frac{11}{2}}}\right)^{\frac{2}{5}} \tag{2.57}$$

where μ is the effective chemical potential of a two-component BEC obtained by the normalization of $\left|f_1\right|^2$ to the number of atoms in state 1. Equation 2.56 is valid for

$|z| < r_{\rm TF} = (2\mu/m\omega_z^2)^{1/2}$, otherwise $|f_1| = 0$. We use Eq. 2.56 for $|f_1|$ in Eq. 2.53; however this implies a certain limitation on $r_{\rm TF}$ for which the analytical solution is valid; this is discussed after the solution is obtained (Eq. 2.67). The substitution of $|f_1|$, σ_1 and σ_2 into Eq. 2.53 yields (step-by-step):

$$\frac{U_{12}}{\pi\left(\sigma_1^2+\sigma_2^2\right)}\left|f_1\right|^2 = \frac{4\pi\hbar^2}{m}\frac{1}{2\pi\sqrt{a_{12}/a_{11}}}\frac{\left|f_1\right|^2}{\frac{\hbar}{m\omega_r}\sqrt{2a_{11}}\left|f_1\right|} = \hbar\omega_r\sqrt{2a_{12}}\left|f_1\right|, \tag{2.58}$$

$$\frac{m\omega_r^2\sigma_2^2}{2} = \frac{m\omega_r^2}{2}\left(2\sqrt{\frac{a_{12}}{a_{11}}}-1\right)\frac{\hbar}{m\omega_r}\sqrt{2a_{11}}\left|f_1\right|. \tag{2.59}$$

Substituting the value of $|f_1|$ from the Thomas-Fermi approximation, we obtain

$$\frac{U_{12}}{\pi\left(\sigma_1^2+\sigma_2^2\right)}\left|f_1\right|^2 + \frac{m\omega_r^2\sigma_2^2}{2} = \frac{\mu-V}{3}\left(4\sqrt{\frac{a_{12}}{a_{11}}}-1\right). \tag{2.60}$$

This is valid only when the TF radius of the BEC in the z direction is large enough and will be discussed after the solution is obtained. Finally we obtain the Schrödinger equation for component 2

$$i\hbar\frac{\partial}{\partial t}f_2 = \left[-\frac{\hbar^2}{2m}\frac{\partial^2}{\partial z^2} + \frac{m\omega_{\rm eff}^2 z^2}{2} + \mu_{\rm eff}\right]f_2, \tag{2.61}$$

where

$$\omega_{\rm eff} = \frac{2}{\sqrt{3}}\sqrt{1-\sqrt{\frac{a_{12}}{a_{11}}}}\,\omega_z, \tag{2.62}$$

$$\mu_{\rm eff} = \frac{\mu}{3}\left(4\sqrt{\frac{a_{12}}{a_{11}}}-1\right). \tag{2.63}$$

2.4.3 Frequency of collective oscillations

Apart from the constant term $\mu_{\rm eff}$, this is a Schrödinger equation for a harmonic oscillator. If the superposition of states $|1\rangle$ and $|2\rangle$ is prepared by a pulse with area θ, the 1D wavefunction of state $|2\rangle$ is expressed in terms of a TF profile for state $|1\rangle$ as $f_2(z,0) = \sin^2(\theta/2)\, f_1(z,0)$. Therefore, the solution of Eq. 2.63 takes the form

$$f_2(z,t) = e^{-i\mu_{\rm eff}t/\hbar}\sum_{k=0}^{\infty}\left[e^{-i\omega_{\rm eff}\left(2k+\frac{1}{2}\right)t}\int\psi_{\rm ho}(2k,z)\, f_2(z,0)\, dz\right], \tag{2.64}$$

where only even harmonic oscillator eigenstates $\psi_{\rm ho}(2k,z)$ contribute to the solution, because the wavefunction $f_2(z,0)$ is symmetric about $z=0$. Equation 2.64 is periodic in

such a way that

$$f_2(z, t + n/f_c) = e^{-i\mu_{\text{eff}} n/\hbar f_c} f_2(z, t), \quad n \in \mathbb{Z}, \tag{2.65}$$

where $f_c = 2 \times \omega_{\text{eff}}/2\pi$ gives the frequency of the collective oscillations:

$$f_{\text{c}} = \frac{4 f_z}{\sqrt{3}} \sqrt{1 - \sqrt{\frac{a_{12}}{a_{11}}}}. \tag{2.66}$$

For our conditions ($a_{11} = 100.40 a_0$, $a_{12} = 98.006 a_0$, $f_z = 11.507\,\text{Hz}$) this formula gives $f_{\text{c}} = 2.91\,\text{Hz}$, while the GPE simulations show $f_c = 3.0\,\text{Hz}$. The residual 3% discrepancy appears as a result of the neglected BEC dynamics in the radial direction [75]. A comparison of the results of the GPE simulations with the analytical formula is presented in figure 2.3. The equation 2.66 describes analytically the branch $a_{12} < a_{11}$ on Fig. 6 in [68]. When $a_{12} > a_{11}$ the treatment is not valid because the effective trapping potential is repulsive in this case, and the shape of the potential outside the condensate should be accounted for.

The effective harmonic potential in Eq. 2.61 affects atoms only within the size of the BEC where the density is non-zero ($|z| < r_{\text{TF}}$). Therefore, Eq. 2.61 is valid only when the characteristic size of the relevant harmonic oscillator eigenstates is less than r_{TF}. As a criterion, we assume that the $n = 0$ and $n = 2$ harmonic oscillator lowest eigenstates have size smaller than r_{TF}:

$$r_{\text{tf}}^2 \gg \frac{5\hbar}{m\omega_{\text{eff}}}, \quad \text{or} \tag{2.67}$$

$$N \gg \frac{2.3}{a_{11}\omega_r^2} \sqrt{\frac{\hbar\omega_z^3}{m}} \left(1 - \sqrt{\frac{a_{12}}{a_{11}}}\right)^{-\frac{5}{4}}. \tag{2.68}$$

When the parameter $a_{11}a_{22} - a_{12}^2$ which defines the miscibility [67, 64] of a two-component BEC is close to 0, the condition 2.68 also defines the components' miscibility. When N is greater than the critical number of atoms, component $|1\rangle$ is spatially separated from component 2 in the ground state of the two-component BEC (Fig. 2.4)

2.4.4 Relative phase evolution

If $n_2 \ll n_1$, the phase evolution rate of component 1 is defined by the chemical potential μ which remains almost the same as before the preparation of the two-component mixture.

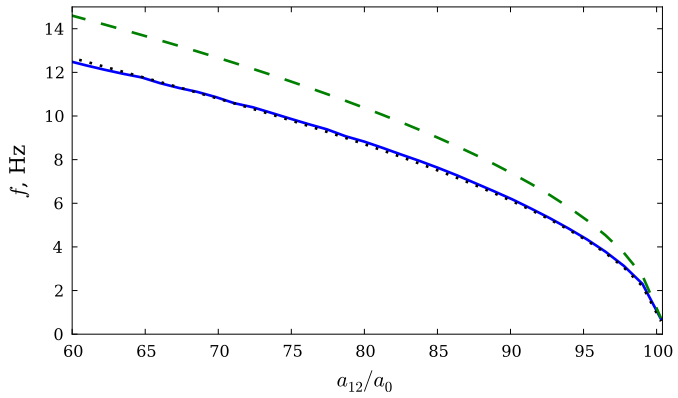

Figure 2.3: Comparison of the analytical model (Eq. 2.66) (dotted line) with the GPE simulations (solid line). The discrepancy between the model and GPE simulations is 3% near the region ($a_{11} - a_{12} \ll a_{11}$). The dashed line is the value predicted by the effective single-component theory in one-dimensional case implied by Eq. 2.26 [71].

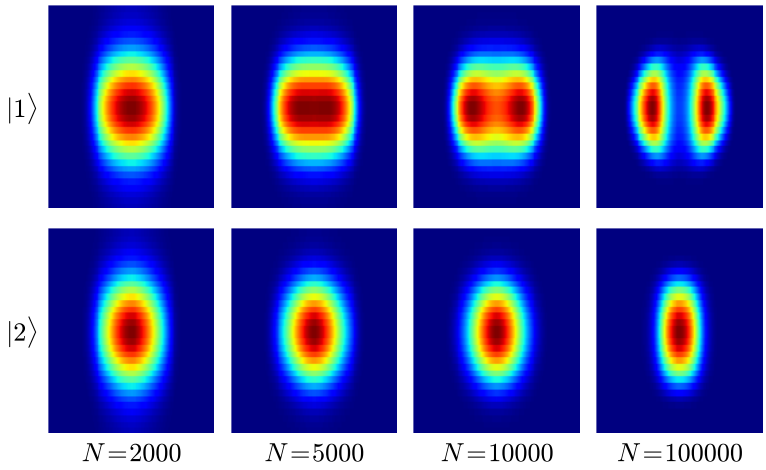

Figure 2.4: Ground states of a two-component BEC having equal populations of states $|1\rangle$ and $|2\rangle$. N is the total number of atoms in the BEC. The critical number of atoms which splits the miscible and separable regimes is $N_c \approx 5 \times 10^3$. Component $|1\rangle$ forms two peaks in the ground state when $N > N_c$ and one peak when $N < N_c$.

The phase evolution of the second component is determined by the sum of a harmonic oscillator phase evolution and the constant phase evolution term in the Hamiltonian of Eq. 2.61 $\mu_{\text{eff}} = \frac{\mu}{3}\left(4\sqrt{\frac{a_{12}}{a_{11}}} - 1\right)$. If an interferometric measurement performed at time t is equal to a multiple of $1/f_c$, the phase of the harmonic oscillator term is always equal to $2\pi k$ and independent of z, i.e., it is uniform along the condensate. This 1D effective treatment clearly predicts that component 2 periodically dephases and rephases with a period of $1/f_c$. The relative phase of the two-component BEC becomes uniform at $t = k/f_c$ ($k \in \mathbb{N}$) and is defined by:

$$\delta\varphi = \frac{\mu - \mu'}{\hbar}t = \frac{t}{\hbar} \cdot \frac{4\mu}{3}\left(1 - \sqrt{\frac{a_{12}}{a_{11}}}\right). \tag{2.69}$$

2.4.5 Order parameter evolution

The effective harmonic oscillator equation (Eq. 2.61) has an analytical solution

$$f_2(t,z) = \sum_{n=0}^{\infty}\left(\int_{-r_{TF}}^{r_{TF}} f_2\left(0,z\right)\, \psi_{ho,n}\left(0,z\right)\, dz\right) e^{-i\omega_{eff}\left(n+\frac{1}{2}\right)t}, \tag{2.70}$$

where $\psi_{h0,n}$ is the n-th harmonic oscillator eigenstate, $f_2(0,z)$ is given by an initial TF profile $|f_1|$ (Eq. 2.56) multiplied by $\sin\left(\theta/2\right)$; only even $n = 0, 2, \ldots$ give a non-zero contribution.

The expansion of the TF profile onto a harmonic oscillator basis can be calculated analytically. It is convenient to express the TF radius of the BEC r_{TF} in terms of an effective harmonic oscillator ground state size $\beta = r_{\text{TF}}\left(\hbar/m\omega_{\text{eff}}\right)^{-1/2}$ replacing z with $\xi = z\left(\hbar/m\omega_{\text{eff}}\right)^{-1/2}$. We define the integrals $I_0(n) = \int_{-\beta}^{\beta}\psi_{ho,n}d\xi$, $I_1(n) = \int_{-\beta}^{\beta}\psi_{ho,n}\xi d\xi$ and $I_2(n) = \int_{-\beta}^{\beta}\psi_{ho,n}\xi^2 d\xi$. Then

$$f_2(t,\xi) = \sum_{n=0}^{\infty}\varepsilon\sqrt{\frac{\hbar}{m\omega_{eff}}}\left(\mu I_0\left(2n\right) - \frac{\omega_z^2}{2}\frac{\hbar}{\omega_{eff}}I_2\left(2n\right)\right), \tag{2.71}$$

where $\varepsilon = \sin\frac{\theta}{2}\sqrt{2/a_{11}}/\left(3\hbar\omega_r\right)$. For the integrals $I_{0,1,2}$ it is possible to derive the following

recursive relations using the symmetry properties of $\psi_{ho,n}$ and integration by parts:

$$\begin{aligned}
I_0(n) =& \sqrt{\frac{n-1}{n}} I_0(n-2) - \frac{2\sqrt{2}}{\sqrt{n}} \psi_{ho,n-1}(\beta), \quad \text{for even } n, \\
I_1(n) =& \sqrt{\frac{n-1}{n}} I_1(n-2) + \sqrt{\frac{2}{n}} I_0(n-1) - \frac{2\sqrt{2}}{\sqrt{n}} \psi_{ho,n-1}(\beta)\,\beta, \quad \text{for odd } n, \\
I_2(n) =& \sqrt{\frac{n-1}{n}} I_2(n-2) + \frac{2\sqrt{2}}{\sqrt{n}} I_1(n-1) - \frac{2\sqrt{2}}{\sqrt{n}} \psi_{ho,n-1}(\beta)\,\beta^2, \quad \text{for even } n,
\end{aligned} \tag{2.72}$$

where the initial integrals are:

$$\begin{aligned}
I_0(0) =& \sqrt{2}\pi^{\frac{1}{4}} \operatorname{erf}\left(\frac{\beta}{\sqrt{2}}\right), \\
I_1(1) =& \frac{2}{\pi^{\frac{1}{4}}} e^{-\frac{\beta^2}{2}} \left(\sqrt{\pi} e^{\frac{\beta^2}{2}} \operatorname{erf}\left(\frac{\beta}{\sqrt{2}}\right) - \sqrt{2}\beta\right), \\
I_2(0) =& \frac{1}{\sqrt{2}} I_1(1).
\end{aligned} \tag{2.73}$$

We use Eqs 2.73 in order to construct the solutions in the form of Eq. 2.71 using the first 20 terms in the sum ($n = 0, 2, \ldots, 38$). The wavefunction of state 1 is expressed as $f_1(t,z) = f_1(0,z)\, e^{-i\mu t/\hbar}$. After the analytic form of the wavefunction f_2 is obtained, the density of the state 2 is $n_2(t,z) = |f_2(t,z)|^2$. We find excellent agreement between the analytical expression and the three-dimensional simulations of the coupled GPE equations (Fig. 2.5). The GPE simulations also contain low-lying single-component collective oscillations with frequency $f_s \approx \sqrt{2.5} f_z = 18.2$ Hz [11], not predicted by the analytics described. The frequency components f_c and f_s and the sidebands $f_s \pm f_c$ are clearly visible in the Fourier spectrum of the component $|2\rangle$ second moment along the z axis $\sigma_z = \langle z\, n_2(z) \rangle_z$ (Fig. 2.6).

Another benchmark of the analytical predictions is performed for the phase evolution. The axial relative number density difference in the Ramsey sequence

$$p_z(t,z) = (n_2(z) - n_1(z))/(n_1(z) + n_2(z)), \tag{2.74}$$

where the 1D densities are obtained by integration across the radial coordinate, is expressed as:

$$p_z(t,z) = \frac{2\mathrm{Im}\left(f_2^*(t,z)\; f_1(t,z)\right)}{|f_1|^2 + |f_2|^2} \tag{2.75}$$

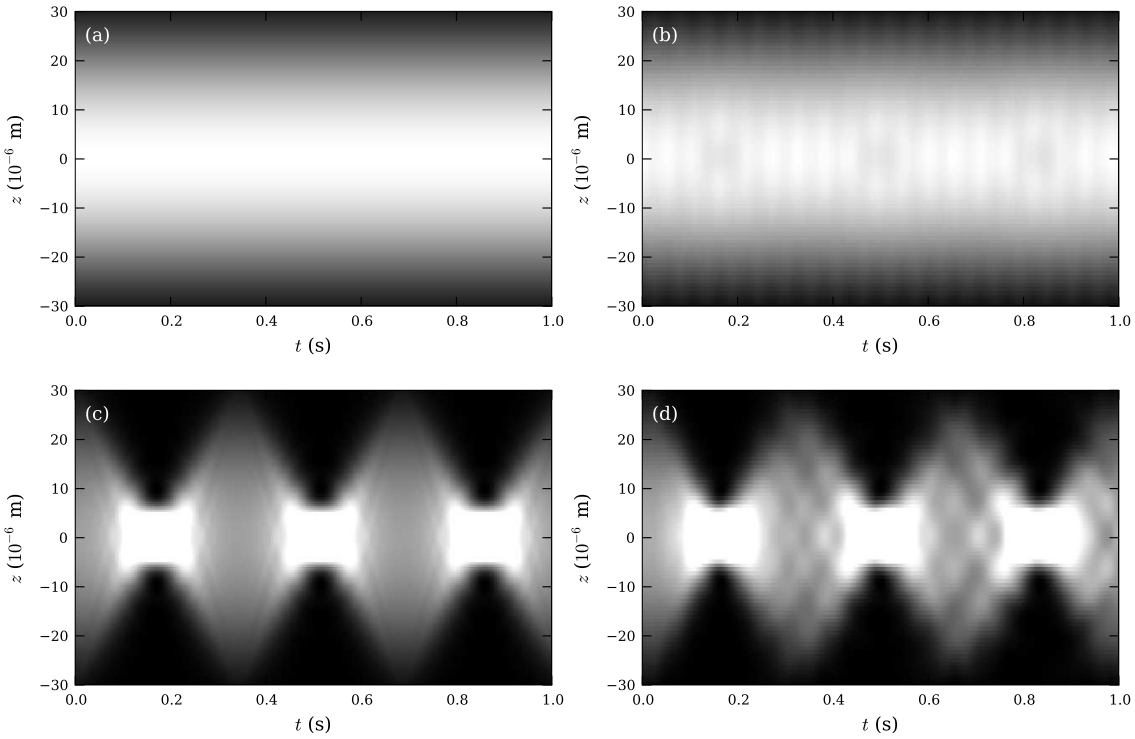

Figure 2.5: Oscillations of the one-dimensional density $|f_2(z,t)|^2$ [(c), (d)] with frequency 2.91 Hz evaluated from Eq. 2.71 (c) and the linear density $n_2(t,z) = |f_2(t,z)|^2$ with frequency 3.00 Hz simulated with the 3D GPE (Eqs. 2.2) (d). Total number of atoms $N = 10^5$. The superposition is prepared by a $\pi/10$-pulse so that the number of atoms in state 2 is $N_2 = 2.4 \times 10^3 \ll N$. During the oscillations of the component $|2\rangle$, density of the component $|1\rangle$ stays almost unperturbed (TF profile (a) vs GPE simulations (b)).

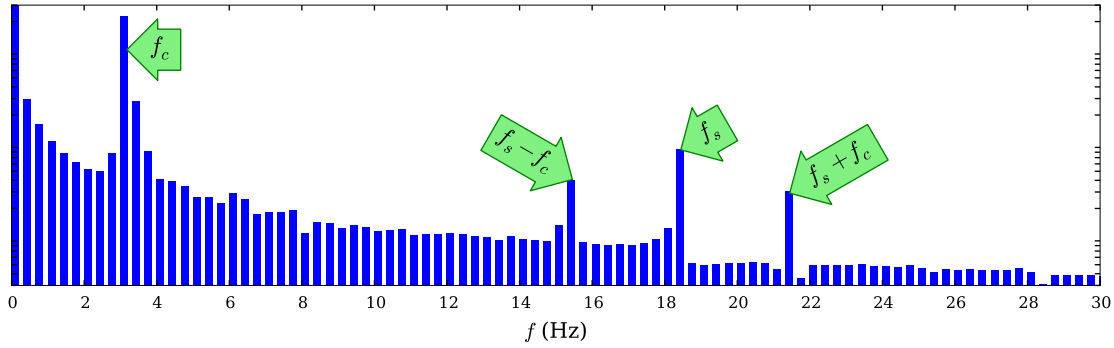

Figure 2.6: Fourier spectrum of the second moment of the component $|2\rangle$ number density during the collective oscillations. The frequencies of the two-component collective oscillations f_c, the low-lying single-component collective oscillations f_s and the sidebands $f_s \pm f_c$ are clearly visible in the spectrum.

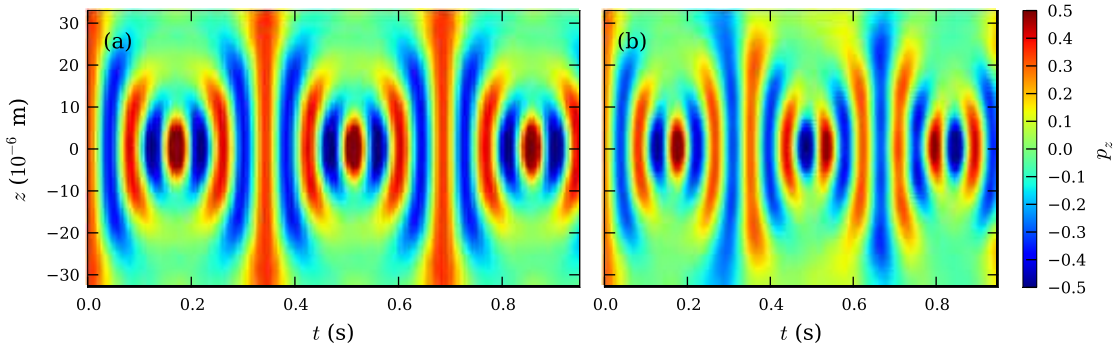

Figure 2.7: Normalized axial density difference in a two-component BEC prepared by a $\pi/10$-pulse and interrogated with a $\pi/2$-pulse. The false color shows the value of $p_z = (n_2(z) - n_1(z))/(n_2(z) + n_1(z))$ representing the local Ramsey fringe for each value of the position in the cloud z. The BEC evolution is performed during time t with radiation detuning $\Delta = 0$, however the transition frequency is perturbed by the collisional shift defining the phase dynamics. Panel (a) is obtained analytically using Eq. 2.71. Panel (b) shows the corresponding results of coupled GPE simulations (Eq. 2.2).

and is a Ramsey fringe plotted for all axial positions. The results of the analytical expression 2.74 are also in agreement with the three-dimensional coupled GPE simulations, however with a slight difference of fringe frequency (Fig. 2.7). As seen from the figure, the phase is uniform along the BEC (the profile $p_z(z,t)$ is not bent) at the points where the component $|2\rangle$ is maximally compressed and when it reaches the initial profile (Fig. 2.5d) with the frequency of collective oscillations. Density of the component $|1\rangle$ stays almost unperturbed during the dynamics when $n_2 \ll n_1$.

Chapter 3

Experimental apparatus

In this chapter we describe the major elements of the experimental setup and the methods used in the experiments throughout the thesis. The existing experimental Atom Chip apparatus was described in detail in the PhD theses of S. Whitlock [78] and R.P. Anderson [64]. In this chapter we describe the experimental sequence and main steps in trapping and cooling of ^{87}Rb atoms and the characterization of the final magnetic trap including trap frequencies, axes and anharmonicity. Resolution of the optical system for imaging cold atomic clouds has been improved through the appropriate use of a pair of achromatic lenses. We set up a dedicated laser diode with narrower linewidth for stable imaging. In addition to that, timing of the probe beam switching was also improved by the synchronization use the AOM intensity control with a mechanical shutter. We developed a fringe removal algorithm which allows the suppression of noise that appears due to a slight difference in interference patterns formed by the light in the absorption and background frames during absorption imaging process (similar to [79]).

3.1 Trapping and cooling on an atom chip

3.1.1 Atom chip

Atom chips are presently widely used for Bose-Einstein condensation experiments [6] providing tight confinement of atoms and strong interactions with the radiation fed to

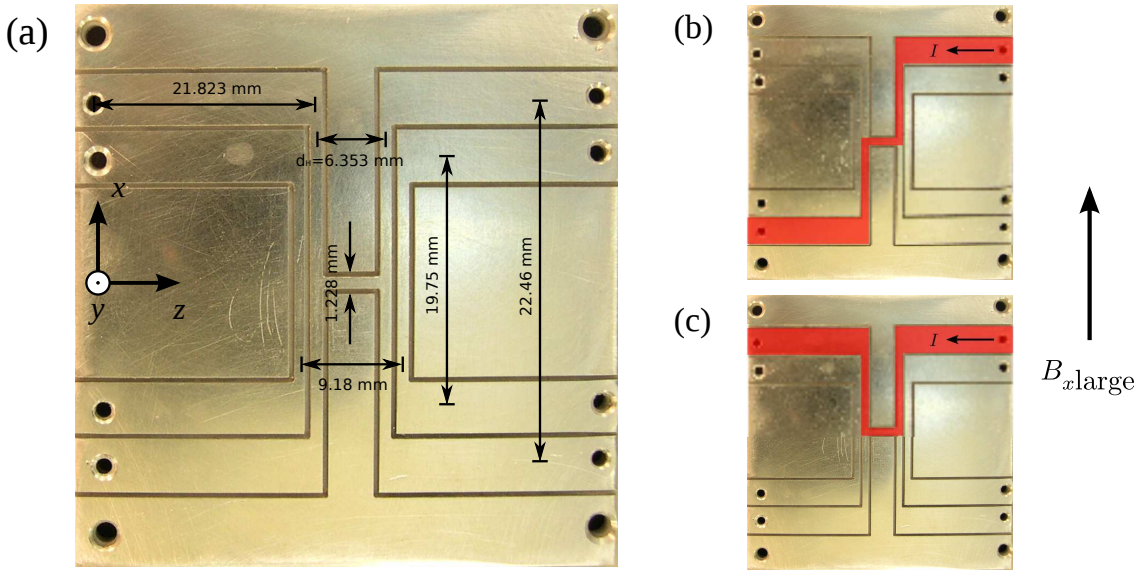

Figure 3.1: (a) The current-carrying wire structure used in the Swinburne atom chip for cooling atoms and production of Bose-Einstein condensates. The coordinate system shown is used throughout the thesis. (b) and (c) Z-wire and U-wire traps are made by a current I passed through the corresponding parts of the wire structure (highlighted in red color) and the magnetic field $B_{x\,\text{large}}$

the chip or on-chip structures. Our atom chip combines a current-carrying wire structure with a mirror surface for use in a reflection magneto-optical trap (MOT). The 100 nm-thick gold film is deposited on a glass substrate with a polished edge. The glass slide was glued to a machined wire structure in a silver foil of thickness 0.5 mm and mounted in an ultra-high vacuum chamber (pressure $\sim 10^{-11}$ torr). The atom chip used to have a magnetised film which was removed in the recent experiments. The configuration of the wire structure with all the useful dimensions for simulating the magnetic field is shown in Fig. 3.1. The chip apparatus is described in detail in the PhD thesis of S. Whitlock [78].

3.1.2 Experimental sequence for Bose-Einstein condensation

We employ the following stages in cooling and producing a quantum degenerate gas of ^{87}Rb atoms:

- mirror magneto-optical trap (MOT) (13.5 s);
- compressed magneto-optical trap on chip (CMOT), or U-wire trap (180 ms);
- polarisation gradient cooling (PGC) in CMOT (8.7 ms);
- optical pumping which transfers atoms to the desired trappable state (1.6 ms);
- loading atoms into magnetic trap (MT) on the chip, or Z-wire trap (5 ms);
- evaporative cooling down to Bose-Einstein condensation (13 s).

We produce hot ^{87}Rb vapour in the UHV chamber using SAES getters (^{87}Rb/NF/-/25/FT 10+10). In order to keep the getters warm, we apply a current of 3.5 A between the cycles. We begin the experimental cycle by applying a current of 5.7 A through the getters for 7 s. We first trap atoms in the MOT made of two diagonal beams, reflecting at 45° from the golden mirror and two counter-propagating horizontal beams parallel to the chip surface [80]. The beams consist of mixed light from trapping and repump lasers. The quadrupole magnetic field is provided by two external coils, arranged in the anti-Helmholtz configuration. We trap approximately 5×10^8 atoms in the MOT in 13.5 s. The number of trapped atoms is monitored with fluorescence detected by a photodiode.

After the MOT stage atoms are transferred in two stages to a CMOT produced by current-carrying wires near the chip surface. The first stage is to transfer atoms to a U-wire compressed magneto-optical trap with the centre located in 4 mm from the chip, realized in 150 ms ramping down the MOT quadrupole magnetic field and ramping up a current of 14.2 A through the U-wire (Fig. 3.1c) along with the magnetic field $B_{x\,\mathrm{large}}$. The second stage transfers the cloud to the CMOT located 2 mm from the chip surface with a 20 ms ramp, by applying a current of 8.2 A through the U-wire.

The temperature of the cloud is limited by Doppler cooling to 146 μK for ^{87}Rb as measured by the time-of-flight (TOF) expansion of the cloud cooled in the CMOT. To

cool the cloud further we implement a polarization gradient cooling (PGC) stage. To achieve that we reduce the magnetic field gradient of the quadrupole field in the CMOT by a factor of 10 and increase the MOT laser detuning up to 45 MHz for 8.7 ms. The temperature of the cloud reduces to 25−30 μK. Next we extinguish the U-wire current, the trapping and repumping lasers and optically pump atoms to $|F = 1, m_F = -1\rangle$ (described in details in Sec. 3.1.3). These steps yield 1.2×10^8 atoms that are magnetically trappable.

After the optical pumping, we switch off U-wire current and transfer atoms into a magnetic trap (MT) with exactly the same spatial position as CMOT and compress it in 250 ms by ramping the Z-wire current from 27.8 A to 37 A and the bias $B_{x\,\mathrm{large}}$ current from 21.7 A to 20.2 A ($B_{x\,\mathrm{large}}$ reaches 42 G). Unwanted atoms remaining in state $|F = 2\rangle$ are deliberately blown away by a 5 ms pulse of the trapping laser. Then, RF evaporative cooling is applied for 13 s in a tight trap (trapping frequencies $\sim (200, 200, 15)$ Hz) with a magnetic field minimum of 0.77 G, where the cloud undergoes Bose-Einstein condensation. Amplitude of the RF signal is kept constant during this process, its frequency is logarithmically ramped from 25 MHz down to 600 kHz. The condensate is then transferred in 0.7 s to a weak magnetic trap (trap frequencies: $(98.25, 100.0, 11.507)$ Hz) located in 0.9 mm from the chip surface with a magnetic field minimum of 3.23 G and evaporated in 2 s down to an almost pure BEC with $N \sim 10^5$ atoms, the RF amplitude is decreased by factor of 5 and the RF frequency is ramped from 2.4 MHz down to 2.3 MHz.

3.1.3 Optical pumping

In order to magnetically trap atoms in the lower hyperfine state, we optically pump them to the $|F = 1, m_F = -1\rangle$ state. One (passive) method is to extinguish the repump light after PGC resulting in atoms spontaneously decaying to $F = 1$ manifold where the state $|F = 1, m_F = -1\rangle$ is predominantly occupied. We use active optical pumping scheme that improves the number of atoms transferred to the magnetically trappable state $|F = 1, m_F = -1\rangle$ by 20%. We apply σ^--polarized light resonant with the $F = 2 \rightarrow F' = 2$ optical transition (Fig. 3.2b) to pump atoms into the $|F = 2, m_F = -2\rangle$ dark state to avoid significant heating that occurs if a cycling transition is used. Simultaneously a σ^- repump

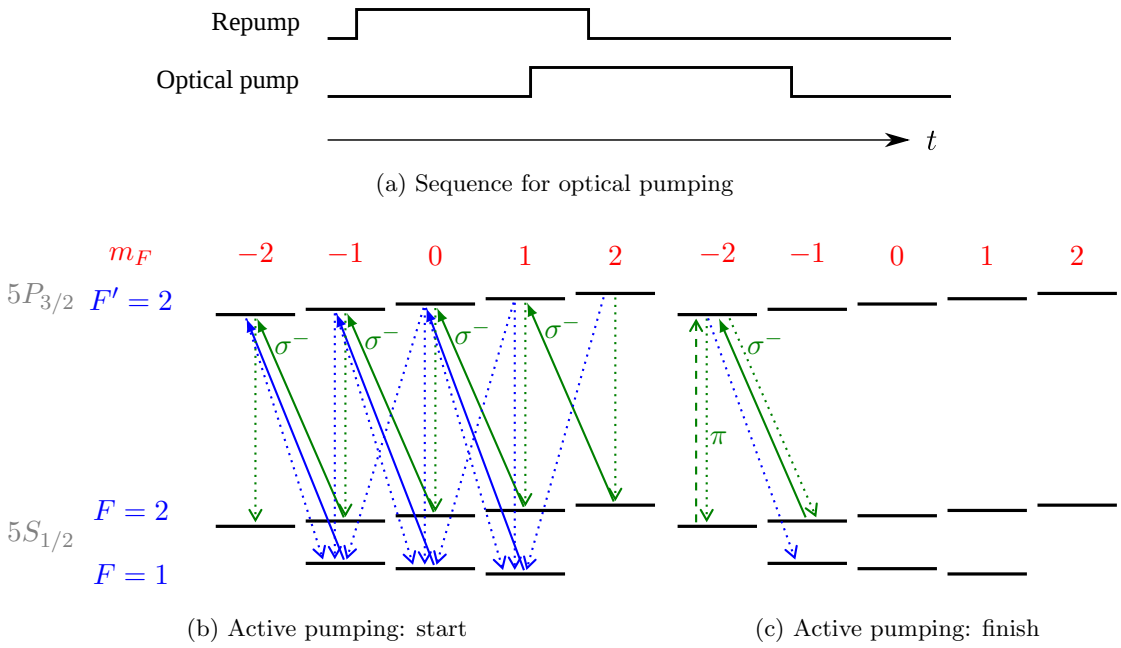

(a) Sequence for optical pumping

(b) Active pumping: start

(c) Active pumping: finish

Figure 3.2: Active optical pumping to the $|F = 1, m_F = -1\rangle$ state using optical pump (green) and repump (blue) lasers. Solid lines show absorption of the laser beams, dotted lines show spontaneous emission. Dashed line shows absorption of a small fraction of π-polarized radiation. The sequence for switching on σ^- polarized repump and optical pump light is drawn in Fig. (a). Firstly, when the radiation of both lasers is applied, atoms are collected in state $|F = 2, m_F = -2\rangle$ (b). Then the repump laser is switched off and almost all the population is transferred to the state $|F = 1, m_F = -1\rangle$ (c).

laser light resonant with the $F = 1 \rightarrow F' = 2$ optical transition is applied (Fig. 3.2b), we use a separate repump channel for this rather than utilizing the repump light present in MOT beams. When the repump laser light is switched off, most of the population is transferred from the $|F = 2, m_F = -2\rangle$ to the $|F = 1, m_F = -1\rangle$ hyperfine ground state via the $|F' = 2, m_F = -2\rangle$ excited state due to the light being deliberately misaligned with the quantization axis resulting in a small amount of π-polarisation being present in the optical pumping laser radiation (Fig. 3.2c).

In the experimental sequence, we weaken the CMOT and red-detune the MOT laser by 40 MHz below the $F = 2 \rightarrow F' = 3$ transition frequency and switch off the repump laser in order to cool the cloud below the Doppler limit. This automatically transfers part of the population to $|F = 1, m_F = -1\rangle$ state. We use active optical pumping after the passive pumping is complete in order to increase the efficiency of the process. This increases the overall optical pumping efficiency from $\sim 80\%$ to 97%. It is important to limit the time of the active optical pumping in order to maintain a good spatial overlap of the cloud with the position of MT and not to introduce extra heating from scattering of multiple photons.

3.1.4 Magnetic traps on a chip

In order to establish ways for manipulating the traps, we derive simple analytical formulae describing their parameters. Consider an infinite wire with a current I. Applying a bias magnetic field $\mathbf{B}_b$ perpendicular to the wire we create a zero of the magnetic field at a distance r_0 from the wire

$$r_0 = \frac{\mu_0 I}{2\pi B_b}. \tag{3.1}$$

In this trap the magnetic field gradient is:

$$\left|\frac{dB}{dr}\right| = \frac{\mu_0 I}{2\pi r_0^2} = \frac{2\pi B_b^2}{\mu_0 I}. \tag{3.2}$$

Atoms can be trapped very close ($\sim$ 1 mm) to the chip surface and the wires can carry currents up to 40 A. Thus we can produce magnetic field gradients of more than a hundred

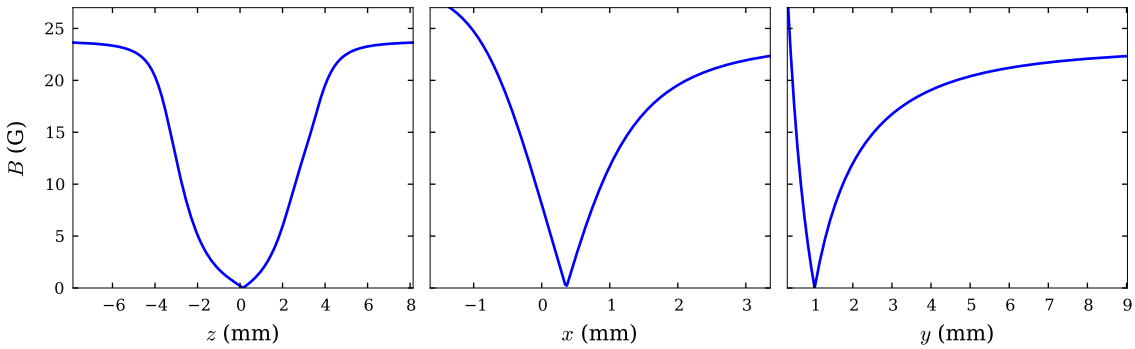

Figure 3.3: Cross-sections of the magnetic field in the U-wire CMOT produced by $B_b = 23.8$ G and $I = 15.3$ A. The magnetic field gradient at the zero magnetic field is $dB/dy = 185$ G/cm. The axes are labelled according to the coordinate system shown in Fig. 3.1.

G/cm. A trap made of such an infinite wire does not provide any confinement along the wire.

In order to make a three-dimensional quadrupole magnetic field, we use a U-shaped wire cut in silver foil (Fig. 3.1) [6]. Its magnetic field is similar to that produced by quadrupole coils and, therefore, can be used for the CMOT (Fig. 3.3). A magnetic trap with zero field in the middle will lose atoms due to spin-flips as they become cold. In order to evaporate the clouds down to Bose-Einstein condensation, we use a Z-shaped wire. In combination with an external bias magnetic field $\mathbf{B}_b$, this configuration produces a harmonic trap analogous to a Ioffe-Pritchard trap [4, 5] (Fig. 3.4). We apply an additional magnetic field $\mathbf{B}_{\parallel}$ along the z axis in order to adjust the magnetic field in the trap bottom B_0. In the approximation of semi-infinite end-wires, an infinite middle wire and $r_0 \ll d_H$ (Fig. 3.1), the magnetic field in the vicinity of the trapping potential minimum is (keeping terms up to second order in the expansion):

$$B(x,y,z) = B_0 + \frac{\left(x^2+y^2\right)}{2B_0}\left(\frac{2\pi B_b^2}{\mu_0 I}\right)^2 + \frac{2\mu_0 r_0 I d_H^2 z^2}{\pi\left(d_H^2+r_0^2\right)^3}. \tag{3.3}$$

From this, one can obtain the trap frequencies for atoms with mass m and magnetic

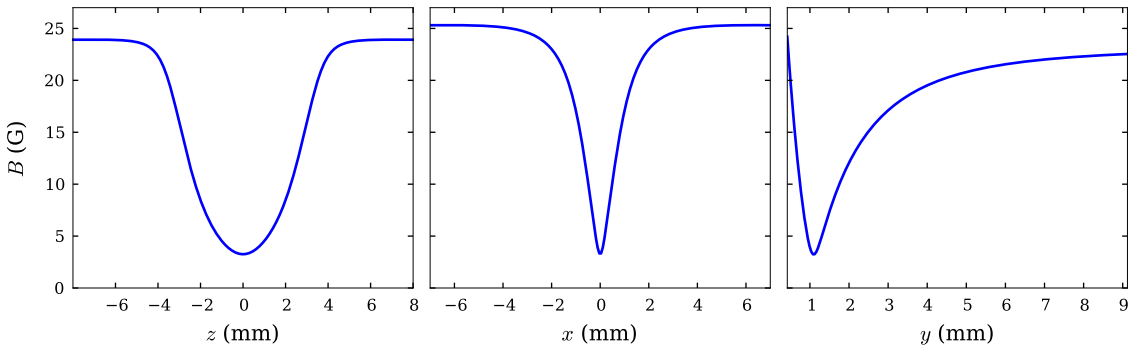

Figure 3.4: Cross-sections of the magnetic field in the Z-wire magnetic trap produced by $I = 15.3$ A, $B_b = 23.8$ G, $B_0 = 3.23$ G.

moment $\mu_B/2$:

$$\omega_x = \omega_y = \frac{2\pi B_b^2}{\mu_0 I}\sqrt{\frac{\mu_B}{2mB_0}}, \tag{3.4}$$

$$\omega_z = \frac{\mu_0 I d_H}{\pi}\sqrt{\frac{\mu_B}{mB_b\left(d_H^2 + r_0^2\right)^3}}. \tag{3.5}$$

For our usual parameters ($I = 15.3$ A, $B_0 = 3.23$ G, $B_b = 23.8$ G, $d_H = 6.353$ mm) we find $\omega_x = \omega_y = 2\pi \times 93$ Hz, $\omega_z = 2\pi \times 12$ Hz.

These simple analytical formulae produce estimates close to the results of the experimental measurements. However in order to include the finite size effects of the wires we numerically integrate Biot-Savart's law. In order to calculate this, we represent the wire structure on the chip as a number of thin, long pieces **AB**. The magnetic field $\delta\mathbf{B}$ at a point C from such a piece is:

$$\delta\mathbf{B} = \frac{\mu_0}{4\pi}\frac{\mathbf{AB}\times\mathbf{AC}}{|\mathbf{AB}\times\mathbf{AC}|^2}\left[\left(-\frac{\mathbf{BC}}{|\mathbf{BC}|} + \frac{\mathbf{AC}}{|\mathbf{AC}|}\right)\cdot\mathbf{AB}\right]. \tag{3.6}$$

The simulated results for the magnetic fields of the U-wire and the Z-wire magnetic traps are represented in Figs. 3.3 and 3.4. In order to calculate the trapping frequencies of the Z-wire trap, we adjust the magnetic field $B_{||} = 0.28$ G in such way that $B_0 = 3.23$ G ($B_b = 23.8$ G, $I = 15.3$ A). We find $\omega_z = 2\pi \times 9.8$ Hz, $\omega_x = 2\pi \times 101.9$ Hz and $\omega_y = 2\pi \times 99.1$ Hz. This is in reasonable agreement with our experimental results

$\omega_z = 2\pi \times 11.507$ Hz, $\omega_y = 2\pi \times 98.23$ Hz. We find ω_x by multiplying ω_y by the ratio ω_x/ω_y obtained in simulations of the Z-wire trap magnetic field. Due to the small asymmetry of the Z-wire, the main axis of the harmonic magnetic trap is rotated by 0.107 rad with respect to the z axis. The magnetic field in the trap is, however, directed along the main axis of the trap.

When the atomic cloud is placed in a gravitational field, the potential minimum of the trap shifts down and the atoms are not positioned in the magnetic field minimum anymore. The potential energy of an atom with magnetic moment μ_m in the trap is:

$$E_p(x, y, z) = \mu_m B(x, y, z) - mgy. \tag{3.7}$$

The magnetic field gradient which holds atoms with magnetic moment μ_m is $B' = mg/\mu_m$ which is equal to 31 G/cm for the magnetic moment of $\mu_B/2$. If atoms in different spin-states have different magnetic moments, this shifts the potential minima of the trapping potentials seen by those atoms. If atoms with magnetic moments μ_1 and μ_2 are placed in the magnetic trap with a field given by Eq. 3.3, the separation between the potential minima is:

$$\delta y = \frac{g}{\omega_1^2}\left(\frac{\mu_1}{\mu_2} - 1\right), \tag{3.8}$$

where ω_1 is the radial trapping frequency along the direction of gravity for the atoms with magnetic moment μ_1; anharmonicity of the trapping potential is neglected. For $\omega_1 = 2\pi \times 98.23$ Hz, $\mu_1 = \mu_B/2$ and $\mu_2 = \mu_B$ the separation $\delta y = -13$ µm, i.e., atoms with the magnetic moment μ_2 are closer to the chip surface. Equation 3.8 can be also used in the presence of a quadratic Zeeman effect; however in this case the magnetic moments μ_1 and μ_2 should be replaced by the derivatives of the magnetic potential energy dE_p/dB. The effect of this on atoms with the same magnetic moment but different quadratic Zeeman shift will be considered in the next section after consideration of the Breit-Rabi formula.

Trapping anisotropy can significantly affect atomic scattering leading to confinement-induced resonances [81, 82]. We use the calculated trap anisotropy to check the effect of this on our scattering lengths measurements (Ch. 6). The most significant anharmonicity of our trap is that of third order in the y direction, whereas the trap is symmetric along

x and z which excludes third order anharmonicity along those directions. The magnetic field along y is:

$$B(y) = \sqrt{\left(B_b - \frac{\mu_0 I}{2\pi\,(y + r_0)}\right)^2 + B_0^2}. \tag{3.9}$$

Here we emphasize that we do not limit equation 3.9 to the use of just zero and second order terms like it was done with Eq. 3.3, and Eq. 3.9 expanded to second order is equivalent to Eq. 3.3 with $x = z = 0$. We expand Eq. 3.9 to fourth order around r_0:

$$B(y) = B_0 + \frac{2\pi^2 B_b^4}{\mu_0^2 B_0 I^2} y^2 - \frac{8\pi^3 B_b^5}{\mu_0^3 B_0 I^3} y^3 - \frac{2\pi^4 B_b^6 \left(B_b^2 - 12 B_0^2\right)}{\mu_0^4 B_0^3 I^4} y^4 + O(y^5). \tag{3.10}$$

This expansion is used to calculate the third order anharmonicity in the presence of a gravitational potential, where the trap is shifted down by g/ω_y^2. The anharmonic potential with third order (α_{3y}) and fourth order (α_{4y}) anharmonicities is usually represented as [82]:

$$E_p(y) = \frac{1}{2} m \omega_y^2 y^2 \left(1 + \alpha_{3y} \frac{y}{a_y} + \alpha_{4y} \left(\frac{y}{a_y}\right)^2\right), \tag{3.11}$$

where $a_y = (\hbar/m\omega_y)^{1/2}$ is the harmonic oscillator length. Therefore, for atoms with magnetic moment $\mu_B/2$ the third order anharmonicity of the trapping potential in the gravitational field of the Earth is:

$$\begin{aligned} \alpha_{3y} &= \frac{\mu_B a_y}{3!\, m\omega_y^2} \frac{d^3 B(\delta y)}{dy^3} \\ &= -\frac{mg\mu_0 I \left(B_b^2 - 12 B_0^2\right) + 2\pi \mu_B B_0 B_b^3}{\mu_B B_b^3} \sqrt{\frac{\hbar}{\pi \mu_0 I}} \left(\frac{8}{\mu_B m B_0^3}\right)^{1/4}. \end{aligned} \tag{3.12}$$

Equation 3.12 gives $\alpha_{3y} = 1.7 \times 10^{-3}$ when $g = 0$ and $\alpha_{3y} = 2.5 \times 10^{-3}$ when gravity is present. We calculate the third and fourth order anharmonicities along different axes numerically (Tab. 3.1)

Accurate knowledge of the harmonic trap frequencies (especially f_z) is crucial for precision measurements. We employ a standard method of dipole oscillations by shifting the trap by half of a cycle, returning to its original position and monitoring periodic oscillations of a BEC in state $|1\rangle$. However, due to small trap anharmonicities the frequency of the oscillations depends on their amplitude. We derive this dependence using the

	x	y	z
α_3	0	2.5×10^{-3}	0
α_4	-1.2×10^{-5}	-6.8×10^{-6}	1.6×10^{-6}

Table 3.1: Anharmonicities of the third (α_3) and the fourth (α_4) order along different directions calculated in the presence of gravity for our chip geometry and the magnetic trap used in all experiments ($B_0 = 3.23$ G, $I = 15.3$ A and $B_b = 23.8$ G)

Rayleigh-Ritz variational method [83]. Classical Hamiltonian of an anharmonic oscillator can be written as:

$$H = K + \frac{m\omega_0^2 x^2}{2} + b_3 x^3 + b_4 x^4, \qquad K = \frac{m\dot{x}^2}{2}, \tag{3.13}$$

where $b_3 = m\omega_0^2 \alpha_3/(2a_{\mathrm{ho}})$, $b_4 = m\omega_0^2 \alpha_4/(2a_{\mathrm{ho}}^2)$, a_{ho} is the harmonic oscillator length and ω_0 is trapping potential frequency. In order to find the oscillation frequency ω we use a trial trajectory:

$$x = A \sin \omega t + B, \tag{3.14}$$

where the amplitude A is known. Importantly, the shift B has to be introduced in order to treat odd order anharmonicities properly. Maupertuis' action [84] can be written as

$$W = \int_0^{2\pi/\omega} 2K \, dt = \pi m \omega A^2. \tag{3.15}$$

The mean energy of the system is

$$\begin{aligned} \bar{E} &= \frac{\omega}{2\pi} \int_0^{2\pi/\omega} H \, dt \\ &= b_4 B^4 + b_3 B^3 + \left(3b_4 A^2 + \frac{m\omega_0^2}{2}\right) B^2 + \frac{3}{2} b_3 B A^2 + \frac{3}{8} b_4 A^4 + \frac{mA^2\left(\omega^2 + \omega_0^2\right)}{4}. \end{aligned} \tag{3.16}$$

From the variational principle

$$\left(\frac{\partial \bar{E}}{\partial \omega}\right)_W = 0, \qquad \left(\frac{\partial \bar{E}}{\partial B}\right)_W = 0. \tag{3.17}$$

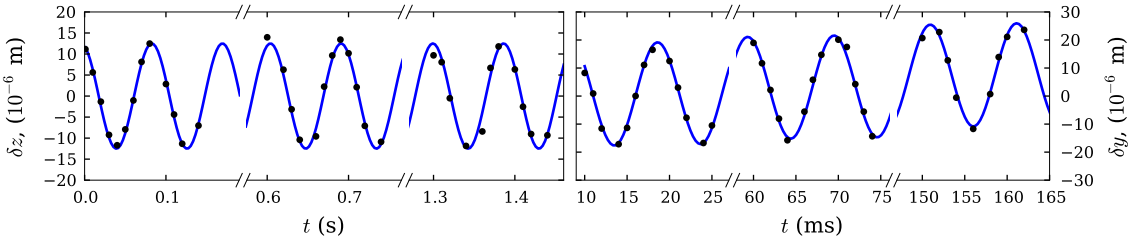

(a) Axial trap frequency f_z (b) Radial trap frequency f_y

Figure 3.5: Trap frequency measurements from dipole oscillations of a BEC. The oscillations are excited by a change in Z-wire current or an end-wire current pulse for half a period of the oscillations. The BEC is held in a trap for a variable time t and its picture is taken after 6.6 ms of free expansion.

Assuming $\alpha_3 A \ll a_{\rm ho}$ and $\alpha_4 A \ll a_{\rm ho}$ we find:

$$\omega^2 = \omega_0^2 \left(1 - \frac{9m\omega_0}{4\hbar}\alpha_3^2 A^2 + \frac{3m\omega_0}{2\hbar}\alpha_4 A^2 + \frac{27\alpha_3^2\alpha_4 m^2\omega_0^2}{8\hbar^2}A^4\right). \tag{3.18}$$

The fourth order term can be neglected at small amplitudes A. In our case, ω_y is less than ω_{0y} by the amount $2\pi \times 0.019$ Hz. However, the shift of ω_z is negligible.

We measure the trap frequencies f_y and f_z with dipole oscillations of a BEC in a magnetic trap (Fig. 3.5). The oscillations are excited by a half-a-period kick with Z-wire or end-wire current pulses. The position of the BEC is measured after $t_{\rm drop} = 6.6$ ms of free expansion. If an object is oscillating in a harmonic trap with amplitude A_0 and frequency ω_0, the momentum is converted to the position after free expansion and the amplitude is equal to $A = A_0(1 + \omega_0^2 t_{\rm drop}^2)^{1/2}$, i.e., the observed amplitude is amplified compared to the amplitude in trap. The measurements yield an "axial" trap frequency $\omega_z = 2\pi \times 11.507(7)$ Hz and a "radial" trap frequency $\omega_y = 2\pi \times 98.23(5)$ Hz. The corresponding amplitudes of oscillations after free expansion (in trap) are $A_z = 12.5(3)$ μm ($A_{0z} = 11.3(3)$ μm) and $A_y = 18.3(3)$μm ($A_{0y} = 4.36(7)$μm). Anharmonicity does not cause a shift in ω_z but ω_y is shifted so that $\omega_{0y} = 2\pi \times 98.25(5)$ Hz. We cannot measure the trap frequency ω_{0x}; however we calculate ω_{0x}/ω_{0y} using the model of the atom chip and calculate the corresponding value of the trap frequency: $\omega_{0x} = 2\pi \times 101.0(5)$ Hz. During

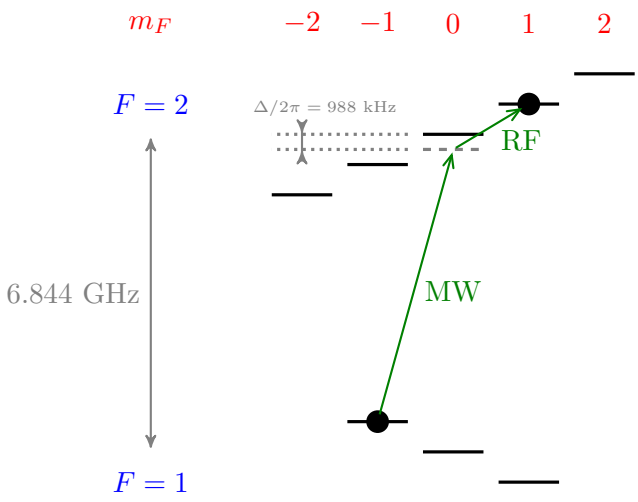

Figure 3.6: Level diagram of the lowest hyperfine states in ^{87}Rb. In our experiments we use two Zeeman sublevels $|F = 1, m_F = -1\rangle$ and $|F = 2, m_F = 1\rangle$ coupled by a two-photon microwave (MW) plus radiofrequency (RF) transition.

the measurement of the "radial" trap frequency, the dependence of the trap position on the hold time t is observed which, however, does not significantly affect the trap frequency (Fig. 3.5b). This was due to a grounding problem with the switching circuitry of the Z-wire, which has now been resolved.

3.2 Atomic system and magnetic dipole coupling

In our experiments we use the two lowest hyperfine levels in ^{87}Rb separated by 6.834 GHz (Fig. 3.6). From all the Zeeman sublevels we choose $|1\rangle \equiv |F = 1, m_F = -1\rangle$ and $|2\rangle \equiv |F = 2, m_F = 1\rangle$ with the same magnetic moment in order to make two BECs trapped at exactly the same position in the presence of gravity and to make our system insensitive to magnetic field noise.

3.2.1 Atomic system

There are two hyperfine ground states in ^{87}Rb: with $F = 1$ and $F = 2$ in the $5\,^2\mathrm{S}_{1/2}$ state (Fig. 3.6). They have three and five Zeeman sublevels, respectively. In low fields ($B \ll 10^3$ G) the magnetic moment is $\mu_1 \approx -m_F\mu_B/2$ for the $F = 1$ atoms, and $\mu_2 \approx m_F\mu_B/2$ for the $F = 2$ atoms. However there is a slight difference between μ_1 and μ_2 due to the quadratic Zeeman effect. It is convenient for our purposes to use a differential analogue to the magnetic moment $\mu_d = dE/dB$ where the magnetic potential energy E is calculated using Breit-Rabi formula. To construct the two-component BEC we choose a pair of states with the same magnetic moment: $|F = 1, m_F = -1\rangle$ and $|F = 2, m_F = 1\rangle$ since they are the only magnetically trappable couple of states with the same magnetic moment.

Atoms of ^{87}Rb have electron angular momentum quantum number $J = 1/2$ in the ground state, the nuclear angular momentum is $I = 3/2$, and the g-factors g_J and g_I are given in [85]. The Zeeman energies of atoms with $J = 1/2$ in a magnetic field B can be precisely calculated using the Breit-Rabi formula [86, 85]:

$$E(F, m_F, B) = -\frac{\Delta E_{\mathrm{hfs}}}{2(2I+1)} + g_I\mu_B m_F B + s\,\mathrm{sign}(F-I)\frac{\Delta E_{\mathrm{hfs}}}{2}\sqrt{1 + \frac{4m_F x}{2I+1} + x^2}, \quad (3.19)$$

where $x = (g_J - g_I)\mu_B B/\Delta E_{\mathrm{hfs}}$ and $s = \mathrm{sign}(1-x)$ if $m_F = -I - 1/2$ or $s = 1$ otherwise, $\Delta E_{\mathrm{hfs}} \approx 2\pi\hbar \times 6.83462861090429(9)$ GHz is the hyperfine splitting energy. The negative sign of $F - I$ for $F = 1$ leads to magnetic moments with a sign opposite to that of m_F quantum number in weak magnetic fields.

Sometimes it is convenient to make an expansion of the Eq. 3.19 for calculating the differences of two Zeeman energies in the vicinity of so-called "magic" points, where the difference in Zeeman energies of the two levels is independent of B to first order. The splitting between the magnetically trappable states $|F = 1, m_F = -1\rangle$ and $|F = 2, m_F = 1\rangle$ currently used in this work [21] is

$$\begin{aligned} E(2, 1, B - B_0) - E(1, -1, B - B_0) &= 2\pi\hbar\left[f_0 + \beta(B - B_0)^2\right], \\ f_0 = 6\,834\,678\,113.59\ \mathrm{Hz}, &\qquad \beta = 431.35947\ \mathrm{Hz/G^2}, \end{aligned} \quad (3.20)$$

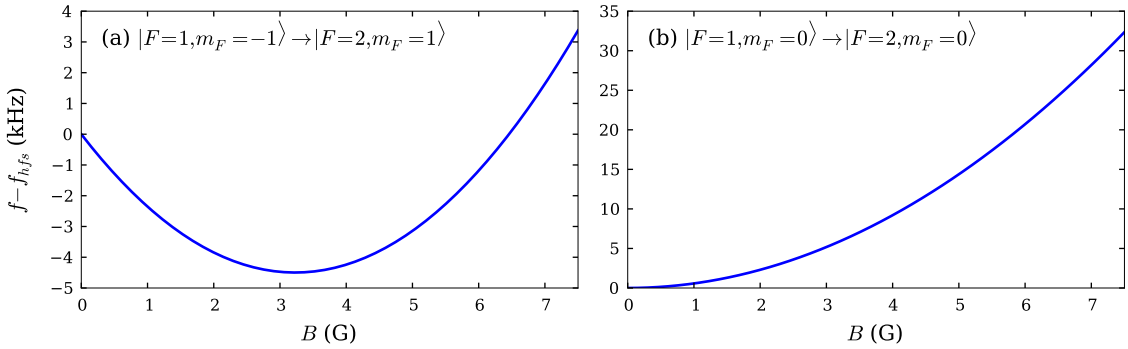

Figure 3.7: Frequencies of the transitions $|F=1, m_F=-1\rangle \rightarrow |F=2, m_F=1\rangle$ (a) and $|F=1, m_F=0\rangle \rightarrow |F=2, m_F=0\rangle$ (b) relative to the hyperfine splitting frequency $f_{\rm hfs} = E_{\rm hfs}/h$. The first order Zeeman shift is cancelled at 3.23 G (a) and 0 G (b) correspondingly. The dependence of the transition frequency on the magnetic field is almost parabolic.

where $B_0 = 3.228917$ G is the "magic" field for these states (Fig. 3.7a). For comparison, the splitting between the "clock" levels $|F=1, m_F=0\rangle$ and $|F=2, m_F=0\rangle$ is:

$$\begin{gathered} E(2,0,B) - E(1,0,B) = 2\pi\hbar \left[f_0 + \beta B^2 \right], \\ f_0 = \Delta E_{\rm hfs}, \qquad \beta = 575.146 \text{ Hz/G}^2. \end{gathered} \tag{3.21}$$

This means that if one wants differential magnetic field noise insensitivity for the states $|F=1, m_F=-1\rangle$ and $|F=2, m_F=1\rangle$, a magnetic field close to B_0 is required (Fig. 3.7a). For the clock states $|F=1, m_F=0\rangle$ and $|F=2, m_F=0\rangle$ the preferable magnetic field is close to zero (Fig. 3.7b); however this might be problematic due to Majorana spin-flips. The expansions (3.20) and (3.21) are valid for weak magnetic fields when $x \ll 1$, or $B \ll 2.4$ kG. When one operates at a magnetic field B_0, noise from external magnetic field fluctuations with an RMS value of δB lead to noise in the difference between Zeeman splittings $\delta E/2\pi\hbar = \beta\, \delta B^2/2$. However if $|B - B_0| \gg \delta B$, $\delta E/2\pi\hbar = 2\beta\, B_0\, \delta B$. The last case is very important for the pair of states $|F=1, m_F=0\rangle$ and $|F=2, m_F=0\rangle$ since $B_0 = 0$ and it is not possible to use $B = 0$ in traps.

We want to account for the non-zero difference in the second-order Zeeman shift,

which makes the potential minima of the magnetic traps for such atoms different in the presence of gravity. The difference in the magnetic potential energies of the atoms $dE_2/dB - dE_1/dB = 2\beta(B - B_0) \ll \mu_m$. Therefore, we derive the shift in position between the trapping potential minima using a Taylor expansion of Eq. 3.8

$$\delta y = \frac{4\pi\hbar\beta(B - B_0)g}{\mu_m\omega^2}, \tag{3.22}$$

while for states $|F = 1, m_F = -1\rangle$ and $|F = 2, m_F = 1\rangle$ $\mu = \mu_B/2$. For these states and our radial trap frequency 98.25 Hz, the shift in position between trapping potentials is conveniently expressed as $\delta y = 31.6$ nm/G $\times (B - B_0)$. This dependence can be used to finely adjust the potential splitting for adjusting the nonlinearity in a two-component BEC.

3.2.2 Microwave and radio-frequency setup

We use microwave (MW) radiation for a variety of purposes: MW spectroscopy, two-photon coupling pulses and the adiabatic transfer of atoms from one hyperfine state to another for dual-state imaging. The microwave signal is produced by a microwave synthesizer (Agilent E8527D) with a typical power of 3 dBm. The low power MW signal goes to a reflective switch (Agilent N9397A) and can be switched between 50 Ω terminator and a 10 W MW amplifier (Fig. 3.8). The microwave switch is able to change the output channel from the 50 Ω terminator to the MW amplifier in order to turn the MW radiation on but switching the output back to 50 Ω terminator has a 100 μs delay. In order to avoid uncontrolled MW coupling when atoms are released from the trap, the experimental sequence has a 0.2 ms delay relative to the MW trigger pulse. For use in the two-photon MW+RF $\pi/2$ splitting we switch on the MW radiation 0.1 ms earlier than the RF radiation in order for the amplitude of the MW field to stabilise. The amplified MW signal is applied to a microwave antenna through a unidirectional coupler and a circulator. The unidirectional coupler transfers 1% of the MW power to a power meter (Agilent E4418D). The radiation is coupled to the atomic system via a half-wave dipole MW antenna made for 6.8 GHz radiation, located close to a window of the experimental setup, about 12 cm

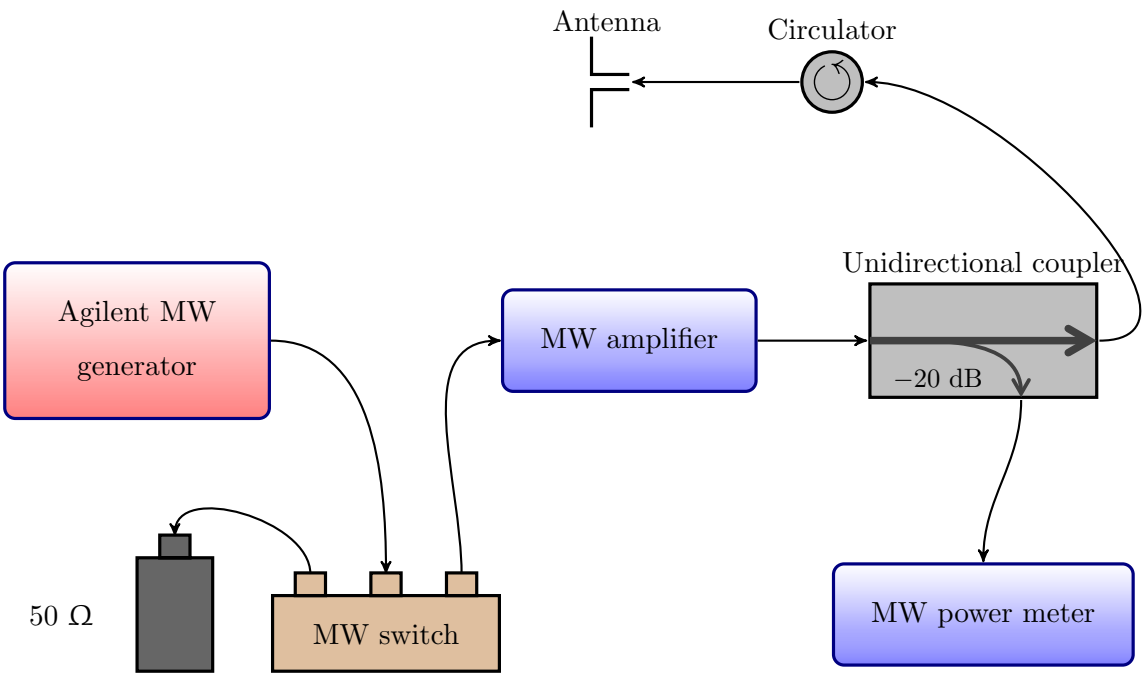

Figure 3.8: Setup for producing and delivering microwave radiation to the atomic system. The signal synthesized by the Agilent MW generator is switched between the 50 Ω terminator and the MW amplifier. After the amplifier it goes to a half-wave dipole antenna through a unidirectional coupler and a circulator. A small part of the signal (−20 dB) is branched off to a MW power meter.

from the atoms. SMA (SubMiniature version A) cables are used to transfer the MW signal between the devices.

Using two side-wires on a chip, we couple the RF radiation to a cloud of ^{87}Rb atoms (Fig. 3.9). The wires on the chip are connected in series in such a way that they produce a linearly polarised magnetic field in the direction perpendicular to the plane of the atom chip and, hence, to the quantization axis. The linear polarisation will produce equal amounts of σ^+ and σ^- RF radiation. We use four different RF generators (SRS DS345) to produce RF fields for a number of purposes: evaporative cooling in two stages, RF field contribution to the two-photon coupling and studying RF-induced Feshbach resonances. The generators are connected to a single 25 W RF amplifier (OphirRF 5303055) via two absorptive switches (Mini-Circuits ZX80-DR230+). RF radiation for evaporative cooling is provided by two synthesizers marked as "Evap. RF 1" and "Evap. RF 2" (Fig. 3.9). The amplitudes of both signals are controlled by a LabView program developed by S. Whitlock [78]. The RF fields for evaporation are switched on by the "RF switch 1" upon the application of a 5 V TTL signal on the "Control 1" input. RF radiation for two-photon coupling and other purposes (such as Rabi oscillations or RF-induced Feshbach resonances) are produced by the "2-photon RF" and "Optional extra RF" synthesizers. Both are controlled by the "Control 3" input which chooses between two synthesizers and the "Control 2" input which turns the signal on and off. The signal from "RF switch 2" is connected to the same amplifier via "Switch 1". All RF switches have a switch-on delay of 12 µs; however it is highly stable and does not change.

3.2.3 RF and MW spectroscopy

In order to characterize the coupling of atoms to electromagnetic field through magnetic dipole transitions we use the treatment fully described in R. P. Anderson's PhD thesis (Chapter 3 in [64]). For atoms in the hyperfine manifold with total atomic angular momentum F the Landè g-factor can be expressed as

$$g_F \approx g_J \frac{F(F+1) - I(I+1) + J(J+1)}{2F(F+1)}, \tag{3.23}$$

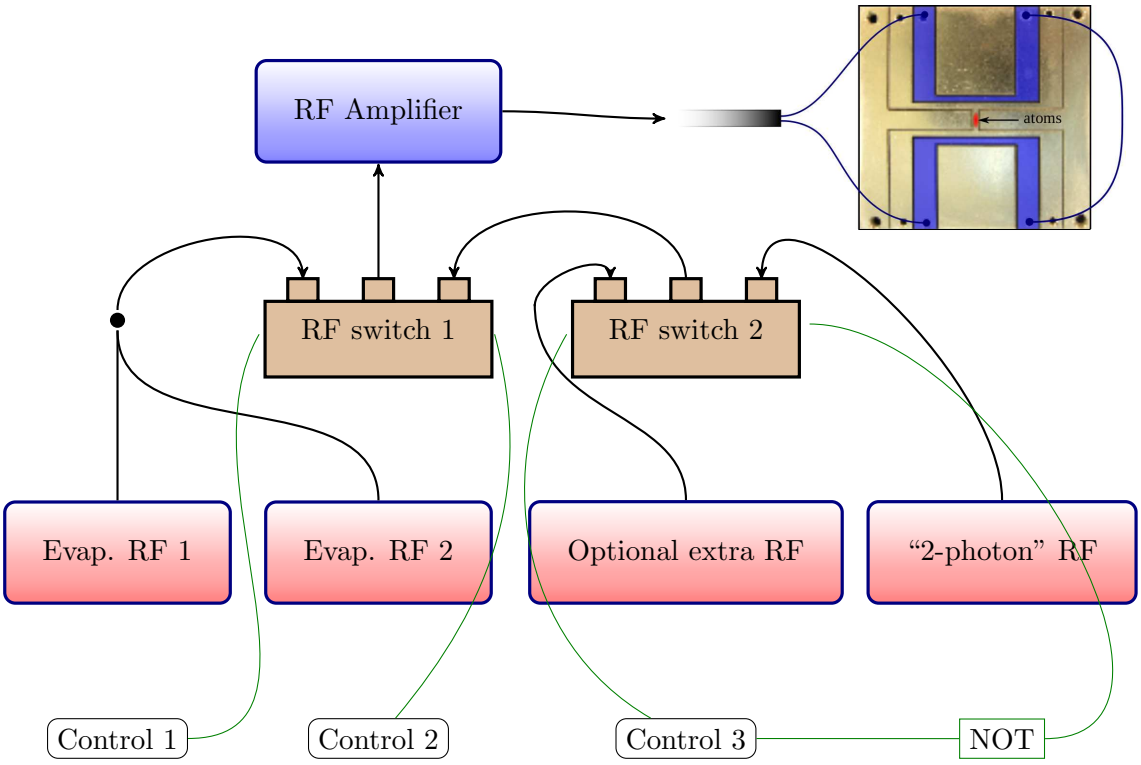

Figure 3.9: Scheme for feeding linearly polarized RF radiation to the atomic system on the chip. The switching circuit chooses from 3 signal inputs: mixed evaporation RF signal, “2-photon RF” or “Optional extra RF”. The RF switch 1 chooses between evaporation (Control 1 switched on) and the signal from RF switch 2 (Control 2 switched on); it can also provide no RF signal (Controls 1 and 2 are switched off). RF switch 2 provides either the RF signal for the two-photon coupling (Control 3 switched off) or for the creation of RF-induced Feshbach resonances (“Optional extra RF”, Control 3 switched on). The RF signal from switch 1 is fed to the atom chip after amplification. The RF radiation is created by two end-wires on the chip (highlighted in blue).

where $g_J \approx 2$ is the electron orbital g-factor and the nuclear factor g_I is neglected. The two lower hyperfine states of ^{87}Rb atom have $g_{F=1} \approx -1/2$, $g_{F=2} \approx 1/2$. For treating $\sigma^{\pm}$ and π-transitions we introduce a coupling strength Ω_0 which, in general, does not coincide with the Rabi frequency but is proportional to it:

$$\Omega_0 = \frac{\mu_B g_F B}{2\hbar}, \tag{3.24}$$

where for $\sigma^{\pm}$ transitions $B \equiv B_{\perp}$ is the component of the magnetic field perpendicular to the quantization axis and for π-transitions $B \equiv B_{\parallel}$ is the component of magnetic field parallel to the quantization axis, and the quantization axis is co-directed with the vector of time-independent magnetic field in the trapping potential minimum. In our experiments the RF magnetic field is coupled to the side-wires and all of the AC power is equally distributed between the σ^+ and σ^- fields as the RF magnetic field is perpendicular to the quantization axis. The magnetic dipole interaction Hamiltonian is:

$$\begin{aligned} \hat{H} &= \hat{H}_{\text{Zeeman}} + \hat{H}_{\text{rad}}, \\ \hat{H}_{\text{Zeeman}} &= A_{\text{hfs}} \hat{I} \cdot \hat{J}, \\ \hat{H}_{\text{rad}} &= -\hat{\mu} \cdot \mathbf{B}_{\text{rad}} \cos \omega_{\text{rad}} t, \end{aligned} \tag{3.25}$$

where the time-independent part of the Hamiltonian $\hat{H}_{\text{Zeeman}}$ describing the hyperfine interaction and Zeeman splitting leads to the Breit-Rabi formula (Eq. 3.19) and the part responsible for coupling with the RF or MW radiation $\hat{H}_{\text{rad}}$ leads to the off-diagonal matrix elements of the Hamiltonian in the $|F, m_F\rangle$ basis:

$$\langle F, m_F \pm 1 | \hat{H}_{\text{rad}} | F, m_F \rangle = \frac{\hbar \Omega_0}{2} \sqrt{F(F+1) - m_F(m_F \pm 1)}. \tag{3.26}$$

For MW $\sigma^{\pm}$ transitions [64]:

$$\langle F', m_F \pm 1 | \hat{H}_{\text{rad}} | F, m_F \rangle = \pm \frac{\hbar \Omega_0}{2} \sqrt{(I \pm m_F + 1)^2 - \frac{1}{4}}, \tag{3.27}$$

and for MW π transitions:

$$\langle F', m_F \pm 1 | \hat{H}_{\text{rad}} | F, m_F \rangle = \frac{\hbar \Omega_0}{2} \sqrt{(2I+1)^2 - 4m_F^2}. \tag{3.28}$$

We will use these results to find the RF and MW field coupling strengths experimentally.

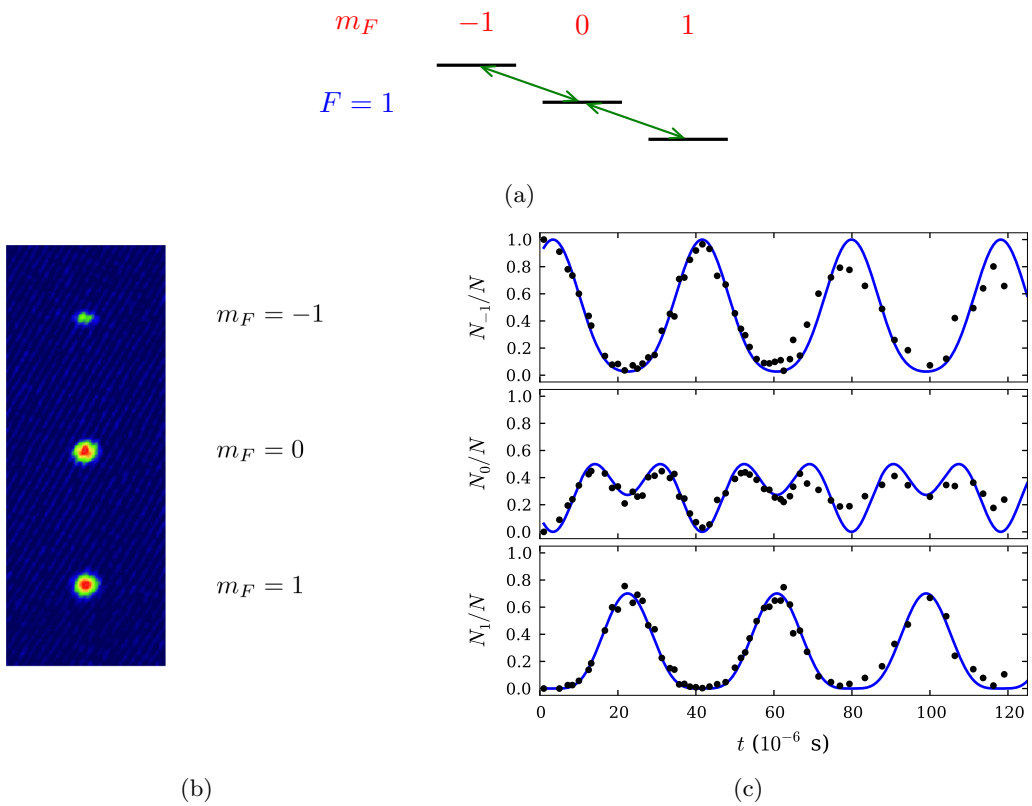

Figure 3.10: RF Rabi oscillations in an $F = 1$ trapped BEC

(a) Level diagram for the $F = 1$ hyperfine state in ^{87}Rb. A RF field is applied which is almost resonant with all single-photon transitions between the Zeeman sublevels.

(b) Images of the BEC in states $m_F = -1$, 0 and 1 after the separation. All three images are taken simultaneously.

(c) Temporal dependence of the population of each Zeeman sublevel relative to the total number of atoms N. The RF coupling is applied during a variable time t. Black points represent the experimental data and blue lines represent the theoretical dependencies (Eq. 3.32) which fit the data.

In order to measure the RF coupling strength we apply a quasi-resonant electromagnetic field to the ^{87}Rb atoms, initially condensed in the $|F = 1, m_F = -1\rangle$ state. The radiation frequency was set to 2.26 MHz and the output of the SRS DS345 generator to -13 dBm. The magnetic field of the trap bottom was adjusted to 3.23 G. Three Zeeman states will be coupled by the RF field (Fig. 3.10a) leading to Rabi oscillations in a three-level system. The RF radiation is applied to the trapped condensed atoms during a finite time t. The atoms are then held in the trap for $t_{\rm hold} = 0.3$ ms. Atoms with $m_F = -1$ remain trapped in such a position that the magnetic field gradient $dB/dy = 2mg/\mu_B$ holds the atoms in the presence of gravity. At the same time atoms with $m_F = 0$ fall down from the trap with acceleration $\vec{g}$ as they are not sensitive to the magnetic field to a first-order approximation. Atoms with $m_F = +1$, which are in a high-field seeking state, are accelerated downwards by the magnetic field gradient dB/dy and $\vec{g}$ with acceleration of $2\vec{g}$. Therefore, the components $m_F = -1$, 0 and 1 obtain initial velocities of 0, $gt_{\rm hold}$ and $2gt_{\rm hold}$, respectively, and are spatially separated after a free expansion time (20 ms). We image all the components simultaneously in free fall after transferring them to the $F = 2$ state with a short 0.1 ms pulse of repump laser light (Fig. 3.10b).

For the $F = 1$ state both of the off-diagonal matrix elements of the Hamiltonian $\hat{H}_{\rm rad}$ responsible for magnetic dipole coupling are equal to $\hbar\Omega_0/\sqrt{2}$. Following the derivation in the thesis of R. P. Anderson [64] wavefunctions in each state are expressed by

$$\psi_{m_F} = \frac{(2F)!}{(F+m_F)!(F-m_F)!} c_1^{F+m_F} c_2^{F-m_F}, \tag{3.29}$$

where the squares of the state amplitudes $c_{1,2}$ are:

$$|c_1|^2 = \frac{\Delta^2}{\Omega_0^2} + \frac{\Omega_0^2}{\Omega_0^2+\Delta^2} \cos^2\left(\frac{\sqrt{\Omega_0^2+\Delta^2}}{2} t\right), \tag{3.30}$$

$$|c_2|^2 = \frac{\Omega_0^2}{\Omega_0^2+\Delta^2} \sin^2\left(\frac{\sqrt{\Omega_0^2+\Delta^2}}{2} t\right), \tag{3.31}$$

where Ω_0 is the coupling strength and $|c_1|^2 + |c_2|^2 = 1$. We obtain the relative populations

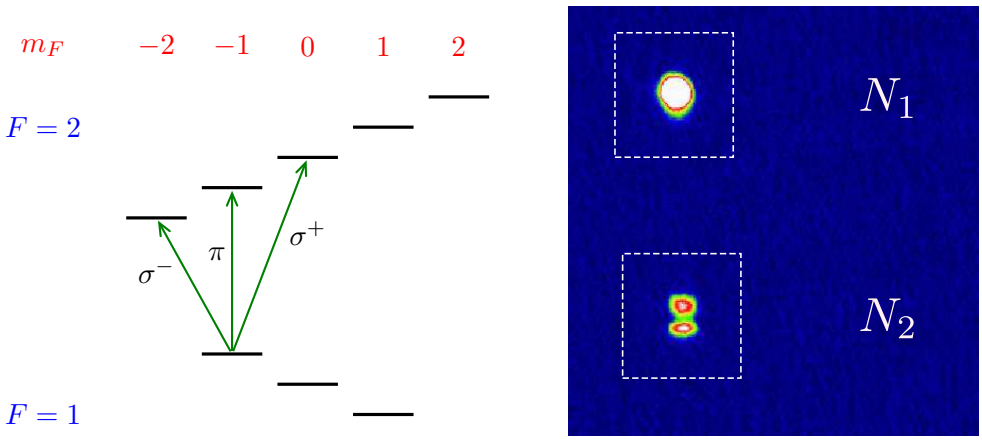

(a) (b)

Figure 3.11: Scheme for performing single-photon MW spectroscopy. Radiation resonant with one of the MW transitions (σ^+, π or σ^-) is applied during 0.1 ms (a). Outcoupled atoms in state $F = 2$ are accelerated during a 0.3 ms hold time and separated from the state $|1\rangle$ atoms in free fall (b). N_2 and N_1 are the corresponding atom numbers.

N_i/N of all the Zeeman sublevels in the $F = 1$ state

$$\begin{aligned} N_{-1}/N &= |\psi_{-1}|^2 = \left(1 - |c_2|^2\right)^2, \\ N_0/N &= |\psi_0|^2 = 2\,|c_2|^2\left(1 - |c_2|^2\right), \\ N_1/N &= |\psi_1|^2 = |c_2|^4. \end{aligned} \tag{3.32}$$

The best fitting of the analytical formulae (3.32) to the data obtained for different coupling times t (Fig. 3.10c) yields $\Omega_0/2\pi = 23.9(2)$ kHz and $\Delta/2\pi = 10.5(3)$ kHz. As long as atoms are held in the magnetic field gradient, the atoms are coupled to the RF field at different values of the static magnetic field and, hence, different Zeeman splittings at different y positions in the cloud. In the case of a BEC with 10^5 atoms, the Zeeman splittings at the top of the cloud and at the bottom of the cloud differ by 18 kHz. This leads to a dephasing of the Rabi oscillations for times longer than 80 µs (Fig. 3.10c).

In order to characterize the MW radiation and measure the magnitude of the magnetic field in the trapping potential minimum, we perform single-photon microwave spectroscopy. We excite $\sigma^\pm$ and π transitions for the condensed atoms trapped in the

$|F = 1, m_F = -1\rangle$ state (Fig. 3.11a). We choose a short (100 μs) MW pulse duration which is close to a half Rabi oscillation. The MW pulse is applied at $t_{\text{hold}} = 0.3$ ms before the trapping potential is switched off and outcouples atoms to one of the non-trappable magnetic sublevels ($F = 2$, $m_F = -2, -1, 0$) which are ejected from the trap. While the condensate in the $|F = 1, m_F = 1\rangle$ state is held during t_{hold}, atoms in the $F = 2$ level with $m_F = 0, -1, -2$ are pushed downwards with accelerations $\vec{g}$, $2\vec{g}$ and $3\vec{g}$, respectively, due to the presence of magnetic field gradient $dB/dy = 2mg/\mu_B$ in the trapping potential minimum. After free fall, components with different magnetic moments, and, hence, different initial velocities, are separated, and atoms with $F = 1$ are transfered to $F = 2$ by a 0.1 ms pulse of repump laser light and both states are imaged simultaneously (Fig. 3.11b). We tune the MW frequency and measure the relative populations of the outcoupled components (Fig. 3.11). In our experiments, it is necessary to tune the trap so that the average magnetic field at the trapping potential minimum is $B_0' = 3.229$ G; at this value of the magnetic field the three MW transitions are separated by 2.26 MHz. When the atomic cloud is placed in a magnetic trap under gravity, the trap minimum does not coincide with the minimum of the magnetic field and the atoms are affected by the magnetic field gradient dB/dy. The resonance transition frequency becomes different for different vertical slices of the cloud (18 kHz difference between the top and the bottom of a BEC with 10^5 atoms) which explains the shapes of outcoupled component and dephasing of the MW Rabi oscillations (similarly to [32], Fig. 3). Fitting the data with Lorentzians (Fig. 3.12), we find the transition frequencies for σ^+ and π resonances $f_+ = 6.83241834(18)$ GHz and $f_\pi = 6.8301550(7)$ GHz, respectively. The measured resonance widths $\Gamma_+ = 8.8 \pm 0.3$ kHz and $\Gamma_\pi = 18.5 \pm 1.1$ kHz are defined by the varying magnetic field across the atomic cloud and power broadening (Fig. 3.12). The width of the recorded resonance depends on the magnetic field gradient of the cloud and is larger for transitions which couple the atoms with a larger difference in magnetic moment. Using the Breit-Rabi formula we measure a magnetic field of $B_0 = 3.2312(4)$ G at the trap centre.

In order to characterize the MW power we couple the two hyperfine levels with a MW

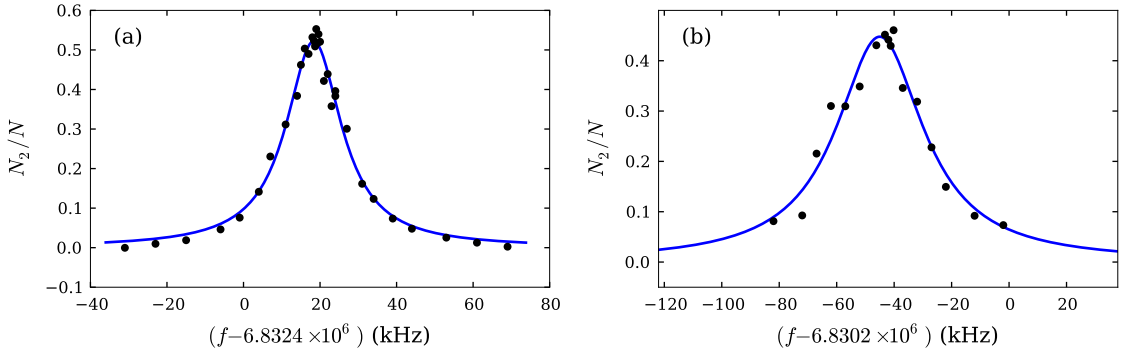

Figure 3.12: Single-photon MW resonances. The population of the outcoupled state N_2 is measured relative to the total number of atoms N in the BEC.
(a) σ^+ resonance, transition $|F=1, m_F=-1\rangle \rightarrow |F=2, m_F=0\rangle$,
(b) π resonance, transition $|F=1, m_F=-1\rangle \rightarrow |F=2, m_F=-1\rangle$.

field and record Rabi oscillations of the two-level system. We measure the population N_2 of the upper state with $F=2$, $m_F=-1$ or 0 simultaneously with the population N_1 of the trapped component $|F=1, m_F=-1\rangle$. The relative difference of both populations oscillates at the single-photon Rabi frequency. An extra decoherence of the Rabi oscillations is present because a differential Zeeman shift of the state $|F=1, m_F=-1\rangle$ and the non-trappable Zeeman sublevels of $F=2$ state varies across the cloud. We account for this effect by adding an additional exponential decay to the Rabi oscillations and fit the oscillations with the function

$$\frac{N_2}{N} = A\, e^{-t/\tau}\, \cos(\Omega t + \varphi_0) + B, \tag{3.33}$$

where the amplitude A, shift B, Rabi frequency Ω, initial phase φ_0 and decay time τ are kept as free parameters. Finally, we find Rabi frequencies for the σ^-, π and σ^+ transitions: $\Omega_- = 2\pi\times15.23(6)$ kHz, $\Omega_\pi = 2\pi\times11.01(8)$ kHz and $\Omega_+ = 2\pi\times7.23(5)$ kHz. The measured Rabi frequencies determine the power broadening contributions to the measured widths of the resonances Γ_π and Γ_+.

In order to produce a coherent superposition of states $|F=1, m_F=-1\rangle$ and $|F=2, m_F=1\rangle$ we couple them with the MW and RF radiation exciting a two-photon

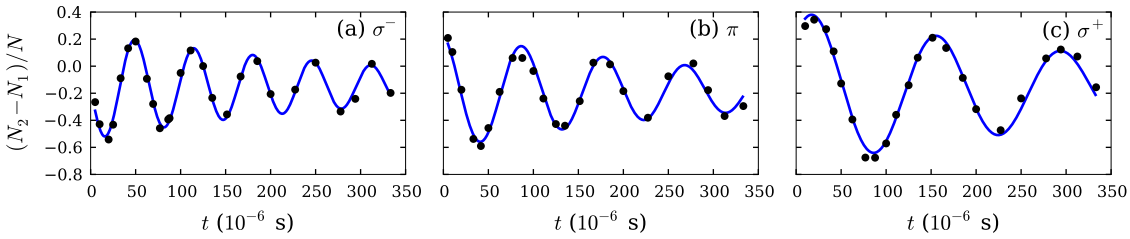

Figure 3.13: Measurement of σ^-, π an σ^+ MW Rabi frequencies Ω. The relative population difference is fitted with a decaying sinusoid with decay time τ.
(a) σ^- transition: $\Omega_- = 2\pi \times 15.23(6)$ kHz, $\tau_- = 330(45)$ ms,
(b) σ^π transition: $\Omega_\pi = 2\pi \times 11.01(8)$ kHz, $\tau_\pi = 327(56)$ ms,
(c) σ^+ transition: $\Omega_+ = 2\pi \times 7.23(5)$ kHz, $\tau_+ = 420(54)$ ms.

transition (Fig. 3.14a). The detuning between the intermediate level (grey dashed line in Fig. 3.14a) and the $|F = 2, m_F = 1\rangle$ state was chosen to be $\Delta = 2\pi \times 988$ kHz. According to [64], the two-photon Rabi frequency is $\Omega_2 = \sqrt{3}\Omega_{0,\mathrm{MW}}\Omega_{0,\mathrm{RF}}/\Delta$. From Eq. 3.27 we find the MW field strength $\Omega_{0,\mathrm{MW}} = \sqrt{2}\Omega_+$. Using this, we find that the two-photon Rabi frequency is $\Omega_2 = 2\pi \times 428$ Hz. This is close to what we measure under slightly different conditions: $\Omega_2 = 520.8(6)$ Hz (Fig. 3.14b).

3.3 Imaging system

In this section, the implementation of the lens system and laser system for absorption imaging of atoms is described. The optical resolution is measured outside the vacuum chamber. The short-term and long-term linewidth of the imaging laser is characterized. Its effect on the absorption imaging is calculated.

3.3.1 Optical resolution

We use a lens system (Fig. 3.15) constructed of two back-to-back achromats with $F_1 = 150$ mm, $F_2 = 500$ mm and diameter 50 mm (Thorlabs AC508-150-B and AC508-500-B). The lens pair is positioned in such way that the atomic cloud is located at the focal point

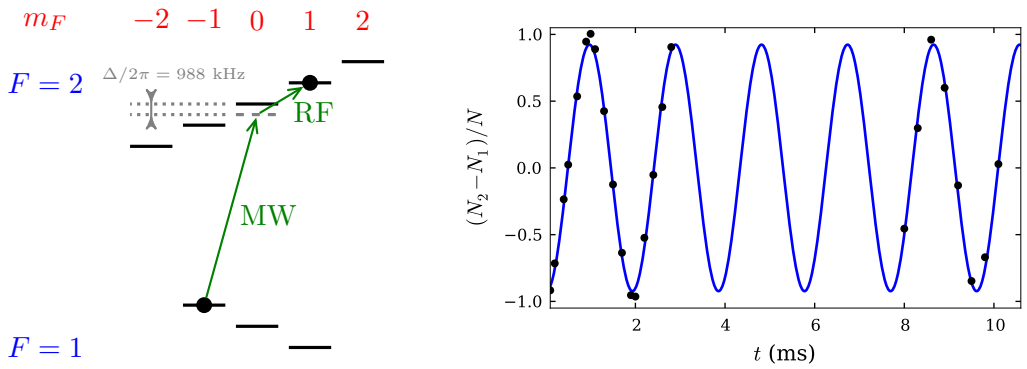

(a) Level diagram (b)

Figure 3.14: Two-photon Rabi oscillations. MW+RF coupling is applied during a variable time t. The detuning from the intermediate level $|F = 2, m_F = 0\rangle$ is $2\pi \times 988$ kHz, and the two-photon detuning is kept close to 0 (a). The relative atom number difference is fitted with a sinusoid, with the Rabi frequency Ω_2 kept as a free parameter (b). The amplitude is equal to 1 as the coupling is resonant. There is no dephasing as the states $|F = 1, m_F = -1\rangle$ and $|F = 2, m_F = 1\rangle$ have the same resonance frequency in different parts of the cloud.

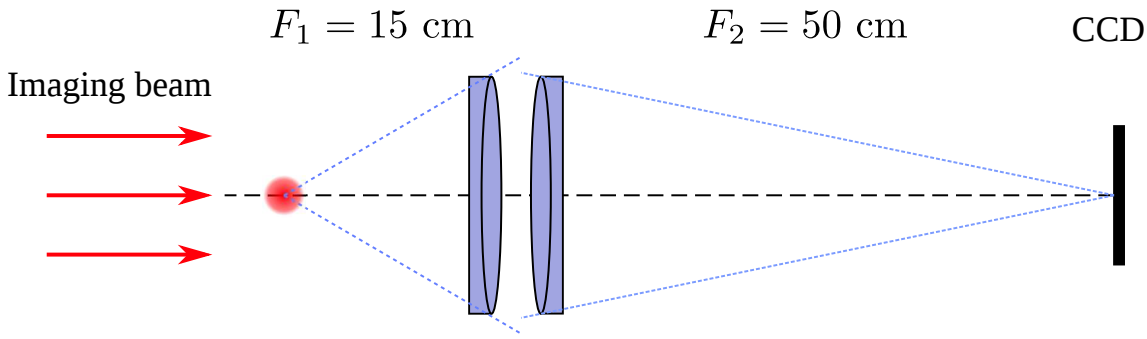

Figure 3.15: The imaging system consists of two back-to-back achromat lenses with focal lengths F_1 and F_2. The atomic cloud is placed at the focal point of the first lens and illuminated by collimated light resonant with the cyclic transition $F = 2 \rightarrow F' = 3$ in ^{87}Rb. The second lens creates a sharp image of the shadow of the cloud on a CCD chip.

of the $F_1 = 15$ cm lens. The CCD chip (Princeton Instruments PI-MAX 1024) is at the focal point of the other achromat lens. An image of the cloud is recorded on the chip of the CCD camera with a theoretical magnification $M = F_2/F_1 = 3.3$. In reality, imperfections in the positioning of the first lens yield a magnification of $M = 4$ measured by dropping the cloud in the presence of gravity and taking into account the pixel size of the CCD chip (13 µm).

The optical resolution of the imaging system in the ideal case is determined by the numerical aperture F_1/D where D is the lens diameter. The resolution by the Rayleigh criterion is $\sigma_{\text{ideal}} = 1.22\,\lambda F_1/D$. In our case, the diffraction limit for that is $\sigma_{\text{ideal}} = 3$ µm. It is important to point out that the resolution depends on the diameter of the lens rather than that of the imaging beam. In reality the resolution is worse than σ_{ideal} because not all of the light from the atomic cloud can pass through the imaging lens. Some of the probing light is shadowed by the atom chip since the atomic cloud is close to the chip. Therefore, we determine the actual optical resolution experimentally, outside the vacuum chamber.

We have measured the resolution by imaging a transmission grating with a 10 µm period (Fig. 3.16a). There are 10 µm and 100 µm steps. For the 100 µm steps we have

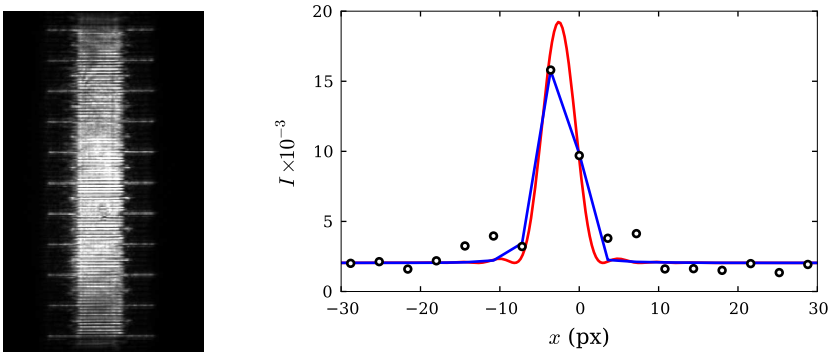

(a) (b)

Figure 3.16: Measurements of the optical resolution of the imaging system. We image a transmission grating with a 10 µm period (a). The resultant distribution of intensities imaged on the CCD chip is fitted with a pixelized Airy function (b). The black dots show the experimental data for the intensities; the red line is the original Airy function; and the blue line is a pixelized version of the Airy pattern.

calculated the pixelized Airy pattern and fit it to the real data, keeping the imaging resolution, the pattern shift and the intensity as free parameters (Fig. 3.16b). The resolution obtained from these measurements was $\sigma_r \approx 6$ µm by the Rayleigh criterion. This can be converted to the resolution given by a Gaussian fit: when one fits an Airy function with a Gaussian, the width of the Gaussian is expressed in terms of the Rayleigh criterion resolution as $2\sigma = 0.68\,\sigma_r$. In a real experimental setup the conditions are slightly different from the measurement carried out outside of the UHV chamber, so the resolution is slightly worse than σ_r.

It is convenient to measure the effective pixel size in the experiment which is equal to the ratio of the CCD camera pixel size divided by the magnification. It is measured by dropping a cloud in the presence of gravity and fitting its position with a parabolic dependence (described in theses [78, 64]).

3.3.2 Absorption imaging

When off-resonant light passes through an atomic medium, the scattering cross-section can be expressed as [85]:

$$\sigma = \frac{\sigma_0}{1 + I/I_s + 4(\Delta/\Gamma)^2}, \tag{3.34}$$

where σ_0 is the resonant cross section. For on-resonant absorption in a two-level system $\sigma_0 = 3\lambda^2/2\pi$ and for ^{87}Rb $\sigma_0 = 2.9 \times 10^{-13}$ m^2. The saturation intensity I_s depends on the polarization of the light. For pure σ^+ transitions in ^{87}Rb $I_s = 1.67$ mW/cm^2. However for linearly polarized imaging light when the population is equally distributed among all the magnetic sublevels $I_s = 3.58$ mW/cm^2 [85]. Imperfections in the polarization may cause the necessity for absolute atom number calibration.

In absorption imaging, we collect three consecutive frames: clean-frame, absorption frame and background frame. The clean frame discharges the CCD chip from the accumulated dark current. The second frame is taken with the absorbing atoms present. The third frame is collected in the presence of the same imaging light but without atoms. Optionally, the "dark" intensity in the absence of any light can be measured and subtracted from all the collected images. In the resonant case ($\Delta = 0$) the column density of the atomic cloud can be calculated as [46]:

$$n(x, y) = \frac{1}{\sigma_0}\left[-\ln\left(\frac{I_{\text{abs}}}{I_{\text{bg}}}\right) + \frac{I_{\text{bg}} - I_{\text{abs}}}{I_{\text{sat}}}\right], \tag{3.35}$$

where I_{abs} is the intensity taken from the absorption frame, I_{bg} is taken from the background frame and I_{sat} is the saturation intensity I_s expressed in terms of pixel counts. At small optical cloud densities the column density becomes close to

$$n(x, y) = -\frac{1}{\sigma}\ln\left(\frac{I_{\text{abs}}}{I_{\text{bg}}}\right). \tag{3.36}$$

We measure the saturation intensity I_{sat} using Eq. 3.35. From this equation we obtain:

$$\sum I_{\text{bg}}\left(1 - e^{-\sigma_0 n_0}\right) = I_{\text{sat}} N - I_{\text{sat}} \sum n_0, \tag{3.37}$$

where $n_0 = -\sigma_0^{-1}\ln(I_{\text{abs}}/I_{\text{bg}})$ and the summation is performed using all the points of the frame. By varying the imaging laser intensity I_{bg}, different points on the linear dependence

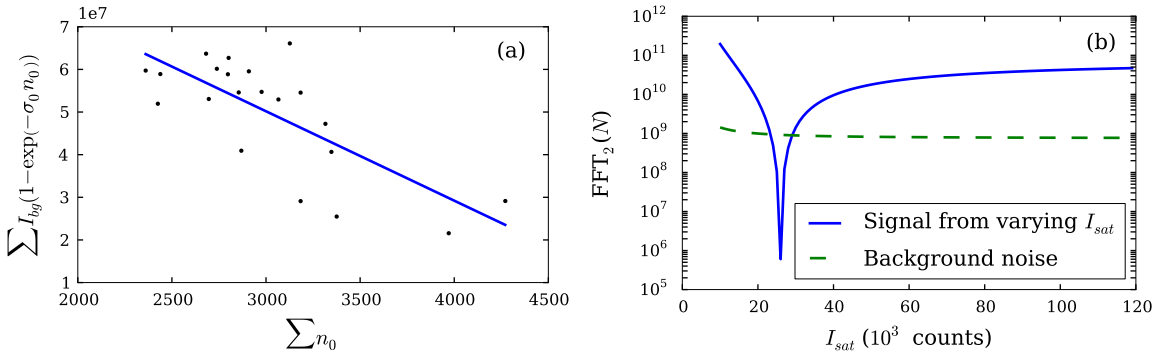

Figure 3.17: Calibration of I_{sat} on the CCD image using two different methods.
(a) The first method involves collecting many images with the same atom number N and different I_{bg} and fitting the data with a linear dependence with slope equal to I_{sat}.
(b) The second method involves collecting many pairs of images with high and low I_{bg} and minimizing variations in the imaged atom number N by minimizing the second component in a discrete Fourier transform by adjusting I_{sat}.

are obtained, the slope of which is equal to the saturation intensity I_{sat} expressed in terms of CCD camera counts. Since the technique assumes that the total number of atoms N is the same in all frames, it should be kept constant during the measurement, and the variations of the prepared number of atoms N determine the uncertainty of measured I_{sat}. For our data we obtain $I_{\mathrm{sat}} = 21(4) \times 10^3$ counts for the effective pixel size of 3.25 µm.

It is not easy to keep the atom number N constant in the frames. Post-selection from a large number of frames could not be used as the measured N depends on the real number of atoms and the imaging laser intensity which is varied. We developed another method for calibrating I_{sat}. The idea is based on the fact that the total number of atoms obtained with Eq. 3.35 should not depend on the background counts I_{bg}. We periodically vary I_{bg}, so that it is high in odd realizations and low in even realizations if they are enumerated from the beginning of the set of measurements. Then we calculate the component in a fast (discrete) Fourier transform of the sequence of atom numbers N corresponding to the frame period of 2 and plot it against the variable I_{sat} (solid line in Fig. 3.17b). The minimum of the plot means that the atom number N does not depend on periodic I_{bg}

variations. The uncertainty is calculated as a region where the second Fourier component is less than the average of the other components indicated by the dashed line in Fig. 3.17b. In this measurement we find $I_{\mathrm{sat}} = 26(3) \times 10^3$ for the effective pixel size of 3.46 μm. The method is stable against slow variations in N.

3.3.3 Imaging laser linewidth

For high precision measurements in BEC interferometry, it is important to measure the total number of atoms with low noise. Therefore, for imaging of a BEC we use a dedicated laser.

A Toptica DL100 laser with MogLabs electronics is locked to the $F = 2 \rightarrow F' = 3$ transition in ^{87}Rb using a polarization spectroscopy scheme (Fig. 3.18). The detuning of the imaging beam can be varied by a double-pass AOM and the beam is coupled to a polarization preserving optical fibre which delivers imaging light to the UHV chamber.

We measure the combined linewidth of two independent lasers locked to different ^{87}Rb resonances with MogLabs controllers. The beams from the two lasers are applied to a fast photodiode (New Focus 1621) and the output signal is processed by a RF spectrum analyzer (R&S FSP7) (Fig. 3.19). The beatnote signal is fitted with a Gaussian function for which the full width half maximum (FWHM) is expected to be larger than that of a single laser by factor of $\sqrt{2}$ assuming both lasers have the same linewidth. When the averaging time of the spectrum analyzer is 0.5 s, we obtain a laser FWHM linewidth of 0.32 MHz (Fig. 3.19a). However, when the averaging time is 2.5 s, the FWHM linewidth increases to 1.3 MHz (Fig. 3.19b). By comparison, the long-term linewidth of a Toptica DL100 laser locked with the original Toptica controller is about 2 MHz. The FWHM linewidth can be expressed as $2\sigma_l\sqrt{2\ln 2}$, where σ_l^2 is the variance of the Gaussian function representing the spectrum of a single laser. For our experiments, the long-term laser linewidth is important since this contributes shot-to-shot variations to the measured atom number.

Now we determine how fluctuations in the imaging laser affect the uncertainty in the total number of atoms. The measured number of atoms N_Δ is proportional to the number

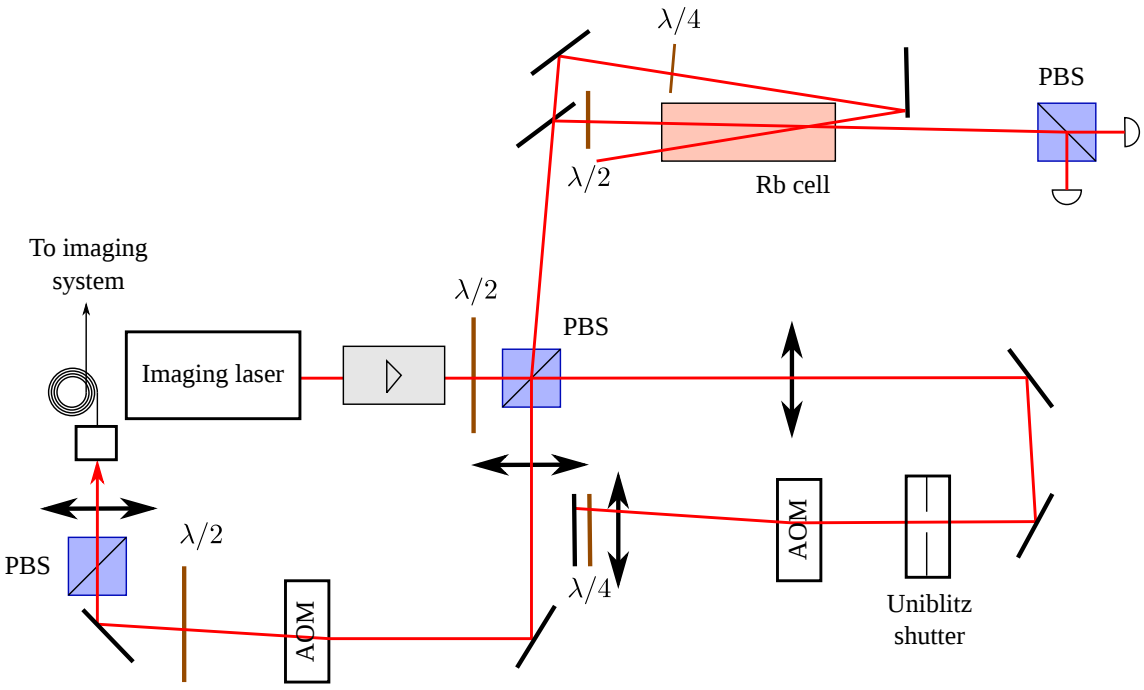

Figure 3.18: Imaging laser system. A small part of the laser beam is split on the polarization beamsplitter (PBS) to the polarization spectroscopy locking system. The main beam passes through a double-pass AOM (IntraAction ATM-801A2) which is used to shift the frequency by an adjustable amount $\sim +120$ MHz and to tune the imaging laser into resonance with the $F = 2 \rightarrow F' = 3$ transition. The frequency of the light is shifted back by -120 MHz with a second, single-pass AOM. Both AOMs are used to quickly switch the laser beam on and off together with a Uniblitz shutter. Finally, the light is coupled into an optical fibre producing an outcoupled power ~ 1.5 mW.

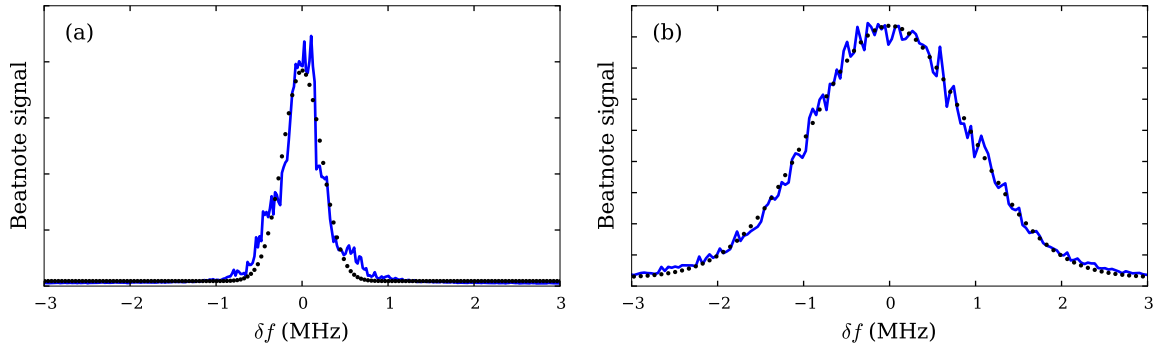

Figure 3.19: Laser linewidth measurement. The beatnote signal is fitted with a Gaussian (dotted line). Signals with 0.5 s (a) and 2.5 s (b) averaging times are presented. The corresponding linewidths are 0.32 MHz and 1.3 MHz.

of atoms measured exactly on resonance N_0 and to the Lorentzian line shape of an atom. From Eq. 3.34 their ratio is

$$\eta(\Delta) = \frac{N_\Delta}{N_0} = \frac{1}{1 + 4\left(\frac{\Delta}{\Gamma}\right)\left(1 + \frac{I}{I_s}\right)^{-1}}, \tag{3.38}$$

or, expanding in a Taylor series

$$\eta(\Delta) = 1 - \frac{4}{1 + \frac{I}{I_s}}\left(\frac{\Delta}{\Gamma}\right)^2 + \frac{16}{\left(1 + \frac{I}{I_s}\right)^2}\left(\frac{\Delta}{\Gamma}\right)^4 + O\left(\left(\frac{\Delta}{\Gamma}\right)^6\right), \tag{3.39}$$

where I is the intensity of the laser, I_s is the saturation intensity of the atomic system, $\Gamma/2\pi = 5.9$ MHz is the natural linewidth for ^{87}Rb and Δ is the detuning of the radiation from the resonance. The laser line spectrum usually has a Gaussian shape, and the probablity density distribution of the laser frequency having the detuning Δ is

$$\rho_l(\Delta) = \frac{1}{\sqrt{2\pi\sigma_l^2}} e^{-\frac{\Delta^2}{2\sigma_l^2}}, \tag{3.40}$$

where the FWHM linewidth of the laser is $2\sqrt{2\ln 2}\sigma_l$. Following these considerations, the number of atoms N measured with a resonant laser beam of finite linewidth is related to the real number of atoms N_0 by

$$\frac{N}{N_0} = \int_{-\infty}^{+\infty} \eta(\Delta)\,\rho_l(\Delta)\,d\Delta \tag{3.41}$$

and

$$\left\langle \left(\frac{dN}{N_0} \right) \right\rangle^2 = \int_{-\infty}^{+\infty} \eta(\Delta)^2 \, \rho_l(\Delta) \, d\Delta - \left(\int_{-\infty}^{+\infty} \eta(\Delta) \, \rho_l(\Delta) \, d\Delta \right)^2 . \tag{3.42}$$

The relative uncertainty in the measured atom number can be expressed as a Taylor expansion by:

$$\frac{\delta N}{N} = \frac{4\sqrt{2}}{1 + \frac{I}{I_s}} \left(\frac{\sigma_l}{\Gamma} \right)^2 + \frac{80\sqrt{2}}{\left(1 + \frac{I}{I_s} \right)^2} \left(\frac{\sigma_l}{\Gamma} \right)^4 + O\left(\left(\frac{\sigma_l}{\Gamma} \right)^6 \right) . \tag{3.43}$$

For the 1.3 MHz FWHM laser and intensity $I \approx I_s$, we obtain $\delta N/N = 0.023$. Equation 3.43 suggests that in the limit $\sigma_l \ll \Gamma$ the atom number uncertainty δN scales quadratically with the linewidth of the laser.

3.3.4 Dual-state imaging

We image the two BEC components ($|1\rangle \equiv |F = 1, m_F = -1\rangle$ and $|2\rangle \equiv |F = 2, m_F = 1\rangle$) simultaneously in one realisation of an experimental cycle [22]. The two states have almost the same magnetic moment $\mu_B/2$, and therefore we cannot use the Stern-Gerlach technique to spatially separate them. In order to measure the densities of both states simultaneously, we use the adiabatic rapid passage technique which was first applied to BECs by Russell Anderson [22, 64]. This technique preserves spatial information of both BEC components. Firstly, we release the atoms initially held in the magnetic trap at the magnetic field of 3.23 G (Fig. 3.20). After 2 ms of fall we switch on a MW field having the same frequency as used for the two-photon transition (6.831430037 GHz) for about 2 ms. The uniform magnetic field B_x is ramped down during that time and the MW frequency of the transition $|1\rangle \rightarrow |F = 2, m_F = -1\rangle$ increases. The corresponding detuning of the MW field changes from $\sim +100$ kHz to ~ -100 kHz, and almost all atoms are transferred to the state $|F = 2, m_F = -1\rangle$ (Fig. 3.20). After the passage we apply a magnetic field gradient produced by a 0.2 ms current pulse through the Z-wire so that the clouds in states $|F = 2, m_F = -1\rangle$ and $|2\rangle$ are spatially separated in 16 ms free fall.

The adiabatic passage should be performed on a time scale much longer than the inverse single-photon Rabi frequency. If we increase the duration for turning on the MW field in

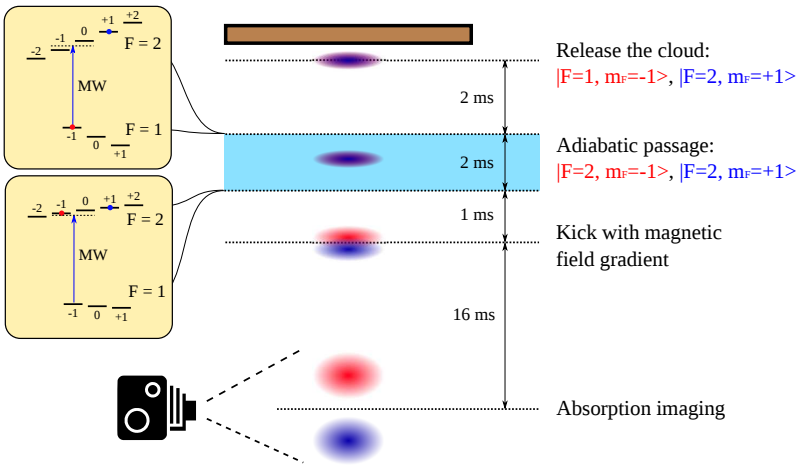

Figure 3.20: Scheme of adiabatic passage. The magnetic field is ramped in such way that the detuning of the MW radiation changes from a positive to a negative value during the adiabatic passage. All the population of state $|1\rangle$ is therefore transferred to state $|F = 2, m_F = -1\rangle$. Both components are imaged in a single image after the Stern-Gerlach separation by a magnetic field gradient and 16 ms of free expansion.

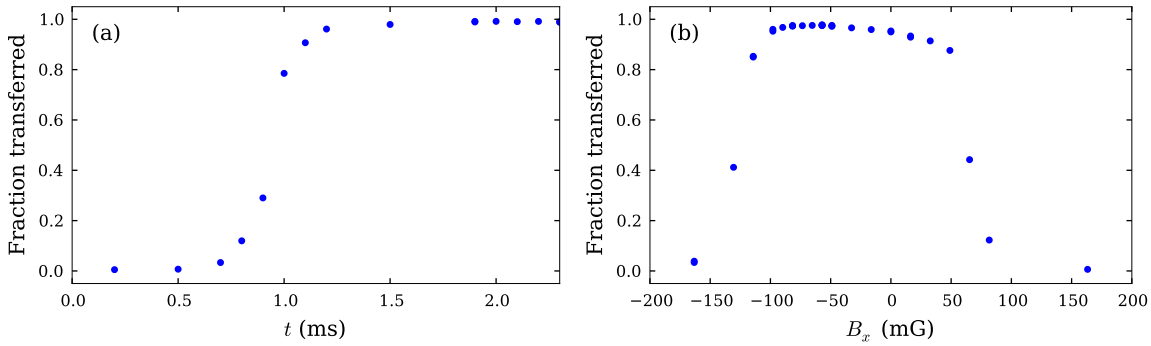

Figure 3.21: Fraction of atoms transferred from the state $|1\rangle \equiv |F = 1, m_F = -1\rangle$ to the state $|F = 2, m_F = -1\rangle$ via adiabatic passage as functions of the duration of the MW field (a) and the static magnetic field B_x (b). The transfer efficiency reaches 99%.

the passage, the transferred population ratio gradually increases to 99% (Fig. 3.21a). It is rather insensitive to the value of the bias magnetic field applied during the passage once the bias field is optimized (Fig. 3.21b). The noise in the transferred number of atoms due to the adiabatic passage efficiency is about 0.2%, which contributes to the uncertainty in the measured number of atoms in state $|1\rangle$.

3.3.5 Fringe-removal algorithm for absorption imaging

We use an "eigenface" fixed pattern noise removal algorithm in which the fringe structure of an absorption frame is reconstructed by projecting the visible fringe structure from the absorption frame on the basis constructed from many background frames. In order to construct the basis we use the Gramm-Schmidt orthogonalization method [65]. Alternatively, LU decomposition might be used for the same purpose [79]. We use masking of the cloud in order to reconstruct the fringe structure.

We define absorption frames as A_i, background frames as B_i, absorption frames in which the atomic cloud is masked (replaced with zeros) as A'_i and background frames with exactly the same mask as B'_i (Fig. 3.22), where $i \in [1, M]$ is an index of a frame doublet (A_i, B_i), M is the number of the frame doublets.

The algorithm concept is the following. All background frames B_i are used to construct an orthonormal basis R_i where $i \in [1, M]$. Any frame B_i can be decomposed into a sum of frames R_j with the corresponding weighing coefficients. In order to construct such a basis, we begin with the normalized B_1 as R_1. Every vector R_{i+1} is calculated by finding and normalizing the component orthogonal to all the frames $R_{1\leq j\leq i}$. After the basis R_j is constructed, we find an optimal background frame as a projection of the absorption frame on the subspace of R_j.

Each frame A and B is composed of $x_{\max} \times y_{\max}$ pixels and can be represented by a matrix $A \equiv (a_{yx})$ or $B \equiv (b_{yx})$. We treat all the frames as $x_{\max} \times y_{\max}$-dimensional vectors $(a_{11}, a_{12}, \ldots, a_{y_{\max}x_{\max}})$. The scalar product of two frames A and B is defined as

$$(A \cdot B) = \sum_{x=1}^{x_{\max}} \sum_{y=1}^{y_{\max}} a_{yx} b_{yx}. \tag{3.44}$$

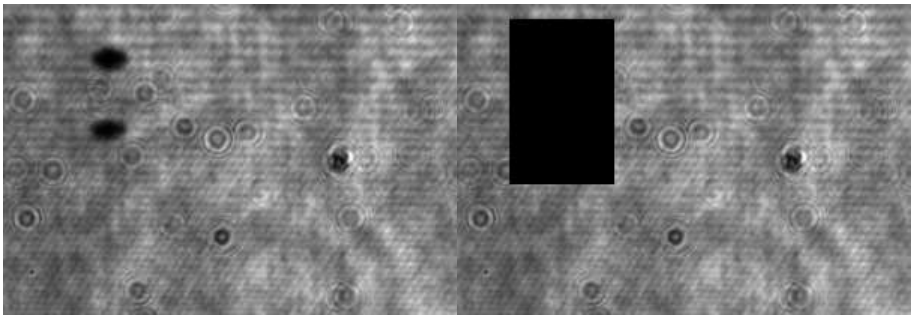

(a) A (b) A'

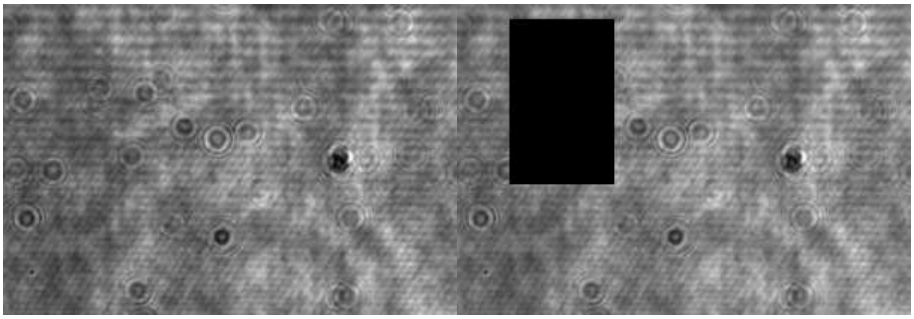

(c) B (d) B'

Figure 3.22: Imaging frames used in the fringe removal algorithm: absorption frame A, masked absorption frame A', background frame B and masked background frame B'.

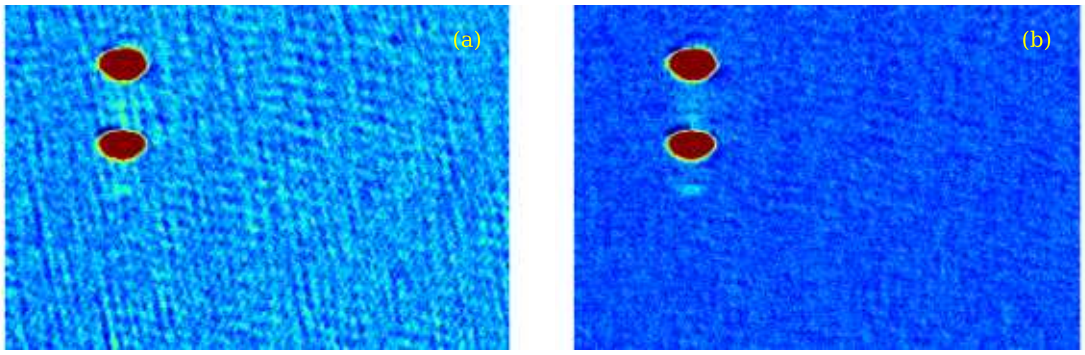

Figure 3.23: Comparison of a usual absorption image (a) with the image processed by the fringe removal algorithm (b) using the same colour scale

The absolute value of a frame A is defined as $|A| \equiv (A \cdot A)^{1/2}$. The orthonormal basis vectors to decompose vectors similar to B'_i are obtained as:

$$\begin{aligned} r'_1 &= \mathrm{norm}\left(B'_1\right), \\ &\dots, \\ r'_i &= \mathrm{norm}\left(B'_i - \sum_{k=1}^{i-1} \left(B'_i \cdot r'_k\right) r'_k\right), \end{aligned} \tag{3.45}$$

where $\mathrm{norm}(x) = x/|x|$. The idea of masking is the following. We construct matrix (α_{ij}) so that

$$\begin{pmatrix} r'_1 \\ \vdots \\ r'_M \end{pmatrix} = \begin{pmatrix} \alpha_{11} & \cdots & \alpha_{1M} \\ \vdots & \ddots & \vdots \\ \alpha_{M1} & \cdots & \alpha_{MM} \end{pmatrix} \begin{pmatrix} B'_1 \\ \vdots \\ B'_M \end{pmatrix} \tag{3.46}$$

The first row of the matrix (α_{ij}) is

$$\alpha_{11} = \frac{1}{|B'_1|}, \qquad \alpha_{12} = \ldots = \alpha_{1M} = 0. \tag{3.47}$$

The other rows, following Eqs. 3.45, are calculated as:

$$\begin{aligned} \alpha_{ij} &= \frac{\beta_{ij}}{\left|\sum_{k=1}^{i} \beta_{ik} B'_k\right|}, \quad \text{where} \\ \beta_{ii} &= 1, \qquad \beta_{i,j<i} = -\sum_{k=1}^{j} \left(B'_i \cdot r'_k\right) \alpha_{kj}, \qquad \beta_{i,j>i} = 0. \end{aligned} \tag{3.48}$$

After calculating the matrix (α_{ij}), a reference frame can be calculated for any image A_i:

$$R_i = \begin{pmatrix} (A_i \cdot r'_1) \\ \vdots \\ (A_i \cdot r'_M) \end{pmatrix} \cdot (\alpha_{ij}) \begin{pmatrix} B_1 \\ \vdots \\ B_M \end{pmatrix}. \tag{3.49}$$

We use R_j instead of a background frame in Eq. 3.35. The noise in such an image is close to the photon shot noise in the absorption frame (Fig. 3.23). Additionally, in our group Valentin Ivannikov has studied the convergence of the algorithm in detail and found that there is a finite optimal number of frames for the best noise reduction (of the order of the square root of the number of pixels in one frame).

Chapter 4

Absolute atom number calibration techniques

Calibration of the absolute total number of atoms is often needed for experiments with cold atoms and BECs, especially for trapped atom interferometry. In the latter, the collisional shift of the transition frequency depends on atom number which should be known with high precision in order to evaluate the value of the shift. In this section we compare a known technique of the atom number calibration based on the condensation fraction below T_c with a new technique of interferometric atom number calibration which we have developed. The third method of calibration uses the scaling of the projection noise with atom number [48, 47] and requires a large number of measurements (~ 500), sensitive detection of small atom numbers ($\sim 10^3$) and low technical noise in the production of a two-component BEC.

4.1 Atom number calibration with the condensate fraction

In this section we calibrate the total number of atoms using the dependence of the Bose-gas condensation temperature T_c on the total number of atoms N. The method is well described in [49, 50]. We incorporate the finite atom number [87] and mean-field corrections [88] in this treatment.

A Bose gas confined in a harmonic trap at a finite temperature T consists of condensed and non-condensed atoms when its temperature is below the critical temperature T_c of Bose-Einstein condensation. The fraction of BEC in the trapped Bose-gas is [10]

$$\frac{N_0}{N} = 1 - \left(\frac{T}{T_c}\right)^3, \tag{4.1}$$

where N_0 is the number of condensed atoms and N is the total number of atoms in the ensemble. In a harmonically trapped ideal Bose gas the condensation temperature with finite number correction is given by [87]

$$T_c^0 = \frac{\hbar\bar{\omega}}{k_B}\left(\sqrt[3]{\frac{N}{\zeta(3)}} - \frac{\pi^2}{12\,\zeta(3)}\right), \tag{4.2}$$

where T_c^0 is the condensation temperature of the ideal Bose gas, $\bar{\omega} = (\omega_x\omega_y\omega_z)^{1/3}$ is the mean trap frequency and $\zeta(x)$ is the Riemann zeta-function. The condensation temperature of an *interacting* Bose gas is different from Eq. 4.2 and should be corrected by ΔT_c [89]:

$$\frac{\Delta T_c}{T_c^0} = b_1\frac{a}{\lambda_0} + b_2\left(\frac{a}{\lambda_0}\right)^2, \tag{4.3}$$

where $a = 100.40\,a_0$ is the s-wave scattering length and λ_0 the thermal de Brogle wavelength given by

$$\lambda_0 = \frac{h}{\sqrt{2\pi m k_B T_c^0}}. \tag{4.4}$$

The coefficient $b_1 \approx -3.426$ follows from mean-field theory [88]. Beyond the mean-field correction the coefficient $b_2 = 46(5)$ was obtained experimentally by Smith et al. [89]. There is no theoretical consensus on the value of b_2 except that it should be positive [90, 91, 92, 93, 94]; therefore we include b_2 in our error analysis instead of using it in the fitting.

We evaporatively cool ^{87}Rb atoms in state $|F = 1, m_F = -1\rangle$ ($N \sim 5\times10^5$) down to a temperature close to T_c. The trap frequencies of the magnetic trap on the chip which we use are $\omega_x = 2\pi\times101.0(5)$ Hz, $\omega_y = 2\pi\times98.23(5)$ Hz and $\omega_z = 2\pi\times11.507(7)$ Hz. We wait 0.7 s after the evaporation for the cloud to thermally equilibrate before we perform the calibration. After reaching the desired temperature with an appropriate choice of the final

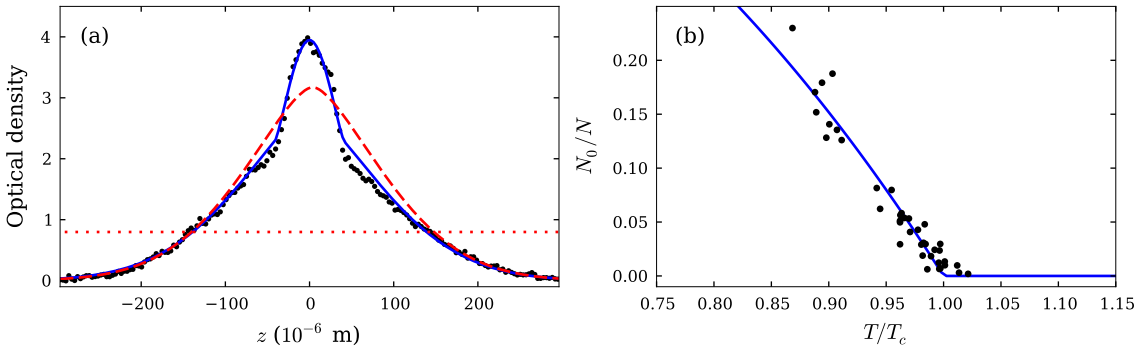

Figure 4.1: (a) Cross-section of the imaged cloud along the axial direction of the trap. We take ~ 50 images of the atomic cloud with the temperature T slightly above and below T_c and fit its 2D column density profile with a bimodal distribution in order to obtain the condensate fraction N_0/N (solid line). The ensemble temperature T is obtained by fitting the wings of the density profile (dashed line fits the data points below the dotted line). (b) Total atom number N is calibrated to make the proper dependence of N_0/N vs T/T_c, where T_c depends on the atom number calibration coefficient; solid line represents the fit of the experimental data with Eq. 4.1.

RF frequency we transfer the cloud to the state $|F = 2, m_F = 1\rangle$ using a MW+RF two-photon π-pulse and take an absorption image using resonant $F = 2 \rightarrow F' = 3$ laser light after a free fall expansion time $t_{\text{drop}} = 20.1$ ms. We employ the "eigenface" fringe-removal algorithm in order to reduce the uncertainty of the measured BEC fraction [79].

In order to evaluate the condensate fraction and the cloud temperature, we perform a 2D fit to the processed absorption image of the cloud with the sum of thermal and BEC profiles. Absorption imaging measures column densities of the cloud. The non-condensed fraction of the column density distribution is [95]

$$n_{\text{th}}(y, z) = \frac{n_{\text{th}}(0)}{g_2(1)}\, g_2\left[e^{-\frac{y^2}{2w_y^2} - \frac{z^2}{2w_z^2}}\right], \tag{4.5}$$

where y and z are radial and axial coordinates, $n_{\text{th}}(0)$ is the peak column density of the distribution, w_y and w_z are Gaussian widths, $g_n(x)$ is a polylogarithm function (for $n = 2$

it is also known as Spence's function which has fast numerical implementation). The ensemble temperature T can be calculated after a time-of-flight expansion:

$$k_B T = \frac{m w_i^2}{\frac{1}{\omega_i^2} + t_{\mathrm{drop}}^2}, \tag{4.6}$$

where the free expansion time $t_{\mathrm{drop}} = 20.1$ ms in our experiments. We restrict ourselves to fitting in the weak (axial) trap direction ($i \equiv z$) as the temperatures obtained from radial fits ($i \equiv y$) for small expansion times differ from Eq. 4.6. The reason for this may be in the high value of the third-order anharmonicity of our trap in the y direction (Tab. 3.1).

The column density of a BEC in Thomas-Fermi approximation obtained in absorption images is [95]

$$n_{\mathrm{BEC}}(y,z) = n_{\mathrm{BEC}}(0) \left(1 - \left(\frac{y}{r_y}\right)^2 - \left(\frac{z}{r_z}\right)^2\right)^{3/2}, \tag{4.7}$$

where r_i are radii of the BEC density distribution and $n_{\mathrm{BEC}}(0)$ is its peak density. In order to obtain the BEC fraction N_0/N, we perform a two-dimensional fit to the atomic cloud density with a bimodal distribution (sum of Eq. 4.7 and Eq. 4.5, Fig. 4.1a). The thermal part of the fit (Eq. 4.5) does not well describe the density distribution in the regions of high density, however it allows to obtain the dependence of the condensate fraction on temperature precisely enough to find the condensation temperature T_c. One needs to use self-consistent Hartree-Fock model [96] instead of Eq. 4.5 in order to obtain a better fitting near the centre of the density distribution. The number of condensed atoms is

$$N_0 = \frac{2\pi}{5} n_{\mathrm{BEC}}(0)\, r_y\, r_z, \tag{4.8}$$

while N is measured by summing up the column densities of the whole cloud. We fit the wings of the 2D density distribution (points with $n < n_{\max}/5$) with Eq. 4.5 to obtain T (Fig. 4.1a). Fitting the regions far from the centre of the ensemble ensures that interactions effects do not affect the shape of the density profile [96, 97]. The effect of interactions is clearly visible in Fig. 4.1a as a difference between the solid and dashed lines near the centre of the cloud, similar to Fig. 1 in [97].

After we obtain a set of points N_0/N vs T, we fit the points N_0/N vs $T/T_c(kN)$ with Eq. 4.1 keeping the calibration coefficient k as a free parameter (Fig. 4.1b). Equation 4.1

was also multiplied by an additional fitting parameter to allow for interaction effects near the condensation threshold. We used the "numpy" Python library for fitting and the "scipy" module for fast calculation of Spence's function $g_2(x)$. When the finite atom number and first-order interaction corrections are included in T_c, we obtain $k = 1.829(15)$. Use of the first-order (mean-field) interaction correction coefficient b_1 in the fit leads to a $+12.6\%$ shift of k; the finite atom number correction shifts k by $+2.7\%$; and the second-order beyond mean-field interaction correction b_2 can shift k by -1.9%. Nevertheless, since the theoretical investigations are not well developed yet and there is no guarantee that b_2 does not depend on T and N, we include the shift due to b_2 in the systematic uncertainty. The uncertainty in the mean trap frequency $\delta\bar{\omega}/\bar{\omega} = 1.7 \times 10^{-3}$ leads to an error in the calibration $\delta k/k = 0.5\%$. Summing up squares of fitting uncertainty and systematics, we have $k = 1.83(4)$, where most of the uncertainty comes from the beyond mean-field shift of the condensation temperature. The precision of the method might also be affected by the trap anharmonicities which are not included but affect the cloud in the regions far from the trap centre. The use of simulated Bose-gas profile instead of the simple bimodal distribution may also affect the precision [96].

4.2 Interferometric atom number calibration

In a two-component BEC the collisional shift of the transition frequency is proportional to the BEC density, or $\propto N^{2/5}$ if the BEC is held in a harmonic trap [21]. In the simplest model, the atom number-dependent phase evolution rate is equal to the collisional shift which allows one to find the ratio k between the real number N and measured number of atoms N_{meas} using a Ramsey interferometric sequence (Fig. 2.1a). Firstly, we analyse the problem analytically using the collisional shift model in order to find what the calibration coefficient k depends on and to find the sources of systematic error. After that we find more precise calibrations using simulations of the coupled GPE equations. We also derive an analytical solution for $\theta \ll \pi/2$ which takes into account kinetic energy terms based on the theory from Sec. 2.4.

As follows from Eq. 2.24, in the approximation of an unchanged condensate density

and a neglected kinetic energy term, the interference fringe of the coherent superposition prepared by a θ-pulse for a fixed evolution time t (Fig. 2.1a), detuning Δ and phase φ_0 of an interrogation $\pi/2$-pulse has the approximate functional form:

$$P_z(N) = A\cos\left(\alpha T\, N^{2/5} + \phi_0\right), \tag{4.9}$$

where the phase $\phi_0 = \Delta T - \frac{\pi}{4} + \varphi_0$ is independent of the total number of atoms, $\alpha \propto \left[a_{22} - a_{11} + \langle\cos\theta\rangle_{eff}\,(2a_{12} - a_{11} - a_{22})\right]$ (Eq. 2.23). The term $\langle\cos\theta\rangle_{eff}$ is the time-averaged splitting $(N_1 - N_2)/(N_1 + N_2)$ just after the preparation radiation pulse. For short evolution times $\langle\cos\theta\rangle_{eff} = \cos\theta$; however at longer evolution times two-body losses change this coefficient. Atoms are lost faster from state $|2\rangle$ than from state $|1\rangle$ in ^{87}Rb; thus N_2 decreases faster than N_1. This means that $\langle\cos\theta\rangle_{eff} > \cos\theta$ and $\langle\cos\theta\rangle_{eff} \to 1$ as $T \to \infty$. Assuming that the actual total number of atoms in the system N is proportional to the measured number of atoms N_{meas} with coefficient k, a fringe takes the form $P_z(N) = A\cos\left(\alpha T k^{2/5}\, N^{2/5} + \phi_0\right)$, and once α is calculated from the scattering properties the calibration coefficient k can be found. We use Eq. 4.9 only for error analysis as we derive more precise analytics for the special case $\theta \ll \pi/2$.

For the case of a $\pi/2$ preparation pulse $\alpha \propto (a_{22} - a_{11})$ for short evolution times t. Thus the calibration coefficient depends mostly on the difference between the intraspecies scattering lengths and the accuracy of this calibration is given by:

$$\frac{\delta k}{k} \approx \frac{5}{2}\frac{\delta\,(a_{11} - a_{22})}{a_{11} - a_{22}} = \frac{5}{2}\frac{\sqrt{\delta a_{11}^2 + \delta a_{22}^2}}{a_{11} - a_{22}}. \tag{4.10}$$

Taking the values and uncertainties of the s-wave scattering lengths $a_{11} = 100.40(10)\,a_0$ [39, 19] and $a_{22} = 95.44(7)\,a_0$, $\delta(a_{11} - a_{12}) = 0.07\,a_0$ (Ch. 6), the systematic error of such a calibration due to uncertainties in a_{jj} is $\delta k/k = 4\%$. However, if the fringe amplitude does not agree with the GPE simulations, the uncertainty can be much more for a short evolution time t. Nonlinearity in absorption imaging can also contribute to a systematic shift of the calibration coefficient. If t is increased, collisional loss terms also affect the dynamics and reduce the measured number of atoms. Apart from that, n_2 decreases faster than n_1, so a_{12} also contributes to the shape of $P_z(N)$.

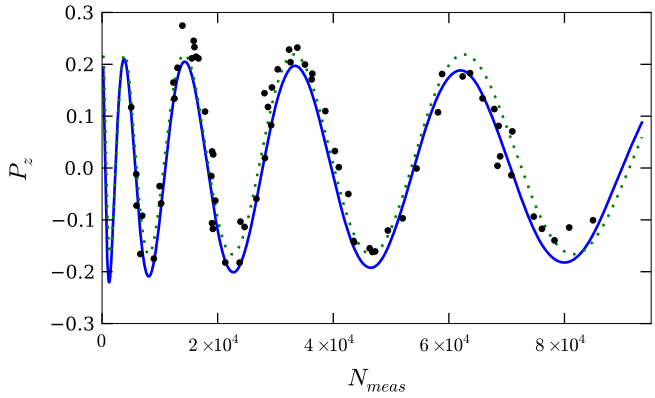

(a) $\theta = \frac{\pi}{10}, k = 1.86(4)$

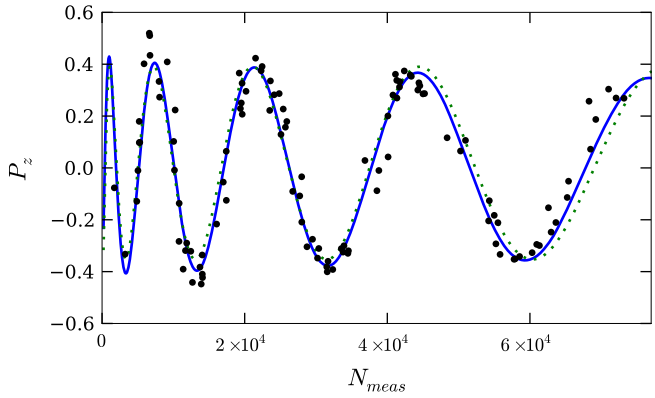

(b) $\theta = \frac{\pi}{5}, k = 1.80(4)$

Figure 4.2: Calibration of the total number of atoms performed with Ramsey interferometry. The normalized longitudinal spin projection $P_z = (N_2 - N_1)/(N_2 + N_1)$ was recorded as a function of the atom number N_{meas} measured by absorption imaging. Black points represent the experimental data, solid lines are the results of GPE simulations ($a_{11} = 100.40\,a_0$, $a_{12} = 98.006(16)\,a_0$, $a_{22} = 98.44\,a_0$) and dotted lines correspond to the analytical dependence given by Eq. 4.16. The calibration is carried out with $\pi/10$ (a) and $\pi/5$ (b) splitting pulses and an evolution time of 0.34 s. The calibration coefficients k measured with different splitting pulses is the same within the systematics. Without taking the systematics into account, the statistical uncertainty in the calibration is just 1%.

When $\theta \ll \pi/2$, long interrogation times t can be used. We select $t = 0.34$ s since this is equal to the time of the mean-field coherence revival (Ch. 5) and provides a high fringe visibility. If the calibration is performed with a $\theta \ll \pi/2$ pulse

$$\alpha \propto 2\,(a_{11} - a_{12}) - \frac{\theta^2}{2}\,(a_{11} + a_{22} - 2a_{12})\,. \tag{4.11}$$

Since $\theta^2/2 \ll 1$, the calibration relies mostly on another difference in scattering lengths, and the contribution of the uncertainty in a_{22} is quite minor

$$\frac{\delta k}{k} \approx \frac{5}{2}\frac{\sqrt{4\left[\delta\,(a_{11} - a_{12})\right]^2 + \frac{\theta^4}{4}\left[\delta\,(a_{11} - a_{12})^2 + (a_{12} - a_{22})^2\right]}}{2\,(a_{11} - a_{12})}. \tag{4.12}$$

We use our precision measurements which give a value for $a_{11} - a_{12}$ with a precision of $0.016\,a_0$ (Ch. 6) in order to use in the interferometric calibration at $\theta \ll \pi/2$. With the precision of our measurements, the contribution of uncertainties in the scattering lengths is $\delta k/k = 1.7\%$ for $\theta = \pi/10$ and $\delta k/k = 1.8\%$ for $\theta = \pi/5$. Another advantage of this scheme is that N_1 stays almost unchanged during the BEC evolution since the two-body intraspecies loss rate for state $|1\rangle$ is zero and the three-body loss rate is small enough over typical experimental timescales. The interspecies losses are significant. However the number of lost state $|1\rangle$ atoms is equal to the number of lost state $|2\rangle$ atoms and in the limit $N_2 \ll N_1$, the N_1 reduction is less than $\theta^2/4\,N$. The total atom number loss rate is proportional to N_2 and is also small. So, the relative atom number loss rate for state $|2\rangle$ is much more than for state $|1\rangle$ and θ constantly decreases and α becomes more and more independent of a_{22} keeping Eq. 4.11 still valid. Overall, the calibration with $\theta \ll \pi/2$ is robust against uncertainties in a_{22}, γ_{12} and γ_{22}.

The analytical formula (Eq. 4.9) based on collisional shift qualitatively predicts the shape of the $P_z(N)$ dependence and shows sources of systematic errors. In order to have quantitative agreement we perform the calibration using GPE simulations. The normalized longitudinal spin projection $P_z = (N_2 - N_1)/(N_2 + N_1)$ depends on the total atom number N, the two-photon detuning and the evolution time t:

$$P_z(N, t, \Delta) = \frac{\mathrm{Im}[e^{i(\varphi + 2\pi\Delta\times t)} \int\limits_V 2\,\Psi_2^*\,\Psi_1\,d^3\mathbf{r}]}{\int\limits_V \left(|\Psi_1|^2 + |\Psi_2|^2\right)\,d^3\mathbf{r}}, \tag{4.13}$$

where the wavefunctions $\Psi_1(\mathbf{r}, t, N_0)$ and $\Psi_2(\mathbf{r}, t, N_0)$ are obtained by solving the coupled Gross-Pitaevskii equations (Eq. 2.3) with the initial number of atoms N_0 and using $N = \int\limits_V (|\Psi_1|^2 + |\Psi_2|^2)\, d^3\mathbf{r}$. We obtain about 200 points $\{N_j, I_j\}$ for the dependence $I = \int\limits_V 2\,\Psi_2^*\,\Psi_1\, d^3\mathbf{r}$ vs N by performing numerical simulations for a wide range of the initial number of atoms N_{meas} (from 100 to 2×10^5). We find the complex function

$$I_s(N) = S\left(\{N_j, \mathrm{Re}\left[I_j\right]\}, N\right) + iS\left(\{N_j, \mathrm{Im}\left[I_j\right]\}, N\right), \tag{4.14}$$

where $S(\{x_j, y_j\}, x)$ is a cubic spline interpolating a function $y(x)$. This complex interpolation function (Eq. 4.14) is used to construct a fitting function

$$P_z(N_{\mathrm{meas}}) = A\frac{\mathrm{Im}\left[e^{i\varphi_0} I_s(kN_{\mathrm{meas}})\right]}{kN_{\mathrm{meas}}}, \tag{4.15}$$

where the calibration coefficient $k = N/N_{\mathrm{meas}}$, the phase φ_0 which incorporates the detuning Δ and an amplitude decay factor A are kept as free parameters and the evolution time t is kept fixed and equal to the duration of the Ramsey interferometric sequence. Once the experimental data for P_z vs N_{meas} are fitted with this function, the free parameters are found. The resultant value $k = 1.83(4)$ is dominated by the precision of the $a_{11} - a_{12}$ measurement. Trap anharmonicities can be easily included in the GPE simulations if they significantly change the trapping potential over the BEC extent.

If the calibration is performed with $\theta \ll \pi/2$ and t is equal to the revival time, it is possible to derive analytical expressions which coincide with the GPE equations much better than the collisional shift model. Reducing the three-dimensional coupled GPE to one dimension with Gaussian trial wavefunctions [70], we have obtained Eq. 2.57 and 2.69 which allows one to construct a function $P_z(N)$:

$$P_z(N) = A\cos\left[\frac{4}{3\hbar}\left(1 - \sqrt{\frac{a_{12}}{a_{22}}}\right)\left(\frac{135Na_{11}\hbar^2\bar{\omega}^3\sqrt{m}}{2^{\frac{11}{2}}} + \varphi_0\right)^{\frac{2}{5}} t\right], \tag{4.16}$$

where the amplitude A and phase shift φ_0 are kept as free parameters. When compared with the results of GPE simulations, the dependence looks very similar (Fig. 4.2). Using this function for fitting the experimental data with $P_z(kN)$ gives $k = 1.89$, 3% higher than the result obtained by using GPE simulations. The result can be further improved by the

inclusion of two-body inelastic losses. Eq. 4.16 is very useful if GPE simulations cannot be performed.

4.3 Conclusion

We developed an interferometric atom number calibration and compared with the conventional technique of atom number calibration by BEC condensation threshold. Two techniques give the same calibration coefficients within the systematic errors. Interferometric calibration heavily relies on our a_{12} measurement (Ch. 6). The agreement between the two techniques independently confirms that our measurement of a_{12} is correct at least to within an uncertainty of $0.02\,a_0$. Interferometric calibration technique can be performed in traps with higher level of anharmonicity than the method which uses T_c as the spatial extent of the BEC is much smaller than that of the non-condensed fraction and it is possible to include anharmonic potentials in GPE simulations. We also derived analytics for the atom number calibration which can be used instead of the GPE simulations.

Chapter 5

Self-rephasing and coherence of a two-component Bose-Einstein condensate

Atom interferometry [98, 99] is a powerful method for precision measurements and a long phase accumulation time is desirable for improving sensitivity. Decoherence limits the timescale of an interferometric measurement and is of fundamental importance in quantum information processing. In this regard interparticle interactions can play a detrimental role [44, 30, 100] in interferometry with trapped Bose-Einstein condensates [20, 101, 102]. Nonlinear interactions generate quantum phase diffusion [103] and mean-field driven dephasing [20, 22] which lead to the loss of interferometric contrast. Interaction-induced phase uncertainty has limited the coherence time in a multi-path BEC interferometer to 20 ms [104] and in a BEC double-well interferometer to 0.2 s [102]. Monitoring the local spin coherence in the centre of a two-component Bose-Einstein condensate (BEC) showed a promising decay time of 0.6 s [24]. However, spatially nonuniform growth of the relative phase across the BEC leads to fast dephasing of the condensate order parameter and decay of the fringe visibility [22].

Another mechanism of decoherence is quantum phase diffusion. When a two-

component BEC is prepared by a radiation pulse or by splitting the BEC in a double-well potential, the precision of the splitting is fundamentally limited by the standard quantum limit. After the evolution, nonlinear interactions increase the phase spread of the order parameter and, hence, also reduce the fringe visibility [51]. Collisional losses decrease the coherence even further [105, 29]. Nevertheless, even in this case the coherence can be partly restored [100].

Collisional dephasing can be reduced by tuning the s-wave scattering length to zero in the vicinity of a Feshbach resonance [26]. Another way to minimise detrimental interaction effects is to use noncondensed atoms with lower atomic density [25]. A long coherence time of 58 s was recently achieved (the result is based on a long time extrapolation of the experimental data for the first 5 s) in Ramsey interferometry with trapped cold atoms using rephasing via the identical spin rotation effect (ISRE) [27] and applied to a trapped atomic clock [106].

In this work we demonstrate that the deleterious effect of atomic interactions on BEC coherence can be reversed via mean-field induced rephasing of the condensate wave functions. The periodic self-rephasing has a mechanism different from ISRE rephasing observed in noncondensed atoms [27] and is due to induced collective oscillations of the condensate wave functions. The timely application of a spin echo further enhances the visibility of the Ramsey interference fringes for a trapped ^{87}Rb condensate and prolongs the coherence time to 2.8 s. These findings were recently published in Physical Review A (Rapid Communication) [31].

5.1 Measurements and analysis of Ramsey fringes

In this set of experiments we typically prepare a BEC of 5.5×10^4 atoms unless mentioned otherwise. All atoms are initially condensed in state $|1\rangle \equiv |F = 1, m_F = -1\rangle$. A cigar-shaped magnetic trap on a chip is used (axial trap frequency $f_{\mathrm{ax}} = 97.0(2)$ Hz, radial trap frequency $f_{\mathrm{rad}} = 11.69(3)$ Hz). The magnetic field at the trap bottom is set to the "magic" value 3.228(5) G in order to eliminate the first-order Zeeman shift between the two internal states $|1\rangle$ and $|2\rangle$. We perform Ramsey interferometry with an initially equal

superposition of states $|1\rangle$ and $|2\rangle \equiv |F = 2, m_F = +1\rangle$. The superposition is prepared by a $\pi/2$-pulse formed by the application of 0.7 ms two-photon coupling (two-photon Rabi frequency $\Omega_{2\mathrm{ph}} = 350$ Hz, two-photon detuning $\Delta = -37$ Hz). After an evolution time t, we apply a second, interrogating $\pi/2$-pulse with a phase lag φ variable on a microwave synthesizer (Agilent E8527D). A single absorption image of both components is obtained after a 20 ms drop time.

Immediately after the second pulse we release the atoms, measure the populations N_1 and N_2 from an absorption image and evaluate the normalized atom number difference $P_z = (N_2 - N_1)/(N_1 + N_2)$. We also express P_z from the wavefunctions obtained in our GPE simulations (Eq. 2.10):

$$P_z(N, t, \Delta, \varphi) = \frac{2}{N} \mathrm{Im}\left[e^{i(\varphi + \Delta\, t)} \int \Psi_2^* \, \Psi_1 \, d^3\mathbf{r}\right], \tag{5.1}$$

where $N = N_1 + N_2 = |\Psi_1|^2 + |\Psi_2|^2$ is the total atom number at the evolution time t. This dependence is also used for atom number calibration (Ch. 4.2). According to Eq. 2.10, the visibility obtained in GPE simulations is

$$\mathcal{V} = \frac{2|\int \Psi_2^* \, \Psi_1 \, d^3\mathbf{r}|}{N}, \tag{5.2}$$

which is independent of φ.

As follows from Eq. 5.1, the interference fringe can be obtained in the time (Fig. 5.3b), phase (Fig. 5.1b, 5.1d) or atom number (Fig. 5.1c, 5.1e) domains. For measurements of the visibility (or interferometric contrast) $\mathcal{V}$ and phase noise we have chosen the phase domain because the interference fringe in this case can be obtained without changing the states before the interrogation. The atom number domain was used for atom number calibration (Ch. 4.2). We also used the time domain for measurements of the scattering length a_{22} (Ch. 6).

Once the phase domain is chosen, the interference fringe can be post-corrected using the information from the fringe obtained in the atom number domain. In the approximation of unchanged BEC density, the fringe frequency is determined by the collisional shift (Eq. 2.24). Taking into account the kinetic energy term, a more precise

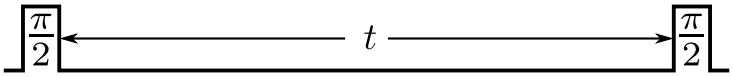

(a) Ramsey sequence

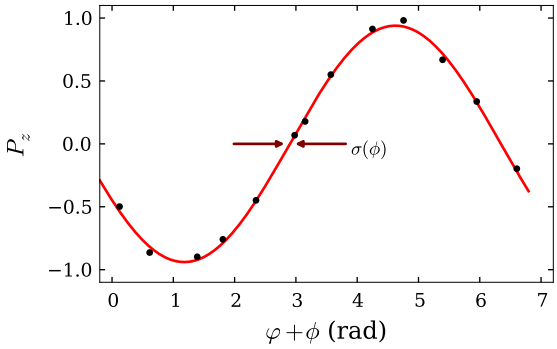

(b) Phase Ramsey at $t = 20$ ms

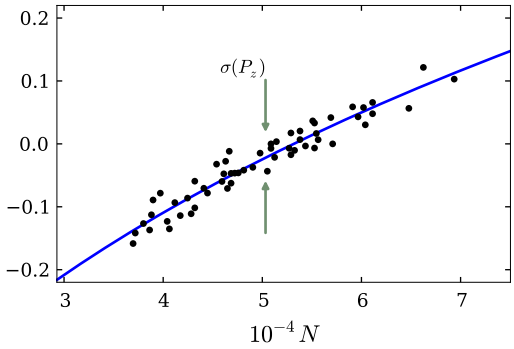

(c) Ramsey with variable N at $t = 20$ ms

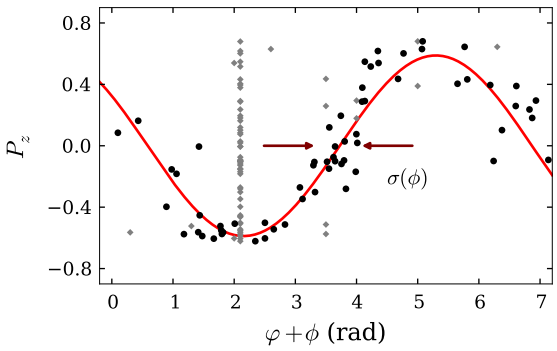

(d) Phase Ramsey at $t = 450$ ms

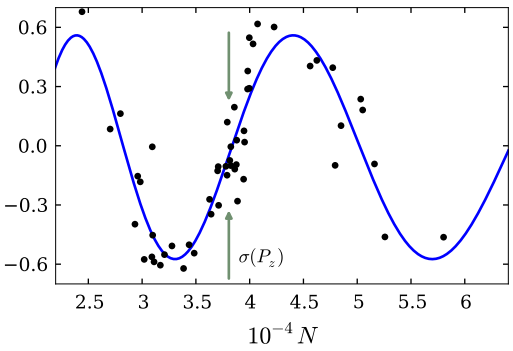

(e) Ramsey with variable N at $t = 450$ ms

Figure 5.1: Ramsey interference in the phase (b, d) and atom number (c, e) domains at 20 ms and 450 ms evolution times obtained with the sequence (a). The relative phase of the two-component BEC depends on the total number of atoms N, which is visible in the atom number domain (c, e). Grey points in (d) stand for the raw phase Ramsey fringe $P_z(\varphi)$, black points ($P_z(\varphi+\phi)$) are corrected for atom number fluctuations. $\sigma(P_z)$ shows the standard deviation of the spin-projection P_z in many experimental realizations. $\sigma(\phi)$ shows the corresponding phase noise.

value of the Ramsey fringe frequency is determined from GPE simulations. However for analysing the data we use a simplified fitting function:

$$P_z(N, t, \Delta, \varphi) = \mathcal{V}(N, t) \cos[\alpha(t)\, N^{2/5}\, t + \Delta\, t + \varphi]. \tag{5.3}$$

The mean-field contribution to the phase is $\phi(t) = \alpha(t)N^{2/5}$ where the coefficient $\alpha(t)$ which is slowly varying with t can be determined from simulations of the coupled GPE; $\alpha(20\text{ ms}) = 0.79$ and $\alpha(450\text{ ms}) = 0.90$. We fit the experimental data $P_z(N)$ for fixed t, with the phase term $\Delta\, t + \varphi$, α and $\mathcal{V}$ set as free parameters (Fig. 5.1c, 5.1e). Our atom number is fluctuating ($\Delta N/N = 10\%$), contributing to $\phi(t)$ and, hence, the phase noise appears due to the atom number fluctuations. This was known to cause phase collapse at evolution times of about 0.5 s [44]. We correct for these fluctuations adding ϕ to φ and obtaining the interference fringe in the corrected phase domain (Fig. 5.1b, 5.1d). Such a correction allows one to perform interferometric measurements on timescales inaccessible otherwise.

5.2 Dephasing of BEC

Interference contrast (or visibility) $\mathcal{V}$ is a common measure of coherence in interferometry. As follows from Eq. 5.2, two components with uniform phase and the same density profiles yield $\mathcal{V} = 1$ in a classical mean-field formalism. When atoms in different internal states have different scattering lengths, there will be a non-uniform dependence of the collisional shift of the atomic transition on the position in the BEC as the condensate has a non-uniform (parabolic) spatial profile in a harmonic trap [21]. The collisional shift, in turn, defines the rate of relative phase growth. Therefore, the order parameter of the two-component BEC decoheres due to the spatially nonuniform growth of the relative phase across the BEC and the interferometric fringe visibility decays [22]. The spatially non-uniform phase reduces the interference contrast in Ramsey interferometry with a BEC; this is approximately described by Eq. 2.20.

The dominant contribution to the phase dynamics at small evolution times is given by a spatially non-uniform collisional shift in the BEC. The density profiles are not

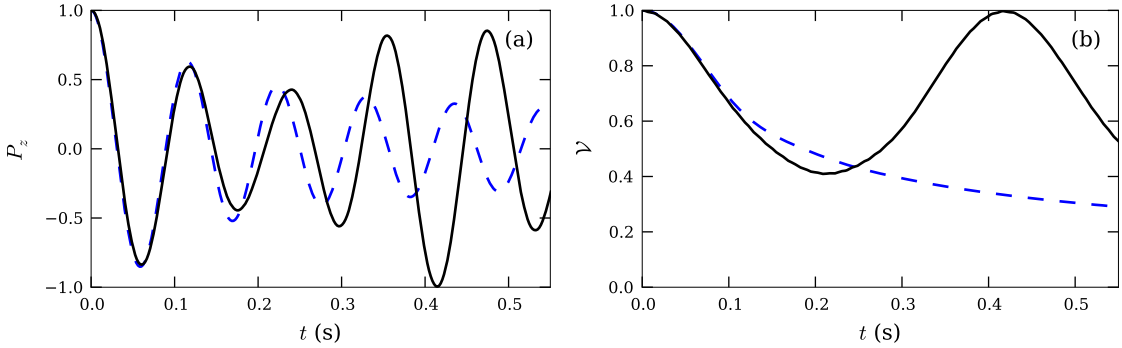

Figure 5.2: Comparison of GPE simulation results (solid lines) and analytical formulas (dashed lines) (Eq. 2.20) for the normalized atom number difference P_z (a) and visibility $\mathcal{V}$ of Ramsey fringes (b). The analytical expression shows good agreement with the GPE simulations at short times; however they disagree at longer evolution times t.

changed significantly at these times, so $\mathcal{V}$ can be calculated in the approximation of unchanged component densities given by the initial Thomas-Fermi profile. In the case of an elongated cigar-shaped trap, the phase dynamics are approximately described by the function $\mathcal{P}(t)$ (Fig.2.19). The visibility is expressed as $\mathcal{V}(t) = |\mathcal{P}(t)|$, and the relative atom number difference in Ramsey interferometry is $P_z(t) = \mathrm{Im}\,[\mathcal{P}(t)]$. This picture qualitatively and quantitatively explains the dephasing at short evolution times $t < 0.15$ s (Fig. 5.2).

The second, interrogating $\pi/2$-pulse transfers the local phase information to the BEC density profiles. In order to visualize the phase information, we plot the local normalized spin-projection $p_z(z) = (n_{1D,2} - n_{1D,1})/(n_{1D,2} + n_{1D,1})$ defined by the experimentally obtained column density profiles $n_1(y,z)$ and $n_2(y,z)$ integrated across the radial direction to one dimension $n_{1D,i}(z) = \int n_j(y,z)\,dy$ (Fig. 5.3). The non-uniform collisional shift (Eq. 2.11) forces the Ramsey fringe in the centre of the cloud to oscillate with a frequency different from the fringe in the outer regions. If the kinetic energy is neglected (which can be done at the very beginning of the evolution), the fringe frequency is determined by the value δf of the collisional shift and the detuning Δ of the coupling radiation from the transition $|1\rangle \rightarrow |2\rangle$. According to [21], the collisional shift of this

transition frequency (2.13) is negative and proportional to the BEC density n. The local fringe frequency ($\delta f + \Delta$) increases with density for positive detuning and decreases for negative detuning. This gives a signature of the sign of the radiation detuning which is positive if the local fringe frequency is higher in the centre of the cloud than near the edges, or the "wavefronts" of p_z look to be "focusing" in time (Fig. 5.3c). Such a simple picture provides a qualitative understanding of the BEC dynamics at the beginning of the evolution.

5.3 Self-rephasing effect

In the temporal evolution of the Ramsey fringe visibility $\mathcal{V}(N,t)$ (initial total atom number $5.5(6)\times10^4$, peak density 7.4×10^{13} cm^{-3}) we observe a decaying periodic structure with peaks and troughs (Fig. 5.6). The initial decrease of visibility is due to the nonuniform growth of the relative phase [22] and the spatial separation of the components [19]. By the end of the first collective oscillation the relative phase is uniform and the two components overlap again (Fig. 5.4). This periodic evolution continues with a slow decay of fringe visibility (decay time of 1.3 s). Inelastic two-body collisions remove atoms from state $|2\rangle$ faster than from state $|1\rangle$ (Sec. 6.6) limiting the maximum fringe contrast to

$$\mathcal{V}_{\max} = 2\sqrt{N_1 N_2}/(N_1+N_2). \tag{5.4}$$

The maximum achievable contrast is less than unity when $N_2 < N_1$ or $N_1 < N_2$ (Fig. 5.6, red dot-dashed line). The coupled GPE model (Fig. 5.6, dot-dashed line) correctly predicts the period of the visibility revivals ($T_{\rm rev} = 0.37$ s), but overestimates their magnitudes.

The origin of the rephasing effect is collective oscillations of the two-component BEC [19]. The ground state of the order parameter for a two-component BEC is different from the ground state of a single component BEC (Fig. 5.4) because the interspecies scattering length (a_{12}) and the intraspecies scattering length (a_{11}, a_{22}) are different and the interaction potentials depend on the value of the population in each state. Using evaporative cooling and thermalisation of the atomic cloud we generate a single condensate in state $|1\rangle$ where the intra-state collisional interactions are completely compensated by

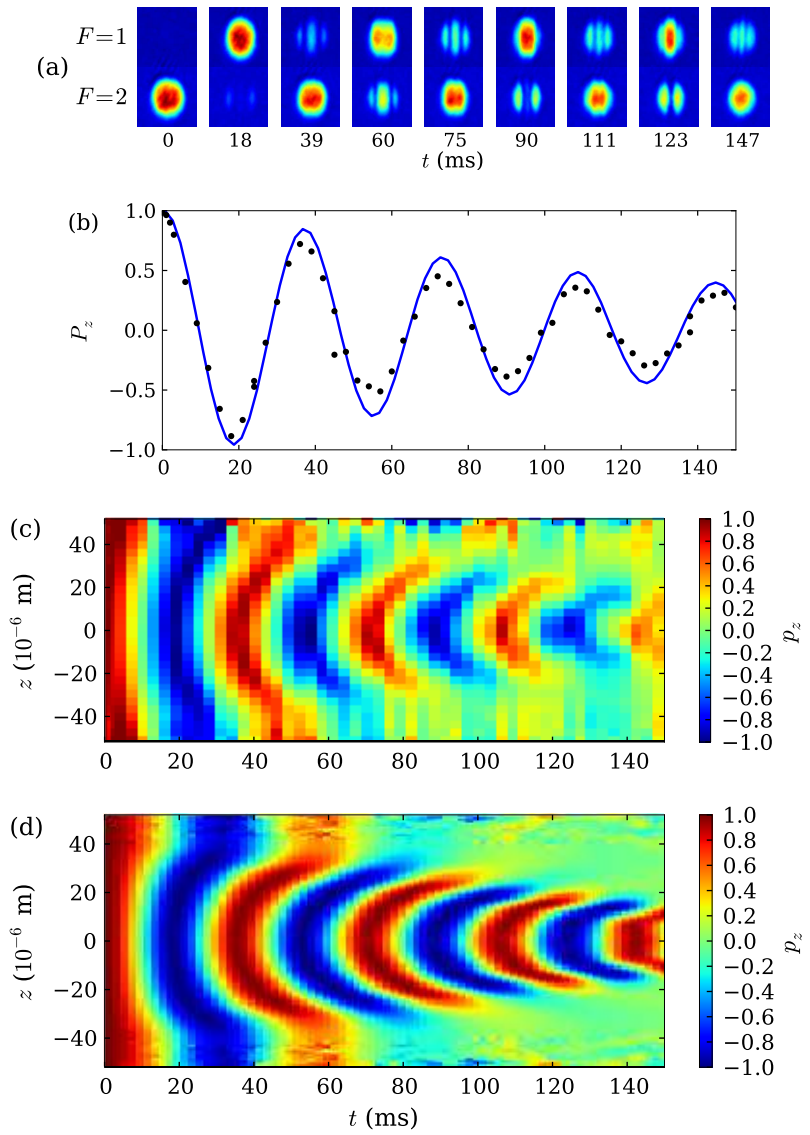

Figure 5.3: Ramsey interferometry at short evolution times. Total numbers of atoms are measured in experimentally obtained density profiles (a) and $P_z = (N_2 - N_1)/(N_2 + N_1)$ is plotted versus the evolution time t (b). The black points are the experimental measurements, the blue solid line is the GPE simulation performed for the experimentally measured detuning $\Delta = 14.0$ Hz and $N = 1.7 \times 10^5$ atoms with no fitting parameters. Axial spin-projection p_z obtained from linear densities in experiment (c) and GPE simulations (d). The spatial dynamics leads to interference in the spatial domain creating interference patterns in the density profiles (a) as well as in the time domain revealing wavefronts of constant phase (c) and (d).

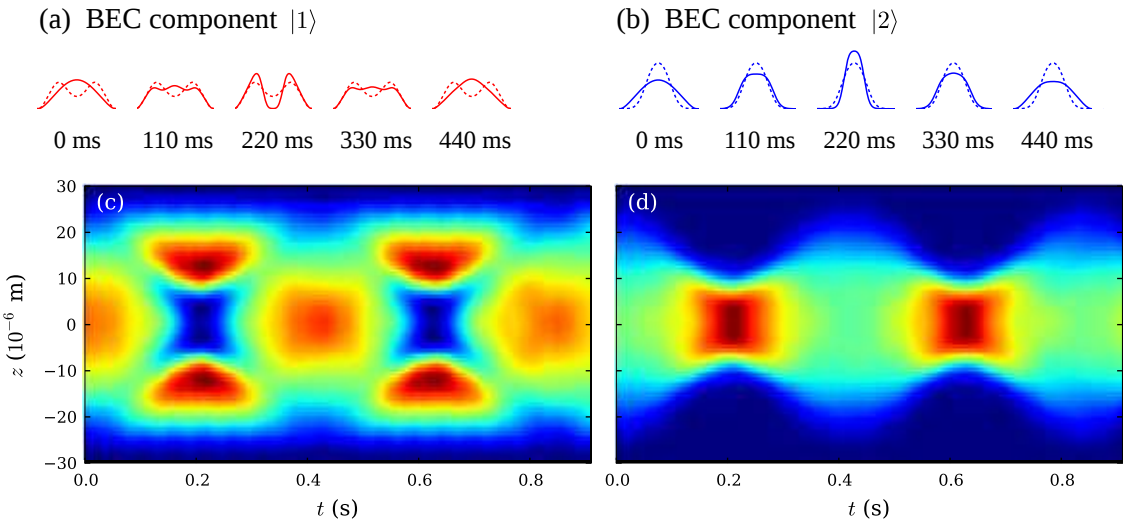

Figure 5.4: Axial density profiles (a, b) (solid lines) of the two BEC components after the preparation $\pi/2$ pulse at different evolution times; also shown in false color scale in (c,d). The ground state [dashed lines (a, b)] of the two-component BEC is different from that of the single-component BEC whose density profile has a parabolic shape. Component 1 [red line (a), false color scale (c)] tends to separate. Component 2 [blue line (b), false color scale (d)] focuses in the middle. After the superposition is created, the initially parabolic density profile oscillates around the two-component ground state. At the turnover points of the oscillations (440 ms) the density profiles coincide again. The two-component ground states are obtained in GPE simulations using the method of propagation in imaginary time. The dynamics of the components are also obtained in GPE simulations ($N = 5.5 \times 10^4$, chemical potential $\mu = 573$ Hz, trap frequencies $f_{\rm ax} = 11.69$ Hz and $f_r = 97.0$ Hz).

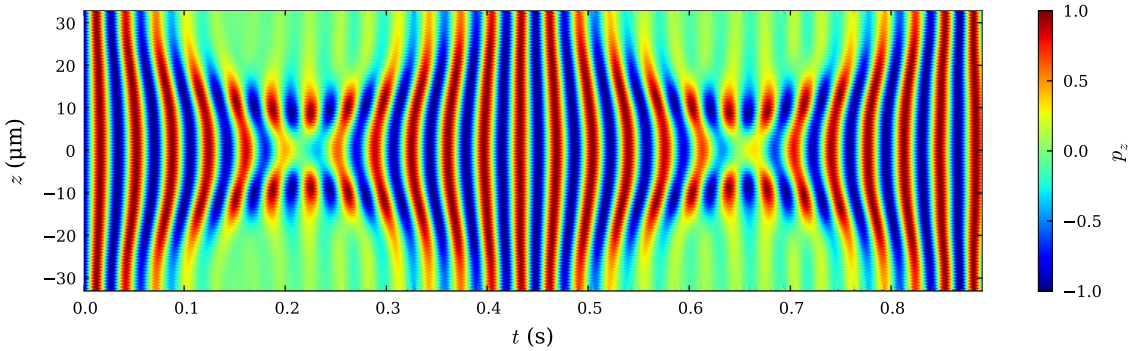

Figure 5.5: Normalized local spin projection $p_z = (n_2 - n_1)/(n_2 + n_1)$ after Ramsey interferometry obtained in coupled GPE simulations ($N = 5.5 \times 10^4$, chemical potential 573 Hz, $\Delta/2\pi = -37$ Hz, no losses). Lines of constant p_z represent wavefronts of relative phase. The mean-field dynamics act to periodically curve the phase wavefronts modulating the contrast of the interference fringes.

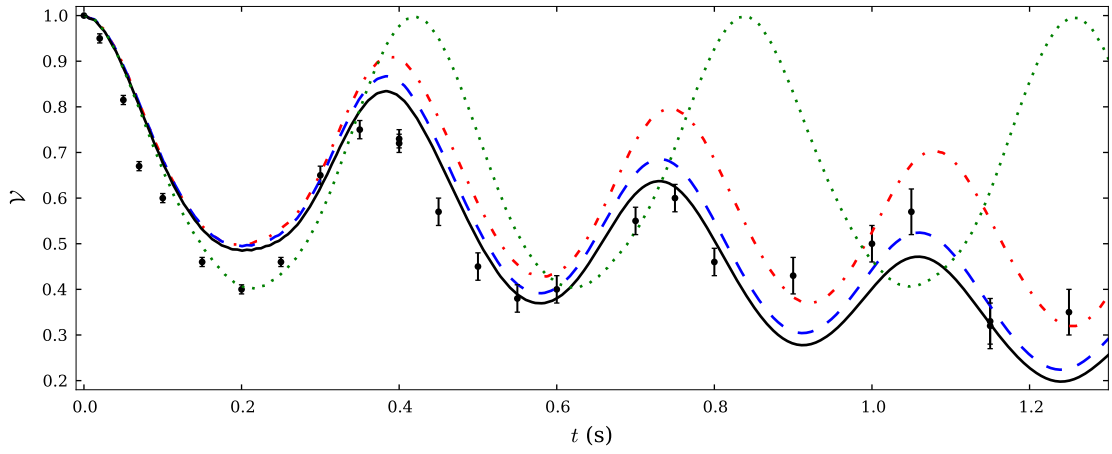

Figure 5.6: Self-rephasing of a two-component BEC. At sufficiently long evolution times the visibility of a Ramsey fringe in a two-component BEC starts to increase by itself. Black points are experimental data, green dotted line is GPE simulation without two-body losses, red dot-dashed line is a GPE simulation with two-body losses, blue dashed line is a truncated Wigner simulation with inclusion of all technical noise, solid black line contains a phenomenological exponential decay with a 10 s time constant.

the parabolic trapping potential. The component $|1\rangle$ is prepared in the ground state. However, the ground state of a two-component BEC differs from the ground state of a single-component condensate (Fig. 5.4, dashed lines): when the two-component condensate is in equilibrium, component $|1\rangle$ is split apart while component $|2\rangle$ focuses in the middle. A $\pi/2$ pulse prepares a nonequilibrium coherent superposition of the two states with modified mean-field interactions so that the difference in collisional energies of the two components just after the application of the pulse is equal to 14.2 Hz while the chemical potential $\mu/2\pi = 573$ Hz and the spatial modes are distinct from those of the two-component ground state (Fig. 5.4, dashed lines). The small differences in the s-wave scattering lengths a_{11}, a_{12}, and a_{22} cause the wave functions of the two components to oscillate out of phase around the ground-state modes as each component tends to minimize the total energy. The local BEC velocity v is proportional to the gradient of the local phase, and thus $\nabla\varphi = 0$ at the turnover points of the oscillations, where φ is the relative phase of BEC. This means that the phase distribution is uniform there giving the maxima of $\mathcal{V}(t)$. At the point of maximum overlap the visibility $\mathcal{V}$ could become almost equal to unity in a lossless situation.

It is possible to estimate the rephasing period analytically using an effective single-component description [71] applied to our three-dimensional situation [70] (Sec. 2.4). According to the effective Schrödinger equation (Eq. 2.53), the combination of collisional energy and trapping potential forms an effective harmonic oscillator potential with trapping frequency

$$\omega_{\text{eff}} = \frac{2}{\sqrt{3}}\sqrt{1 - \sqrt{\frac{a_{12}}{a_{11}}}}\omega_{\text{ax}}. \tag{5.5}$$

The initial Thomas-Fermi density profile can be decomposed into a set of effective harmonic oscillator eigenstates, and the wavefunction of state $|2\rangle$ evolves in time as:

$$\Psi_2(t) = \sum_{k=0}^{\infty} E_{2k}\langle\psi_{2k}|\Psi_2(0)\rangle\psi_{2k}, \tag{5.6}$$

where $E_n = e^{-i\left(n\omega_{\text{eff}}+\frac{1}{2}\omega\right)t}$ is the energy of the n-th harmonic oscillator eigenstate ψ_n. The initial wavefunction $\Psi_2(0)$ is symmetric, and therefore only even eigenstates ψ_{2k} contribute to the evolution. According to Eq. 5.6, the revival frequency is two times the effective

trapping potential frequency:

$$T_{\mathrm{rev}} = \frac{\sqrt{3}}{4 f_{\mathrm{ax}}} \left(1 - \sqrt{\frac{a_{12}}{a_{11}}}\right)^{-\frac{1}{2}}. \tag{5.7}$$

The model yields a revival time of 0.34 s compared to a first coherence revival of 0.39 s obtained in three-dimensional CGPE simulations. However the second (0.74 s) and third (1.08 s) revivals are separated by a time closer to multiples of T_{rev}. This quantitative disagreement can be explained by the inherent limitations of the model which is derived for $n_2 \ll n_1$. In this case the revival period is slightly more than T_{rev} given by equation 5.7, and includes the dependence on a_{22} and N. It is realised when the first $\pi/2$ pulse prepares equally populated states $|1\rangle$ and $|2\rangle$. The atoms are lost faster from state $|2\rangle$ than from state $|1\rangle$, and the condition $n_2 \ll n_1$ is better satisfied at longer evolution times. Also the model suggests that component $|2\rangle$ is surrounded by component $|1\rangle$ which is not valid when the kinetic energy of the single-component BEC becomes comparable or greater than the difference in collisional energies. In fact, the GPE simulations do not show any significant dephasing for the latter case of a small total numbers of atoms.

Simulations of the GP equations without two-body losses show a 100% visibility revival (Fig. 5.6, green dotted line). GPE simulations with the inclusion of two-body collisions (red dashed line) (Eq. 2.3) are in better agreement with the experimental data. As long as the two-body collisions lead to much faster decay of the populations of the states than with three-body collisions, the effect of the latter can be neglected. Indeed, when the BEC is prepared purely in state $|1\rangle$, we observe a slow atom number decay by three-body recombination with a time constant of the order of 100 s. As shown in our measurements, the interspecies loss coefficient $\gamma_{12} = 1.51 \times 10^{-14}$ cm^3/s is much smaller than the intraspecies loss coefficient $\gamma_{22} = 8.1 \times 10^{-14}$ cm^3/s (Sec. 6.6). Therefore atoms are lost asymmetrically from states $|1\rangle$ and $|2\rangle$ and N_2 decreases faster than N_1 (Fig. 5.8a). Inclusion of quantum noise effects via a truncated Wigner approach offers just a slight additional decrease in visibility [29]. Further agreement is achieved by the inclusion of technical noise which is discussed in Sec. 5.6.

5.4 Spin-echo technique

The spin-echo technique was successfully applied in non-condensed clouds in order to reverse decoherence effects [107, 108]. The first attempt was to employ a spin echo to reverse the dephasing of a BEC at short evolution times [64, 109]. It helped to increase the visibility by approximately a factor of two, however the time for $1/e$ decay of the contrast was still too short (170 ms [64] and 33 ms [109]). Here, we combine spin-echo and self-rephasing effects in such way that the mean-field dephasing effects are completely eliminated, as well as the asymmetry due to two-body losses.

We apply a spin-echo at different evolution times symmetrically, i.e., the π-pulse splits the Ramsey sequence in two equal parts (Fig. 5.7a). The application of the spin-echo technique has several advantages. The major contribution to the decrease in visibility in the Ramsey experiment is due to asymmetric two-body losses, i.e., the population of state $|2\rangle$ is lost faster than for state $|1\rangle$. The spin echo reverses the populations of the two states, and the numbers of atoms in the two states become almost equal again at the end of the sequence (Fig. 5.7c) if the π-pulse is symmetrically applied. The spin echo is most effective when applied at the points of the mean-field self-rephasing ($t = 0.37$ s, 0.75 s, 1.05 s), where the two components overlap well and the relative phase is uniform along the condensate. The mean-field formalism reveals that the visibility will have almost complete recovery: the GPE simulations show $\mathcal{V} = 0.99$ for $t = 0.75$ s and $\mathcal{V} = 0.98$ at $t = 1.5$ s. This can serve as a comprehensive test of the remaining BEC coherence: the truncated Wigner simulations predict that the quantum fluctuations reduce the visibility down to $\mathcal{V} = 0.92$ at $t = 1.5$ s [29]. Other decoherence effects reduce the visibility even further. Our experimental data consistently show that the measured visibility is less than even the predictions of the truncated Wigner model: $\mathcal{V} = 0.85$ at $t = 0.75$ s and $\mathcal{V} = 0.75$ at $t = 1.5$ s (Fig. 5.7b). However it is higher than in any other experiment limited by mean-field effects. We introduce an additional exponential decay with a time constant of 10 s to our simulations for the best fit with the spin echo data (black solid line in Fig. 5.7b) and infer an overall coherence time of 2.8 s.

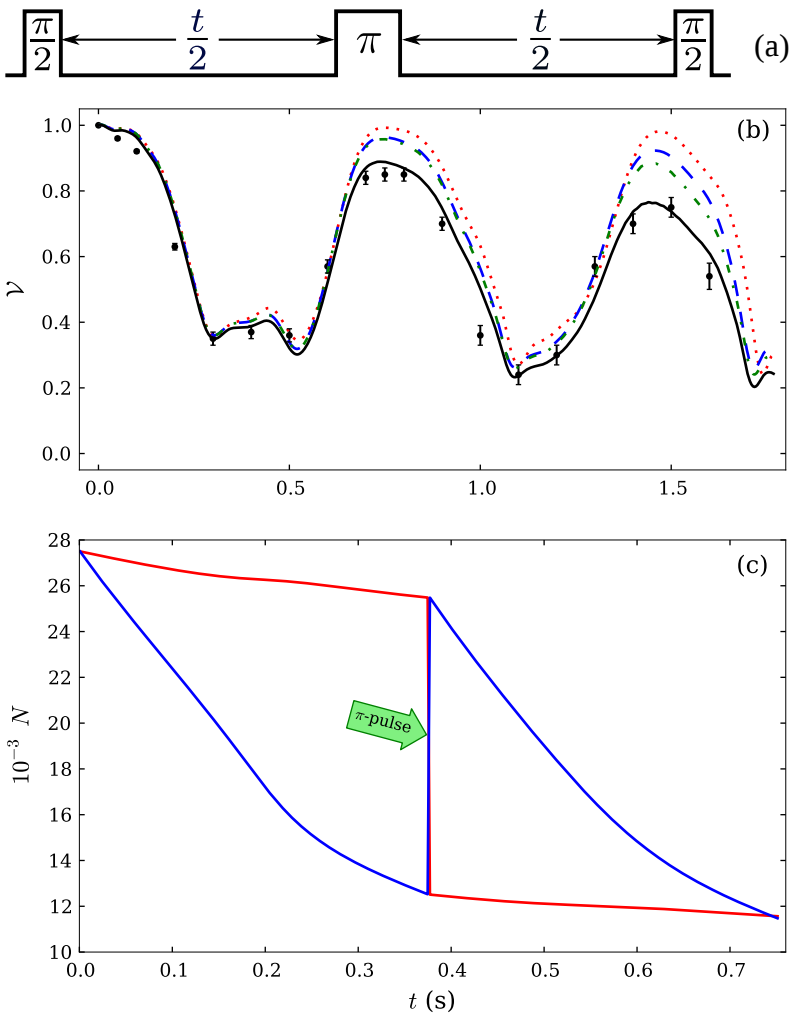

Figure 5.7: A spin-echo sequence (a), in comparison with Ramsey sequence, contains a π-pulse in the middle. The visibility of the spin-echo (b) reaches maxima when the π-pulse is applied synchronously with the mean-field revivals. GPE simulations are represented by the red dotted line, the truncated Wigner simulations results are shown with the blue dashed line, the green dash-dotted line includes all classical noise sources in addition to the quantum noise and the black line includes an additional 10 s exponential decay. In the GPE simulations the visibility reaches almost unity even with losses because they are symmetrized with the spin-echo. Losses of components 1 and 2 are shown in (c) by red and blue lines correspondingly.

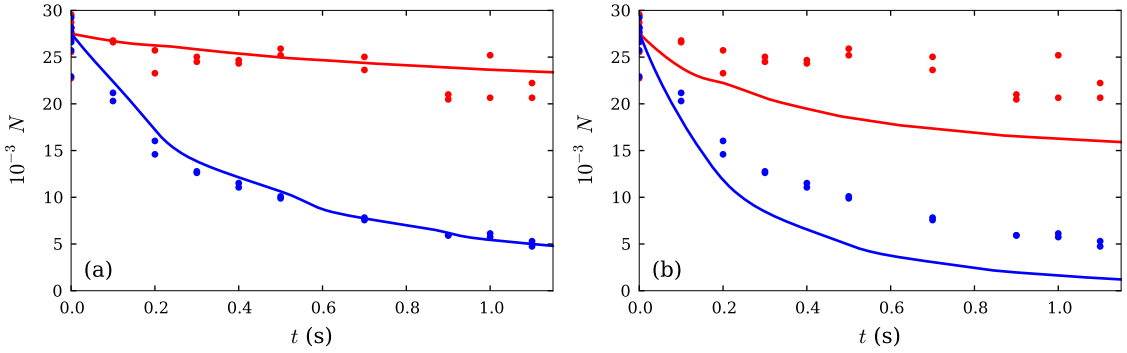

Figure 5.8: Comparison of experimental data points for losses in a two-component BEC prepared by a $\pi/2$-pulse between our measured loss terms (a) and those reported by the Amherst group (b) [19].

5.5 Sensitivity to scattering lengths

The two-component BEC dynamics at long evolution times is very sensitive to the ratios of the s-wave scattering lengths and the two-body loss coefficients. The value of the scattering length for state $|1\rangle$ in ^{87}Rb $a_{11} = 100.40\,a_0$ was obtained in theoretical investigations [39] and is commonly used. The Amherst group [19] measured the values $a_{12} = 97.66\,a_0$ and $a_{22} = 95.00\,a_0$ by fitting two-component BEC collective oscillations with GPE simulations and the two-body loss coefficients $\gamma_{12} = 7.80(19) \times 10^{-14}$ cm^3/s and $\gamma_{22} = 1.194(19) \times 10^{-13}$ cm^3/s by observation of atom number decay in a two-component and a single-component BEC. All of these values were obtained for a two-component BEC in states $|1\rangle$ and $|2\rangle$ in a TOP-trap at a bias magnetic field of 8.32 G. Use of these values in our experiment performed at 3.23 G yield significant disagreement with the experimental data. However the use of theoretical predictions ($a_{11} = 100.44\,a_0$, $a_{12} = 98.09\,a_0$, $a_{22} = 95.47\,a_0$) [21] or the latest predictions ($a_{11} = 100.40\,a_0$, $a_{12} = 98.13\,a_0$, $a_{22} = 95.68\,a_0$) [40, 41] relying on the spectroscopy of the highest bound rovibrational levels in the $^{87}Rb_2$ molecule yields better agreement with the experimental data points.

The values of the two-body loss coefficients also greatly affect the simulations of the BEC dynamics. The Amherst group values of γ_{12} and γ_{22} are not in good agreement with

our experimental data (Fig. 5.8b). Also Satoshi Tojo et al. [43] have recently deduced $\gamma_{22} = 1.04(10) \times 10^{-13}$ cm^3/s from a measurement of the atom number decay in a single-component BEC composed of atoms in state $|F = 2, m_F = -1\rangle$. Our measurements in Ch. 6 ($\gamma_{12} = 1.51 \times 10^{-14}$ cm^3/s and $\gamma_{22} = 8.1 \times 10^{-14}$ cm^3/s) show much better agreement with the experimental data (Fig. 5.8a).

We compared the simulations of Ramsey (Fig. 5.9a) and spin-echo (Fig. 5.9b) interferometry on a two-component BEC with the experimental data for different sets of scattering lengths a_{12} and a_{22}. The range of values $a_{12} = 98.0 \pm 1.0\, a_0$ and $a_{22} = 95.50 \pm 1.0$ were used, and the figures show the results for $a_{12} = 98.0 \pm 0.5\, a_0$ and $a_{22} = 95.50 \pm 0.5\, a_0$. An increase of a_{12} increases the period of the dynamics while an increase of a_{22} makes the minimum visibilities higher. In the Ramsey sequence, the decay of the visibility at the revival points is mostly accounted for by two-body losses of atoms. In the spin-echo sequence the GPE simulations show a visibility close to unity and we add an additional exponential pre-factor to account for the additional visibility decrease. The visibility dynamics in the Ramsey interferometry suggest that the scattering lengths are approximately $a_{12} = 98.2(5)\, a_0$, $a_{22} = 95.3(5)\, a_0$. The uncertainty of such a measurement does not allow to distinguish between the Amherst group results [19] and indirect calculations [41]. In chapter 6 we measure all the scattering properties more precisely.

5.6 Decoherence factors

Five factors affect the coherence of the condensate: mean-field dephasing, asymmetric losses, quantum noise, interaction with non-condensed atoms, and classical perturbations of phase induced by interaction with the environment. The effects of the first two factors (mean-field dephasing and asymmetric losses) can be rectified with the self-rephasing effect and with spin echo. Phase noise (quantum or classical) will also lead to decreasing visibility. If the phase noise is normally distributed and the width of the phase distribution is $\sigma = \left\langle \Delta\varphi^2 \right\rangle^{1/2}$, the visibility decrease is defined as the amplitude of the sinusoidal fit to the scattered points (Fig. 5.10) and can be calculated in the limit of a large number of

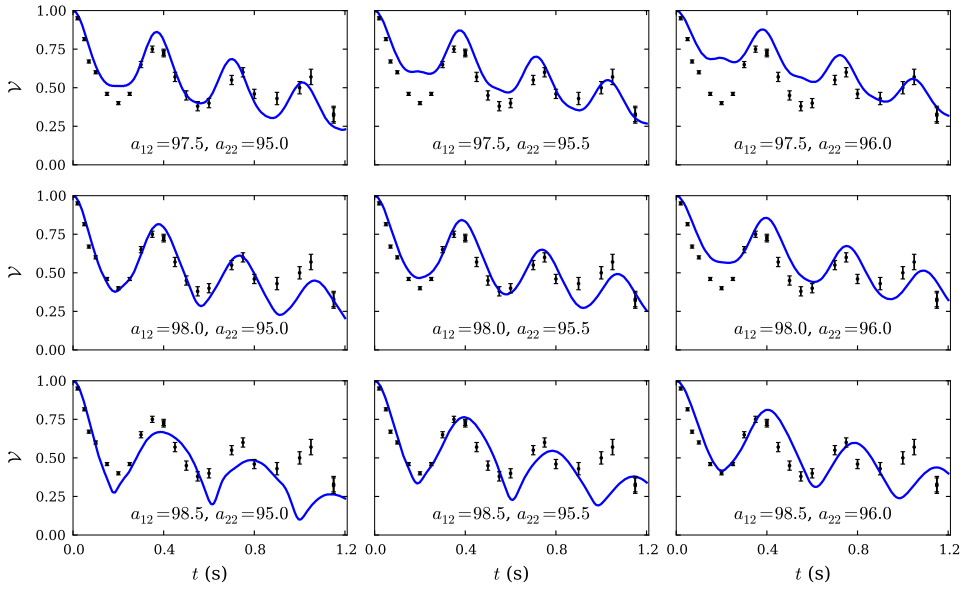

(a) Ramsey sequence

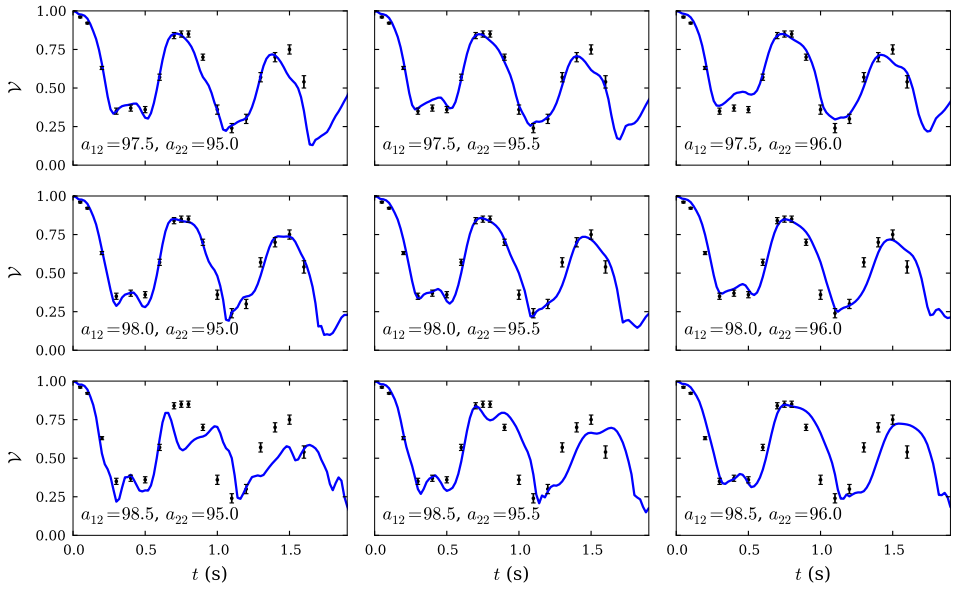

(b) Spin-echo sequence

Figure 5.9: Comparison of experimental data (black points) for Ramsey (a) and spin-echo interferometry (b) of a BEC with $N = 5.5 \times 10^4$ atoms with the results of GPE simulations (solid lines) for different values of the scattering lengths a_{12} and a_{22} while $a_{11} = 100.40\, a_0$. The values of the two-body loss coefficients are $\gamma_{12} = 1.51 \times 10^{-14}$ cm^3/s and $\gamma_{22} = 8.1 \times 10^{-14}$ cm^3/s.

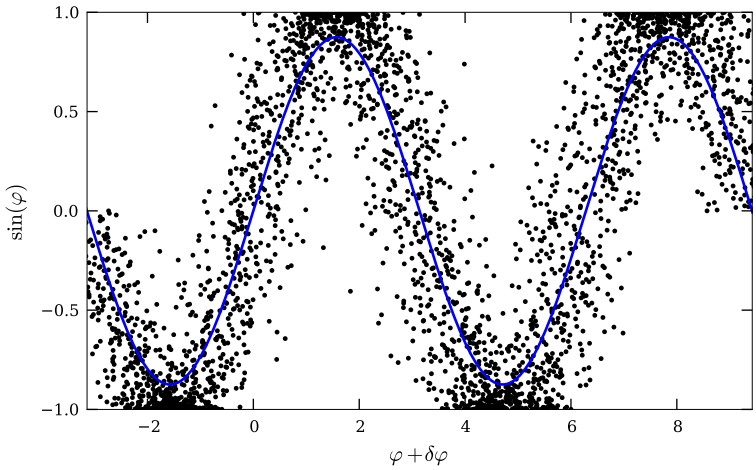

Figure 5.10: The points of a sinusoidal fringe with a normally distributed phase noise $\delta\varphi$, $\sigma = \left\langle \delta\varphi^2 \right\rangle^{1/2} = 0.5$ rad. The phase noise leads to an amplitude reduction of a factor of 0.88 as shown by the solid line representing a sinusoidal fit to the points. This is in agreement with the analytical formula for the amplitude $\mathcal{V}_\sigma = e^{-\sigma^2/2}$.

points:

$$\mathcal{V}_\sigma = \int_{-\infty}^{+\infty} \cos\varphi \, \frac{1}{\sqrt{2\pi\sigma^2}} e^{-\frac{\varphi^2}{2\sigma^2}} \, d\varphi = e^{-\frac{\sigma^2}{2}}. \tag{5.8}$$

In order to obtain a result that does not depend on the number of experimental realizations, we evaluate the phase noise as a first point of an Allan deviation:

$$\sigma = \sqrt{\frac{\langle (\varphi_i - \varphi_{i+1})^2 \rangle}{2}}, \tag{5.9}$$

where the phase in each realization is $\varphi_i = \arcsin\left(\delta P_{z,i}/\mathcal{V}\right)$ using the deviation $\delta P_{z,i}$ of the experimental measurements from the computed dependence $P_z(N)$ (Eq. 5.3).

Firstly, we consider the quantum noise which appears from the interplay of the quantum projection noise from the preparation of the coherent superposition, two-body losses and the nonlinear evolution [29]. Creating a coherent superposition with a $\pi/2$-pulse creates the phase noise determined by the standard quantum limit $\sigma_{\mathrm{SQL}} = 1/\sqrt{N}$. The nonlinear evolution increases this phase noise together with a squeezing process [51]. Two-body losses increase the phase noise together with the uncertainty in the numbers of

atoms in each component [66, 29]. As the phase noise in the nonlinear evolution depends on the initial beamsplitting uncertainty, the increase in relative atom number noise due to the losses increases the phase noise after the two-component condensate evolution.

To characterize the phase decoherence we studied the growth of the phase uncertainty for the Ramsey and spin echo sequences (Fig. 5.11). For each time t we set the phase φ of the second $\pi/2$ pulse to ensure $\langle P_z \rangle = 0$. In each realization we measure N, record the deviation $\delta P_{z,i}$ from the computed atom number dependence (Figs. 5.1b and 5.1d, solid line) and record the relative phase deviation $\delta\phi_i = \arcsin(\delta P_{z,i}/\mathcal{V})$. We use $M = 50$ to 100 realizations for each data point in Fig. 5.11 and evaluate the Allan deviation $\sigma(\phi)$ for the duration of an experimental cycle (50 s). The error bars on each point in Fig. 5.11 represent the statistical uncertainty of $\sigma(\phi)$ and are calculated as $\sigma(\phi)/\sqrt{M-1}$. The truncated Wigner simulations show a phase noise of $\sigma = 0.08$ rad at $t = 1.5$ s in spin-echo sequence (Fig. 5.11b) which suggests a visibility decrease by a factor of 0.997. Nevertheless, the visibility shown by the simulations $\mathcal{V} = 0.92$ is significantly less than in the mean-field calculations (Fig. 5.7b). Therefore, phase noise is not the only effect of quantum noise because of its multi-mode nature. Our experimental points show $\mathcal{V} = 0.75$ for $t = 1.5$ s which suggests other sources of decoherence.

There are several sources of technical phase noise: local oscillator instability, imaging noise and preparation pulse instability (or instability of the two-photon Rabi frequency). The local oscillator instability was measured in Ramsey interferometry with cold non-condensed atoms (red points at Fig. 5.11). In the Ramsey sequence, the long-term drift (with the time constant $\Delta\tau = 50$ s) and short-term fluctuations (with the time constant $\Delta\tau \approx t$) both contribute to the phase noise expressed as Eq. 5.9. The phase noise in the spin-echo sequence directly measures the Allan deviation for time $t/2$ in such a way that $\sigma = \sqrt{2}\,\sigma_{\mathrm{Allan}}(t/2)$ if there are no other sources of noise, i.e., the local oscillator contribution to the spin-echo sequence is determined by the short-term stability.

Imaging noise contributes to the measured phase uncertainty in the following way. The relative phase in the Ramsey sequence is modelled with the dependence $\alpha(t)\, N^{2/5}\, t$ (Eq. 5.3). Therefore, the phase noise depends on the uncertainty of the

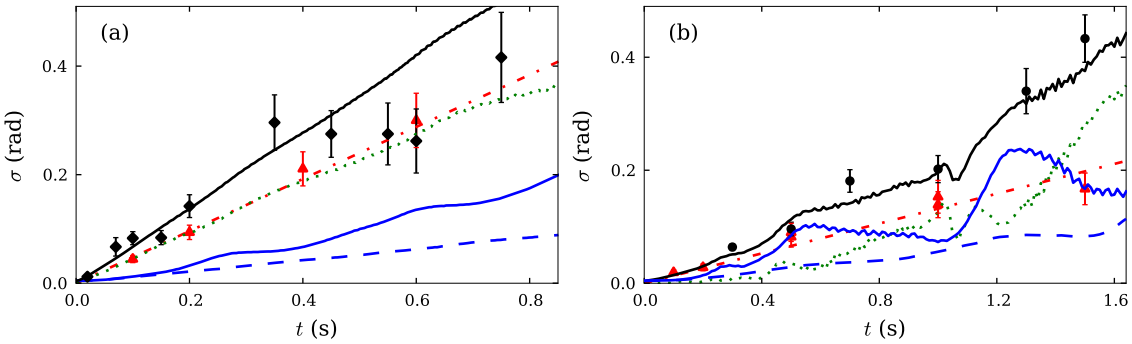

Figure 5.11: Phase uncertainty growth in Ramsey (a) and spin echo (b) sequences for the two-component BEC (black circles) and noncondensed cold atoms (red triangles). The blue dashed lines show the effect of quantum noise simulated with the truncated Wigner method. The red dash-dotted lines indicate the contribution from MW frequency fluctuations. The black solid lines show the simulated combined effect of quantum and classical noise.

total number of atoms, and total number of atoms instability suggests that these fluctuations will make the phase absolutely random at a certain time (called "phase collapse" in [44]). We use the post-correction of experimental points using the dependence $P_z(N)$ (Fig. 5.1 (c), (e)), so that our atom number uncertainty $\Delta N/N = 0.023$ is determined by the imaging noise rather than the BEC preparation instability (Eq. 3.43). This type of phase noise is given by

$$\sigma_{\text{img}} = \frac{2}{5}\,\alpha(t)\,N^{\frac{2}{5}}\,\frac{\Delta N}{N}\,t. \tag{5.10}$$

In the case of the spin-echo sequence, the dependence of imaging noise on the evolution time is less trivial (Fig. 5.11b) and is obtained in the GPE simulations performed for different total numbers of atoms.

Another possible source of phase uncertainty is the fluctuations and drifts of the two-photon Rabi frequency caused by fluctuations of RF and microwave Rabi radiation powers and can be eliminated using a power feedback loop. Fluctuations of the intermediate state detuning due to magnetic field noise also contributes to fluctuations in the two-photon

Rabi frequency at the level of $\sim 0.3\%$. The preparation pulse area fluctuations measured by observations of fluctuations in P_z after the $\pi/2$ splitting are usually at the level of $\Delta\theta = 0.02$ rad in this experiment. In the case of absence of collective oscillations, this would lead to extra phase noise $\Delta\varphi = \chi N \Delta\theta t$. This relation is roughly satisfied when $\chi \propto (a_{11}+a_{22}-2a_{12})$ is far from zero. However, in our case $\chi \approx 0$, and the phase noise from this should be calculated in the Monte-Carlo GPE simulations where the realizations of a BEC with different splitting angle θ are performed. We include a Gaussian distribution of noise $\Delta\theta$ in the preparation pulses, and its action combined with the quantum noise is shown by the solid blue lines (Fig. 5.11).

Another possible factor of decoherence is the effect of finite Bose-gas temperatures. This is a rather unexplored area. The problem of BEC coherence at low temperatures $T/T_c \ll 1$ has been considered for the case of a homogeneous Bose gas [30]. Accordingly, decoherence due to thermal excitations is defined by the diffusion coefficient $\mathcal{D}$ so that the condensate phase variance in the absence of other decoherence mechanisms depends on time as:

$$\left\langle \Delta\phi^2 \right\rangle = 2\mathcal{D}t. \tag{5.11}$$

In the limit of low temperatures T the diffusion coefficient can be approximately estimated [30]

$$\mathcal{D} \approx \frac{0.3036g}{\hbar V}\left(\frac{k_B T}{ng}\right)^4, \qquad \text{for} \quad \frac{k_B T}{ng} \to 0, \tag{5.12}$$

where V is the condensate volume, $g = 4\pi\hbar^2 a/m$ is the interaction coefficient and n is the BEC density. It is worth mentioning that the same decoherence mechanism is one of the limiting factors in spin-squeezing experiments [110]. Our experiments are performed in an harmonic trap; however we use equation 5.12 as a first approximation but take n equal to the BEC mean density and $V = \frac{4}{3}\pi R_{\text{rad}}^2 R_{\text{ax}}$ as the BEC volume defined by its radii. Substituting our experimental parameters and the temperature $T = 0.2\,T_c$ yields a coherence time $t_c \approx 1/\mathcal{D} = 13$ s. In the measurements of the decay of the visibility in the spin-echo sequence, we observe an additional decay of fringe visibility which we model with an exponential pre-factor decaying with a time constant of 10 s (Fig. 5.7b). This value of the additional decay suggests that decoherence due to the finite temperature can

be responsible for this extra decay and could accurately be accounted for by truncated Wigner simulations in the experimentally relevant case of a Bose gas in an harmonic trap at $0 < T < T_c$.

We account for all decoherence factors by including their effect in the simulations and evaluate the phase and amplitude coherence times. We consider a two-component BEC to be incoherent if the phase noise reaches a value of $\sqrt{2}$. If the visibility is dependent only on the phase noise, the corresponding visibility reaches the value $1/e$ (Eq. 5.8). However, the phase noise does not explain all of the visibility decay in the truncated Wigner simulations and the experiment which exhibit additional fringe amplitude decay, probably due to multi-mode excitations caused by quantum noise and finite temperature effects. As such, the amplitude coherence time should be shorter than the phase coherence time.

In our work we determine two kinds of coherence time. The first is the time at which the visibility maximum drops by $1/e$ (amplitude coherence time). The simulations show that the amplitude coherence time is 1.3 s in Ramsey interferometry and 2.8 s in interferometry with a spin-echo π-pulse when all the sources of noise are included. Without these factors, the coherence time in Ramsey interferometry is 2.6 s (Fig. 5.12a) and 9.5 s with spin echo (Fig. 5.12b), as shown by the truncated Wigner simulations for a BEC at zero temperature. Secondly, we determine the phase coherence time at which the phase becomes random ($\delta\varphi = \sqrt{2}$). The phase coherence time in the Ramsey sequence is 2.2 s and 3.3 s in the spin-echo sequence when all the classical sources of noise are included. According to the results of the simulations, the coherence time is prolonged up to 11 s in the Ramsey (Fig. 5.12c) and 14 s in the spin-echo (Fig. 5.12d) sequences when there are no sources of decoherence and only unavoidable quantum noise is present. The results obtained in the truncated Wigner simulations without any decoherence sources except fundamental quantum noise can possibly be achieved once the sources of technical noise are eliminated and the BEC is prepared at lower temperatures.

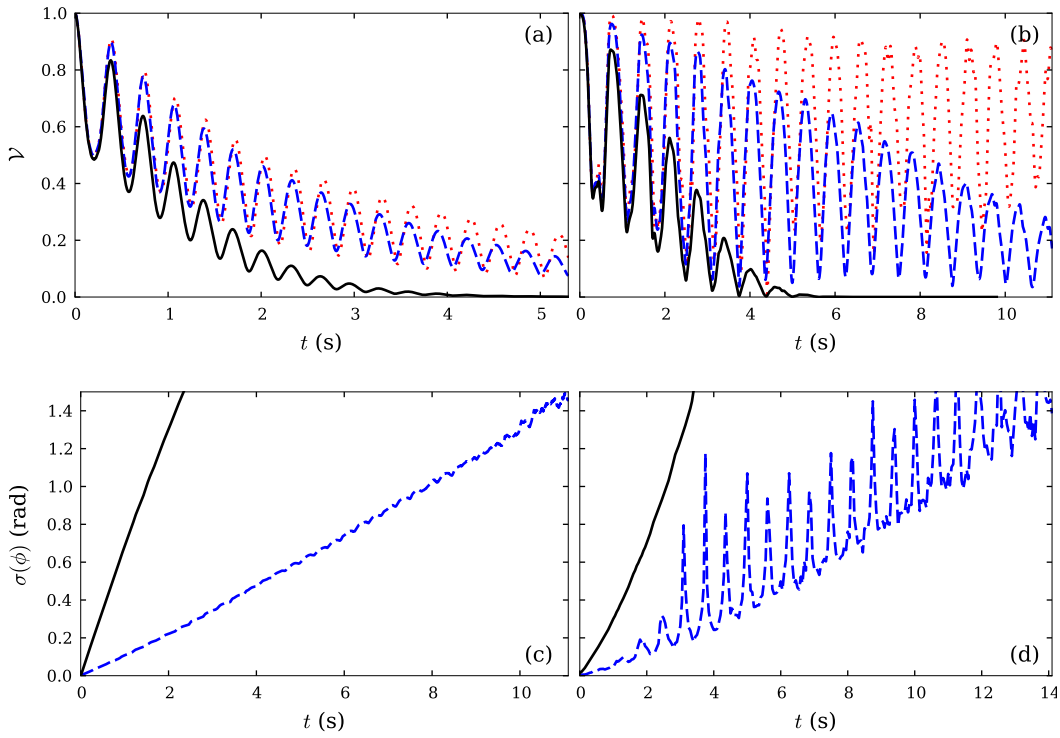

Figure 5.12: Ramsey (a) and spin-echo (b) visibilities simulated for long evolution times with the truncated Wigner method (blue dashed lines) with the inclusion of classical noise (black solid lines) which allow one to infer amplitude coherence times. For the comparison, the results of the coupled GPE simulations are shown (red dotted lines). The widths of the noise distribution in the Ramsey (c) and spin-echo (d) sequences define the phase coherence times at which the phase noise is equal to $\sqrt{2}$ rad.

5.7 Conclusion

In this chapter we have observed that the mean-field induced collisional dephasing is reversed due to periodic collective oscillations in a two-component BEC. The synchronized application of a spin echo significantly enhances the self-rephasing, allowing us to record a visibility of 0.75 at an evolution time of 1.5 s. The quantum noise simulations consider the effects of asymmetric two-body losses and quantum phase diffusion on the BEC coherence. Together with evaluations of the classical noise and single-particle coherence, the simulations allow us to estimate a condensate coherence time of 2.8 s, the longest coherence time for an interacting quantum degenerate gas. We observed that the use of previously reported values of the scattering lengths [19] in the GPE simulations does not reproduce our data. Therefore we performed our own measurement and report the findings in Ch. 6.

Chapter 6

Precision measurements of s-wave scattering lengths in ^{87}Rb

Precise knowledge of values of scattering lengths is very important for calculating clock shifts and modelling BEC dynamics. The scattering lengths of ^{87}Rb atoms in the $F = 1$ or $F = 2$ states are very close to each other (maximum difference is of the order of 5%) due to the particular properties of the singlet and triplet $^{87}\mathrm{Rb} + {}^{87}\mathrm{Rb}$ interaction potentials [35]. Coherent superpositions of these states are used in trapped atomic clocks [25, 27] and spin-squeezing experiments [47, 48]. The non-equilibrium dynamics of mixtures of these states is very sensitive to differences between the scattering lengths of the species involved [19, 42]. Frequency shifts in trapped atomic clocks are also dependent on the differences between the scattering lengths rather than their absolute values [21]. For example, the collisional frequency shift in a trapped atomic clock made from an equal superposition of the two states with similar scattering amplitudes is proportional to the difference between the intraspecies scattering lengths $(a_{11} - a_{22})$. The spin squeezing rate in a fully overlapping two-component BEC is defined by the nonlinearity χ [51] which, in turn, is proportional to $(a_{11} + a_{22} - 2a_{12})$ [111, 48]. Scattering length measurements can also provide a way to monitor drifts of fundamental constants. It was recently shown by Chin and Flambaum [45] that precise measurements of scattering lengths can be very sensitive to drifts of the electron to proton mass ratio m_e/m_p.

Our states of interest $|1\rangle \equiv |1,-1\rangle$ and $|2\rangle \equiv |2,+1\rangle$ are the only ones in ^{87}Rb which have the same magnetic moment and are magnetically trappable. This makes these states of great interest for magnetically trapped atomic clocks and interferometry applications. Thus, accurate knowledge of the scattering lengths for these states is very important for a broad range of applications.

In this chapter we develop a new method for the precision measurement of interspecies scattering lengths using collective oscillations in a two-component BEC. The method is virtually decoupled from one of the intraspecies scattering lengths, the number of atoms and loss terms. In the experiment with a two-component BEC composed of internal states $|1\rangle \equiv |F=1,\ m_F=-1\rangle$ and $|2\rangle \equiv |F=2,\ m_F=1\rangle$ we measure $a_{12} = 98.006(16)\,a_0$. Based on this value, we find $a_{22} = 95.44(7)\,a_0$ in Ramsey interferometry. Also we obtain the two-body loss coefficients $\gamma_{12} = 1.51(18)\times 10^{-14}$ cm^3/s and $\gamma_{22} = 8.1(3)\times 10^{-14}$ cm^3/s.

6.1 Previous measurements of scattering lengths

Scattering lengths for our states of interest were finely predicted in theoretical studies by the group of S. Kokkelmans in 2002 ($a_{11} = 100.44\,a_0$, $a_{12} = 98.09\,a_0$, $a_{22} = 95.47\,a_0$, where a_0 is Bohr radius) [35, 21]. In fact, the improved theory of inter-atomic scattering now provides values with only small variations from the early prediction ($a_{11} = 100.40(10)a_0$, $a_{12} = 98.13(10)$, $a_{22} = 95.68(10)$) [40, 41].

One of the first measurements of the scattering length $a_{11} = 87(21)\,a_0$ performed by Newbury et al. [33] was based on the rethermalization rate of a cold atomic cloud. Observations of losses in a two-component BEC [14] allowed one to theoretically deduce $a_{11} = 106(6)\,a_0$ [34]. Measurements of frequency shifts with cold atoms and BECs preformed in 2002 [21] allowed one to measure $a_{22} - a_{11} = -4.85(31)\,a_0$, which is in a good agreement with recent theoretical studies. However it was pointed out that the atom number calibration could affect this result by $0.1\,a_0$. In the experiment both components were trapped at the "magic" magnetic field $B = 3.23$ G in a Ioffe-Pritchard magnetic trap which ensures the same magnetic moments, Zeeman shifts and trap frequencies for both

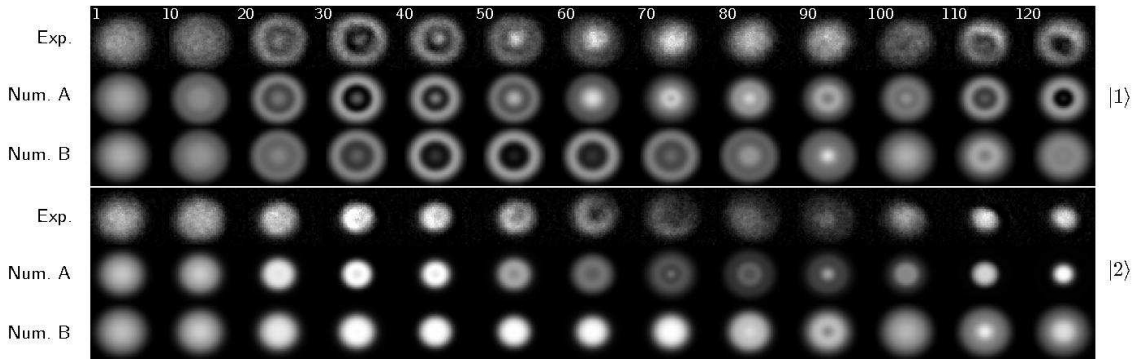

Figure 6.1: Adapted from reference [19]: Top view of a time-sequence of experimental and numerical density profiles for $N = 3.50(5) \times 10^5$ ^{87}Rb atoms with equal populations in the $|1\rangle$ and $|2\rangle$ states. The first row shows the measured density profiles for the $|1\rangle$ atoms, while the second and third rows give numerical results including losses and different trap frequencies (Num. A) and without those additional model features (Num. B). A similar arrangement is given for the $|2\rangle$ atoms in the fourth, fifth, and sixth rows. The field of view in all pictures is approximately 100 μm on a side. The evolution time (in ms) for each column is indicated in the top row.

components.

A completely different method was used in the group of D. Hall. The non-equilibrium dynamics without significant damping was observed in a two-component Bose-Einstein condensate [19]. Comparing experimental images with multiple numerical simulations using coupled GPE model (Fig. 6.1) allowed the fitting of the scattering lengths a_{12} and a_{22} assuming $a_{11} = 100.4\, a_0$. During the evolution the scattering lengths affect the dynamics in such way that it is sensitive to differences in the scattering lengths. For equal populations of the two states the evolution is sensitive to the two scattering lengths differences: $a_{11} - a_{12}$ and $a_{11} - a_{22}$. However, both parameters are present in the Gross-Pitaevskii Eqs. 2.3 and cannot be obtained independently from each other. In addition, it was pointed out that the dynamics are very sensitive to the inter- and intra-species two-body loss coefficients γ_{12} and γ_{22}. The rates γ_{12} and γ_{22} were measured by the same group in an independent study and reported together with the values of scattering

lengths [19]. The calibration of the absolute number of atoms is very important and greatly affects the measurements of γ_{22} [112]. An additional complexity of the experiment is the use of a time-averaged orbiting potential (TOP) magnetic trap in which normally the positions of the potentials for both components do not exactly coincide resulting in a periodic separation [17]. Nevertheless, a magnetic field $B = 8.32(2)$ G was found to produce coinciding trap potential minima for the particular experimental arrangement. This resulted in slightly different trap frequencies for both components, and the GPE simulations of the two-component dynamics required precise knowledge of both trap frequencies. Finally, the results obtained in that work ($a_{12} = 97.66\,a_0$, $a_{22} = 95.0\,a_0$) seems to give good agreement with the obtained experimental data. However they are vastly different from the theoretical studies ($a_{12} = 98.13(10)\,a_0$, $a_{22} = 95.68(10)\,a_0$) given the error bars of the theoretical calculations. It is worth mentioning that a very similar method was recently used to characterize the interspecies scattering length near a magnetic Feshbach resonance in ^{87}Rb [42].

Another method, interferometric measurement of scattering lengths [21], also requires precise knowledge of the absolute number calibration. The method based on collective oscillations [19] could possibly give better precision and allows one to extract a_{12}. However all the scattering lengths are coupled together in the GPE modelling, loss coefficients are required to be well characterised, features of the TOP trap should be taken into account and the absolute atom number calibration is required to be carefully performed.

While the interferometric study and the collective oscillations method have certainly improved our knowledge of the scattering lengths in ^{87}Rb, the coupled nature of the dynamics and many systematic uncertainties (absolute atom number calibration, dependence on loss coefficients, sensitivity to trap dynamics) has led us to develop a more robust technique of a_{12} measurement which is uncoupled to a_{22}, does not rely on a stringent absolute atom number calibration and has reduced dependence on two-body loss coefficients.

6.2 Effect of interspecies scattering length on two-component BEC dynamics

We firstly analyse the problem using the effective single-component Schrödinger equation 2.61 for the state $|2\rangle$,

$$\begin{aligned} i\hbar\frac{\partial\Psi_2}{\partial t} &= \left[-\frac{\hbar^2}{2m}\frac{\partial^2}{\partial z^2} + \frac{1}{2}m\omega_{\text{eff}}^2 z^2\right]\Psi_2, \\ \text{where} \quad \omega_{\text{eff}} &= \frac{2}{\sqrt{3}}\sqrt{1-\sqrt{\frac{a_{12}}{a_{11}}}}\omega_z, \end{aligned} \tag{6.1}$$

which can be applied to our two-component BEC when the number of atoms in state $|2\rangle$ is much less than the total number of atoms in the BEC. The solution of Eq. 6.1 is spatially symmetric (as well as the initial wavefunction given by the parabolic Thomas-Fermi (TF) profile) and can be expressed in terms of even harmonic oscillator eigenstates (Eq. 2.71). Therefore, the wavefunction of state $|2\rangle$ exhibits periodic focusing in a trapped two-component BEC with twice the harmonic oscillator frequency ω_{eff}/π, or the period of the collective oscillations:

$$T_{\text{col}} = \frac{\sqrt{3}}{4f_z}\left(1-\sqrt{\frac{a_{12}}{a_{11}}}\right)^{-\frac{1}{2}}. \tag{6.2}$$

This is valid only if the total number of atoms is large enough for the initial BEC in state $|1\rangle$ to have a TF radius much larger than the size of first harmonic oscillator eigenstates (Eq. 2.68).

As follows from the Eq. 6.2, the period of the collective oscillations depends only on the trapping potential frequency and a_{12}/a_{11}. Assuming $a_{11} = 100.40\,a_0$, it is possible to measure a_{12} independently of the total number of atoms N, loss terms and a_{22}. We check the limits of validity of these assumptions using CGPE simulations. First of all, the effective single-component theory is valid when N is sufficiently large (Eq. 2.68), and we obtain $N > 3\times10^4$ (Fig. 6.3c) to be enough for the precision measurements under our conditions (trap frequencies $(11.507, 98.25, 101.0)$ Hz). On the other hand, the effective single-component theory is derived under the assumption that the density of component $|2\rangle$ n_2 is much less than total BEC density n. If the two-component BEC is prepared by a

pulse with area $\theta \ll \pi/2$, this condition is satisfied. Analytical calculations using Eq. 2.71 show that $n_2 \ll n$ when the preparation pulse angle $\theta \leq \pi/5$ (Fig. 6.2).

The coupled GPE simulations also show that for a sufficiently small preparation pulse ($\theta \leq \pi/5$) the dependence of the focusing dynamics period on θ is suppressed (Fig. 6.3d). For small θ and our trap parameters, the period of oscillations is independent of the total atom number when $N > 3 \times 10^4$ (Fig. 6.3c) which allows one to avoid the problem of precise absolute atom number calibration. It is also clearly visible that for $N = 10^5$ and $\theta = \pi/10$ the dynamics does not significantly depend on a_{22} (Fig. 6.3b). Nevertheless, the period T_{rev} strongly depends on a_{12} as clearly visible in Fig. 6.3a.

In conclusion of this section, a_{12} can be measured independently of a_{22}, N and the collisional loss terms if sufficiently large atom numbers N are used, along with a sufficiently short preparation pulse $\theta \ll \pi/2$.

6.3 Measurement sequence and convergence of analysis

Even though we can measure a_{12} almost independently of the other parameters, the scattering length a_{22} and the two-body loss coefficients γ_{12} and γ_{22} are also of interest. In order to find all the parameters we use an iterative cycle of data processing until convergence (Fig. 6.4).

The time dependence of collective oscillations of the lightly populated component $|2\rangle$ is crucially dependent on the a_{12}/a_{11} ratio. In order to account for the residual dependence on the scattering length a_{22}, the total atom number N and the two-body loss coefficients we carry out measurements and analysis of the data in the following way. We use the latest theoretical predictions of the scattering length values ($a_{12} = 98.13\,a_0$ and $a_{22} = 95.68\,a_0$) [40, 41] and experimental values of the two-body loss coefficients measured at 8.32 G ($\gamma_{12} = 7.80 \times 10^{-20}$ m$^3/s$ and $\gamma_{22} = 1.194 \times 10^{-19}$ m$^3/s$) [19] as initial parameters. In the first iteration we use these values in the interferometric calibration of the total atom number N [31]. We measure the two-body loss coefficients using the atom number calibration results. Then we find a new value of a_{12} from the collective oscillations dynamics. In the next step we find a_{22} from Ramsey interferometry measurements with

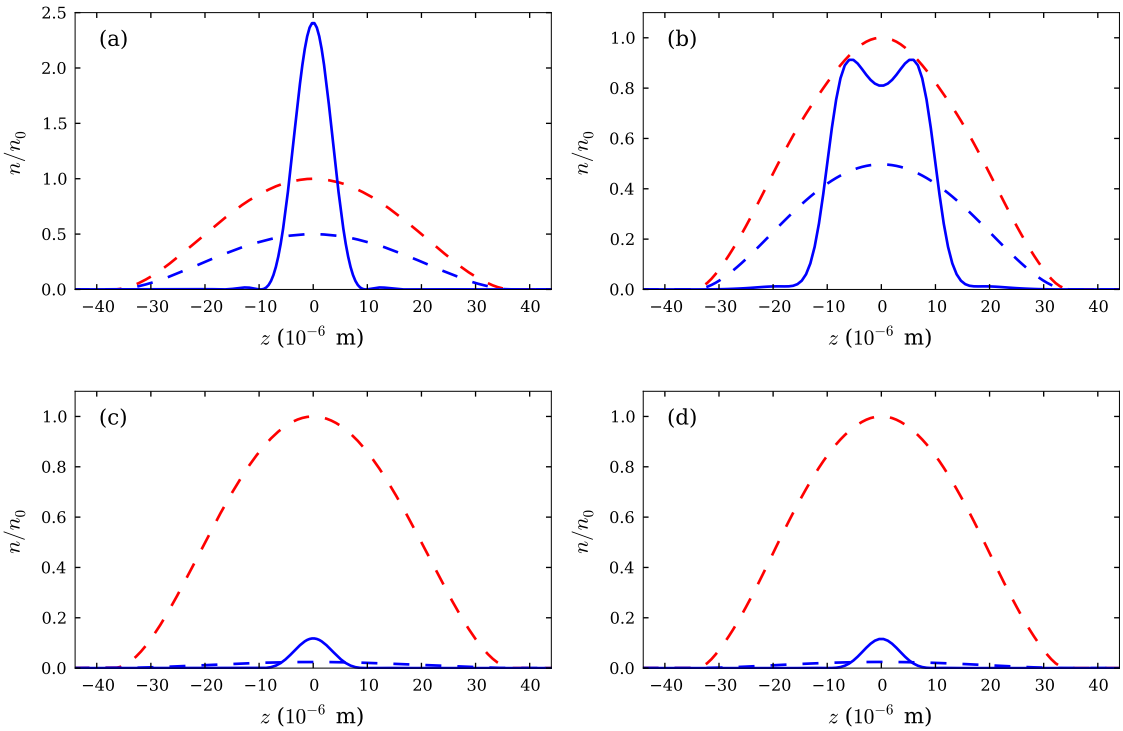

Figure 6.2: Evolution of linear density $n(z) = \iint n_{3D}(x, y, z)\, dx\, dy$ of component $|2\rangle$ in a two-component BEC predicted by the analytical model (a, c) in comparison with CGPE simulations (b, d) ($N = 10^5$). The two-component BEC is prepared by a $\pi/2$ (a, b) or $\pi/10$ (c, d) pulse. During the evolution of a two-component BEC, component $|2\rangle$ is periodically focusing. Linear densities obtained from predictions of analytical theory (Eq. 2.71) (a,c) and GPE simulations (b,d) are compared at $t = T_{\mathrm{col}}/2$ (solid blue line). Red dashed line represents the total linear density of the BEC at $t = 0$, n_0 is the linear peak density of the BEC, blue dashed line is the linear density of the component $|2\rangle$ at $t = 0$. At large preparation angles ((a) $\theta = \pi/2$) the analytical model predicts $n_2 > n$; however the GPE simulations (b) show that $n_2 \leq n$. At $\theta \ll \pi/2$ the effective single-component theory (c) agrees well with the coupled GPE simulations(d).

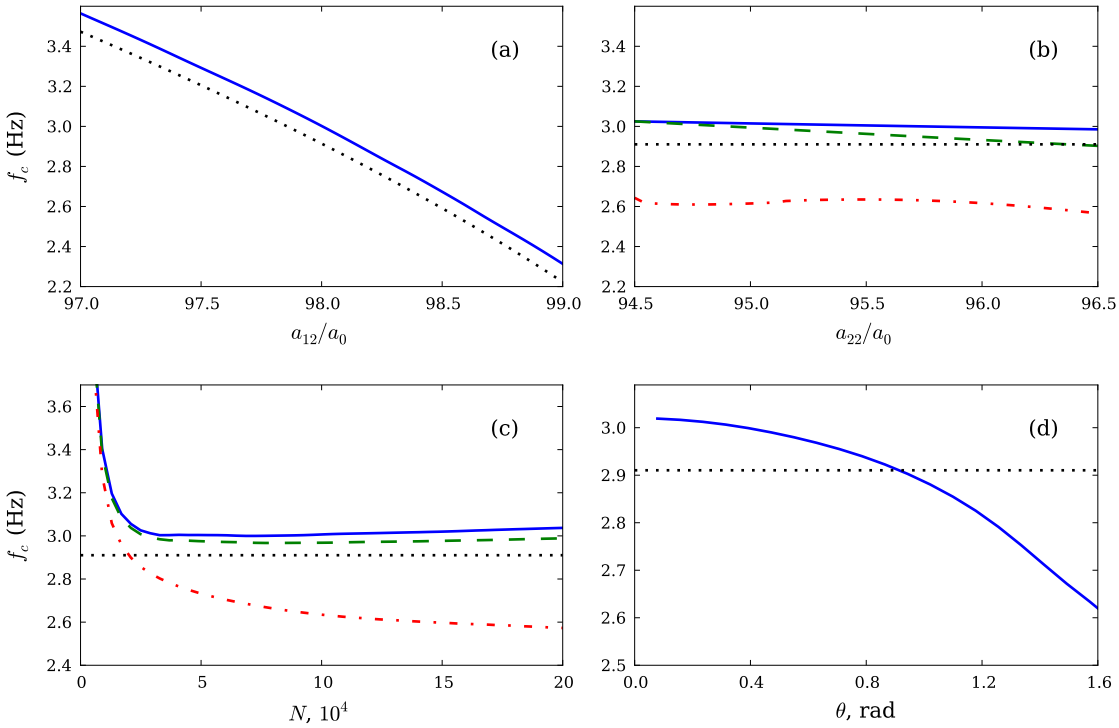

Figure 6.3: Dependence of the frequency of collective oscillations of component $|2\rangle$ on the scattering lengths a_{12} (a), and a_{22} (b), on the total atom number N (c) and the preparation pulse area θ (d). Dotted lines are the analytical predictions of Eq. 2.66. Three-dimensional GPE simulations are represented by solid lines ($\theta = \pi/10$), dashed lines ($\theta = \pi/5$) and dash-dotted lines ($\theta = \pi/2$). $N = 10^5$ for (a), (b) and (d).

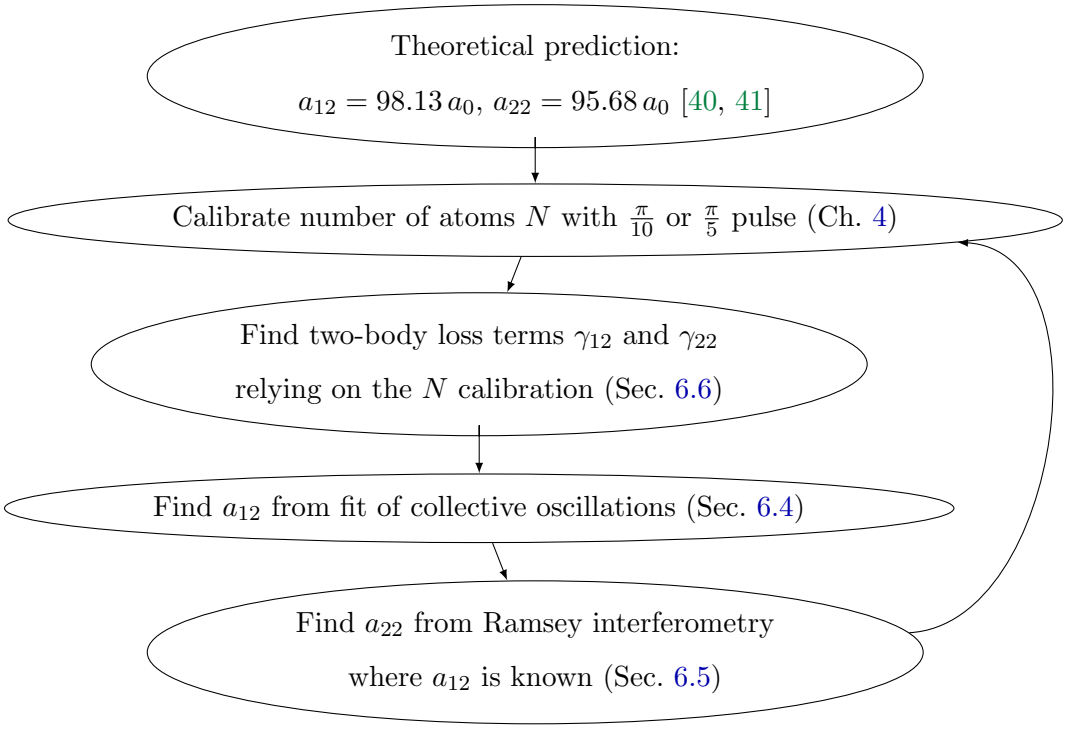

Figure 6.4: Converging sequence of data processing to evaluate the s-wave scattering lengths. The atom number calibration depends on a_{12}, and the evaluated value of a_{22} depends on the atom number calibration and the two-body loss terms. In order to ensure the convergence, we cycle through the fitting yielding those parameters until they stop changing. Notably, a_{12} stays almost unchanged during this process confirming that it is almost decoupled from other parameters.

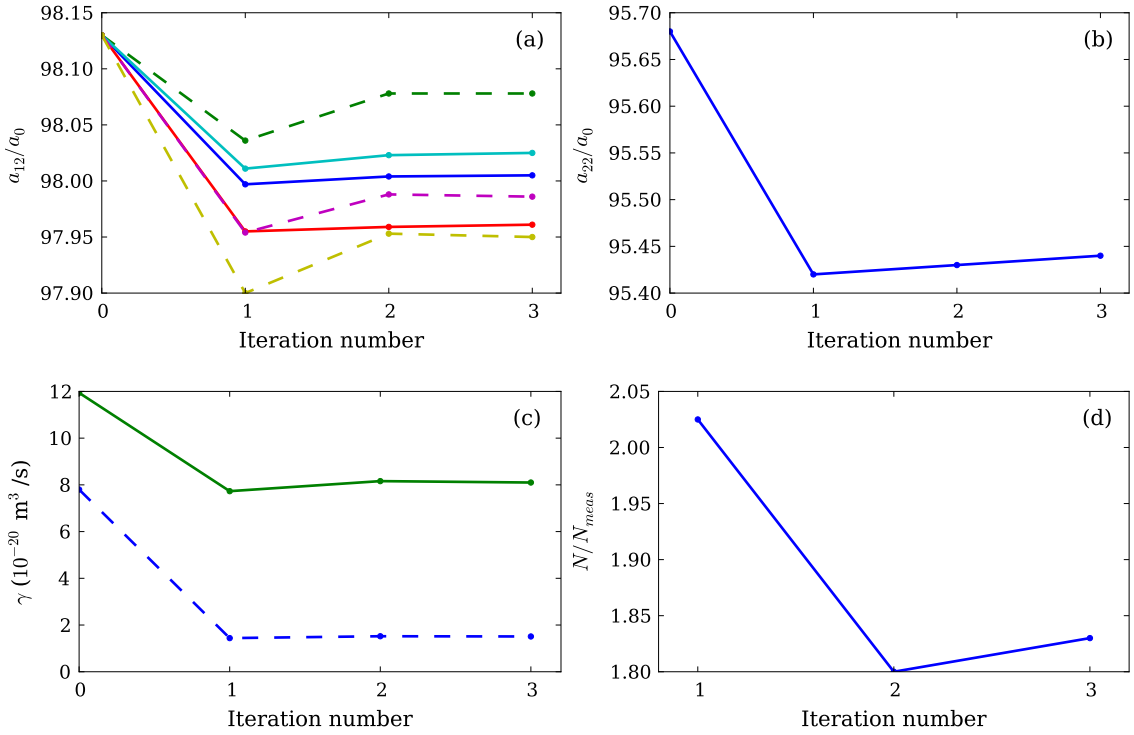

Figure 6.5: Iterative convergence of values of the interspecies scattering length a_{12} in six independent measurements (a), the intraspecies scattering length a_{22} (b), the two-body loss coefficients γ_{22} (solid line) and γ_{12} (dashed line) (c) and the interferometric atom number calibration (d).

$\pi/10$ and $\pi/2$ preparation pulses. At the end of the first iteration we find new values of N, γ_{12}, γ_{22}, a_{12} and a_{22} and cycle through the same sequence of analysis several times until all values converge. We find that 3 iterations are enough for convergence (Fig. 6.5).

6.4 Interspecies scattering length measurement

For measurements of the s-wave scattering length a_{12} characterizing the inter-state interactions of ^{87}Rb atoms, we prepare a BEC in state $|1\rangle$, apply a $\pi/10$ or $\pi/5$ pulse to produce a two-component BEC with the populations $N_2 \ll N$. After holding for a variable time t, the BEC is released from the trap and a single absorption image of both

components is taken after $t_{\mathrm{drop}} = 6.6$ ms or 20.1 ms of free expansion. The axial width of component $|2\rangle$ is measured at different evolution times t by performing 2D Gaussian fits of the density profiles (Fig. 6.6) from the absorption images and plotting against the evolution time t (Fig. 6.7, Fig. 6.9). The choice of Gaussian fitting functions originates from the fact that component $|2\rangle$ has a Gaussian shape when the two-component BEC is in its ground (equilibrium) state and $n_2 \ll n$ (follows from Eq. 2.61). Indeed, 2D Gaussian functions fit the experimentally obtained density profiles well at all times and can provide a good measure of the BEC width (Fig. 6.6). This measurement was made for different numbers of atoms ($6.9 \times 10^4 \leq N \leq 1.4 \times 10^5$), different preparation pulse areas θ and different drop times t_{drop} in order to check that systematic errors do not contribute. The measurement results were fitted with the widths of density profiles obtained in a similar way from numerical simulations of coupled Gross-Pitaevskii equations (Eq. 2.3) and integrated along one of the dimensions. The full 3D simulations were performed using a split-step Fourier method [113] on a $128 \times 32 \times 32$ Cartesian grid. The simulator of the BEC dynamics was developed by Bogdan Opanchuk [114].

It is crucial to simulate the BEC free expansion during the drop time t_{drop}. After the BEC is released from the trap, the mean-field interactions quickly become small and momenta of different parts of the BEC remain almost unchanged. Thus, the BEC components continue focusing (or defocusing) during the free fall, i.e., the width of the state $|2\rangle$ BEC reaches its minimum at a shorter evolution time (Fig. 6.8). This could lead to an under-estimation of the period of the collective oscillations T_{col} and an under-estimation of the measured a_{12}. We have simulated the BEC free expansion using the same split-step method but at a different grid size ($128 \times 256 \times 256$) to ensure that the whole cloud fits in the grid. Alternatively, we could introduce an additional time shift of the dynamics and keep it as a free parameter as long as only the period of the dynamics matters; however this approach is less precise.

We developed a method of absolute atom number calibration which depends on the scattering lengths (Section 4.2). If a two-component BEC used in this method is prepared with a short pulse (e.g., $\theta = \pi/10$), the dependence of the obtained calibration coefficient

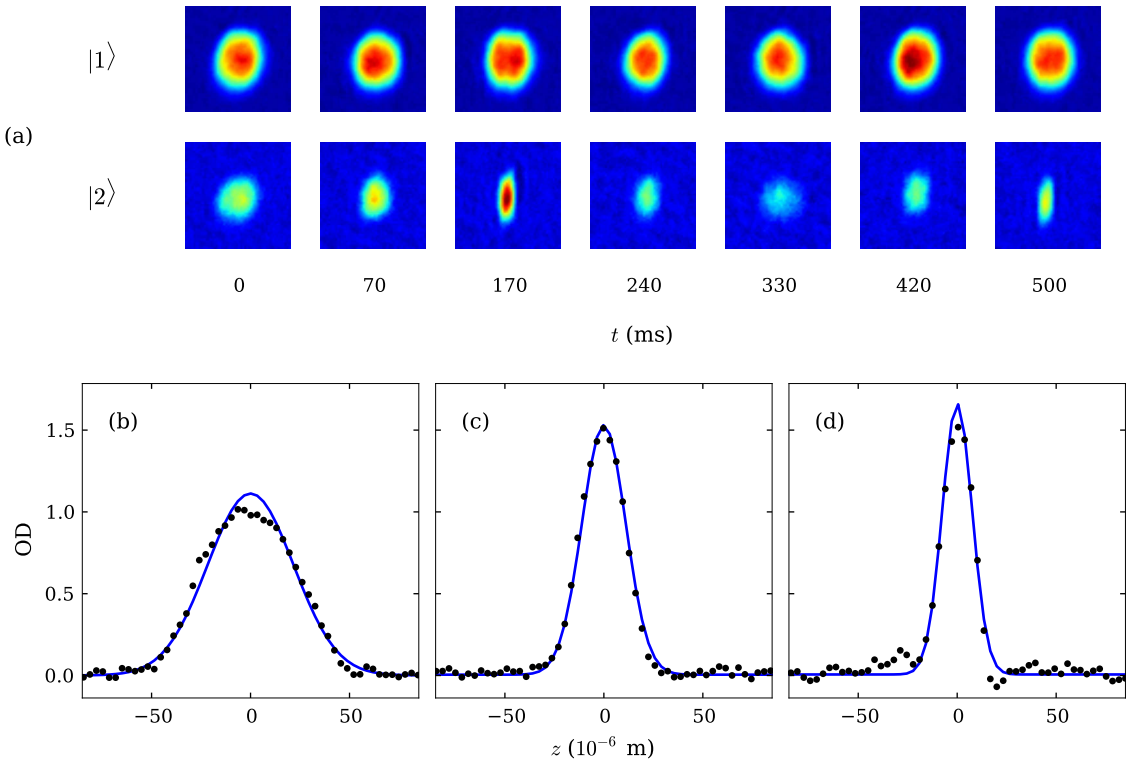

Figure 6.6: Temporal evolution of the two components of a BEC prepared by a $\pi/5$ pulse, $t_{\mathrm{drop}} = 20.1$ ms. The experimentally obtained absorption images (a) reveal that component $|2\rangle$ periodically focuses while component $|1\rangle$ remains almost unchanged when $n_2 \ll n$. The cross-sections of the single shot absorption images of component $|2\rangle$ taken at different evolution times (0 ms (b), 100 ms (c) and 170 ms (d)) show that the experimental data (black points) are well fitted with 2D Gaussian functions (blue solid lines are cuts of 2D Gaussian fits).

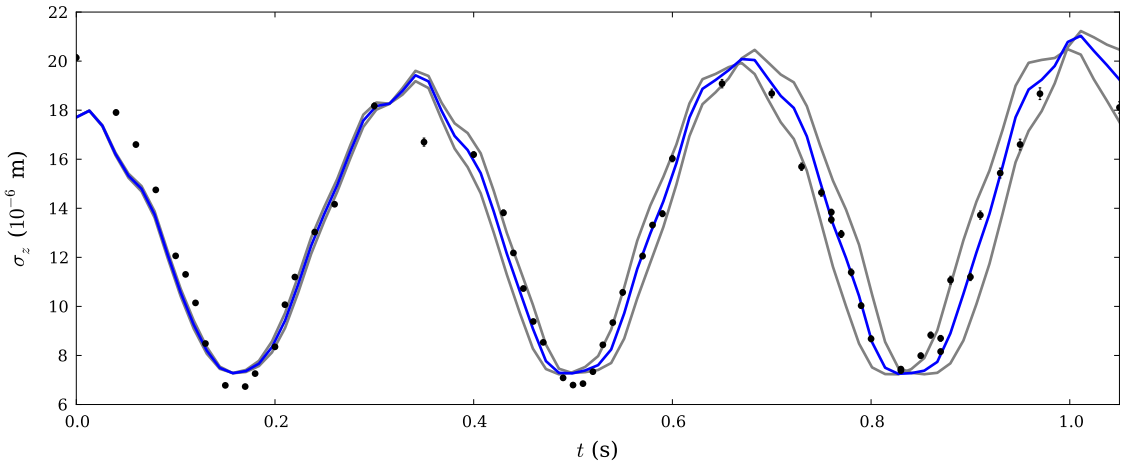

Figure 6.7: Comparison of the experimental data (Fig. 6.9f) with the simulations performed for optimal a_{12} (solid blue) and changed by $\pm 0.1 a_0$ (grey lines). The statistical uncertainty of the fit is $0.015\, a_0$.

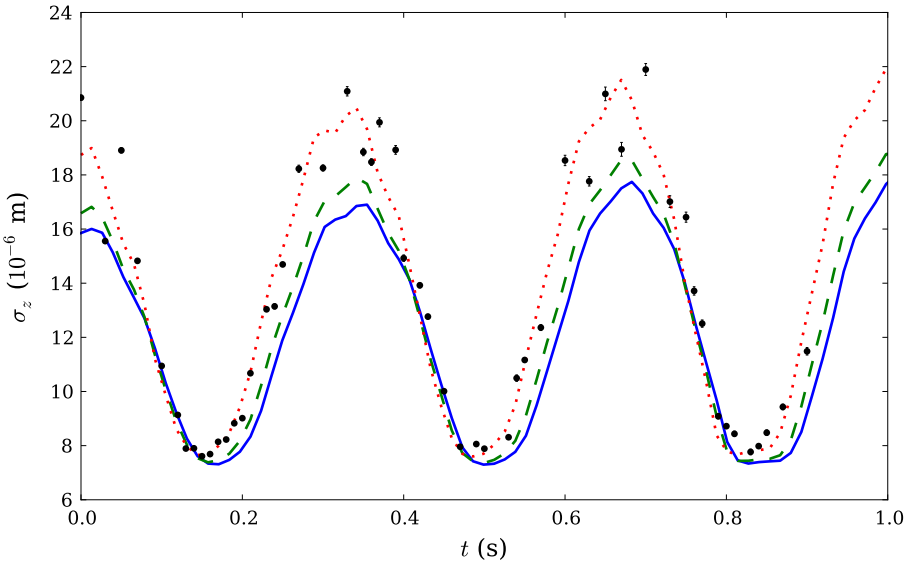

Figure 6.8: Width of component $|2\rangle$ calculated for different free expansion times. Black dots are experimental points taken for a 20.1 ms free expansion time. The results of CGPE simulations without free expansion (solid line), with 6.6 ms of free expansion (dashed line) and with 20.1 ms of free expansion (dotted line) are presented. It is clear that the cloud continues its focusing dynamics during the free expansion time.

$k = N/N_{\mathrm{meas}}$ is sensitive to the difference $(a_{11} - a_{12})$ and is almost insensitive to a_{22} (the residual small dependence can be included in the systematic uncertainty until a_{22} is known). After the value at a_{12} is obtained, we change accordingly the calibration coefficient in the simulations. This uncertainty in the total number of atoms does not influence the outcomes because changing the number of atoms by factor of 2 results in a variation of the simulated a_{12} value by less than $0.03a_0$ for the measurements performed with a $\pi/10$ preparation pulse. As such, at the second iteration the values of a_{12} and atom number calibration coefficient k can be considered to have converged to the actual values.

We perform 6 sets of experiments: with $\pi/10$-pulses and $\pi/5$-pulses (Fig. 6.9). Systematic errors are calculated for each set of measurements assuming a 10% error in the preparation pulse area θ (defined by the MW switch) and a 15% error in the total number of atoms N obtained from the preparation of the BEC. The error in a_{22} is calculated further on. The error in a_{12} consists of the systematics calculated from the slopes of the corresponding dependences (Fig. 6.3):

$$\delta a_{12} = \left(\frac{\partial f_c}{\partial a_{12}}\right)^{-1} \left(0.10\,\theta\frac{\partial f_c}{\partial \theta} + 0.15\,N\frac{\partial f_c}{\partial N} + \delta a_{22}\frac{\partial f_c}{\partial a_{22}}\right) + \delta_{\mathrm{st}} a_{12}, \tag{6.3}$$

where $\delta_{\mathrm{st}} a_{12}$ stands for the statistical uncertainty of the a_{12} measurement. The final value of a_{12} was calculated as a weighted mean of all the individual results, where the weight coefficients are obtained from the errors of the individual measurements (Table 6.1). The inclusion of quantum noise in the analysis [29] and accounting for finite temperature effects and trap anharmonicities is a subject of further theoretical and experimental studies.

6.5 Intraspecies scattering length measurement

We measure the value of the s-wave scattering length a_{22} characterizing the interactions of atoms in state $|2\rangle$ using Ramsey interferometry and the obtained value of $a_{12} = 98.006\,a_0$. We employ two Ramsey sequences with superpositions created by $\pi/10$ (sequence I) and $\pi/2$ (sequence II) pulses, in such a way that the experimental runs are intermixed in time. This ensures that the interference data are taken at the same value of the two-photon detuning and the total number of atoms for both sequences. According to

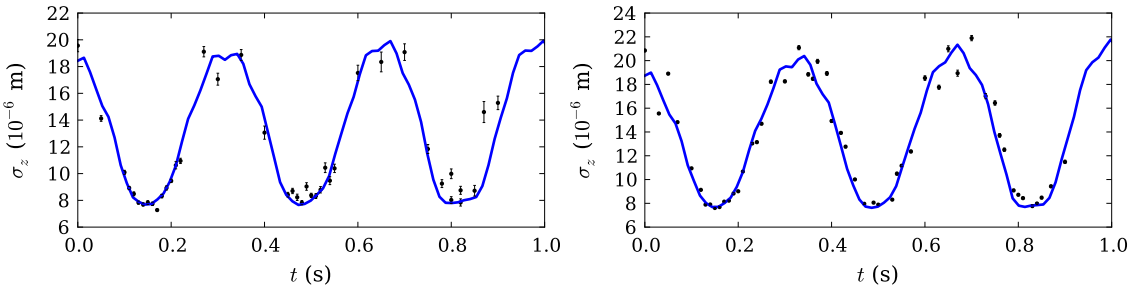

(a) $\theta = \pi/10$, $N = 6.9 \times 10^4$, $t_{\text{drop}} = 20.1$ ms

(b) $\theta = \pi/5$, $N = 7.6 \times 10^4$, $t_{\text{drop}} = 20.1$ ms

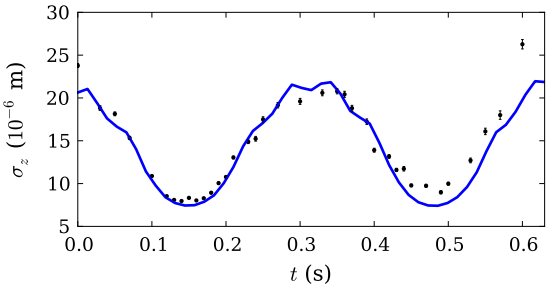

(c) $\theta = \pi/10$, $N = 1.3 \times 10^5$, $t_{\text{drop}} = 20.1$ ms

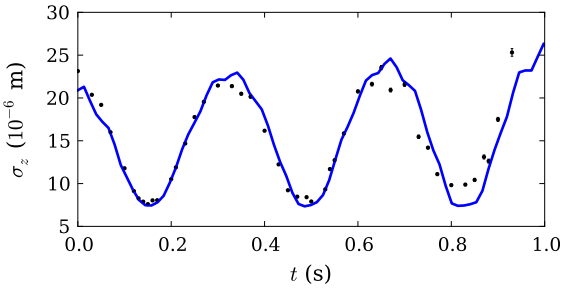

(d) $\theta = \pi/5$, $N = 1.4 \times 10^5$, $t_{\text{drop}} = 20.1$ ms

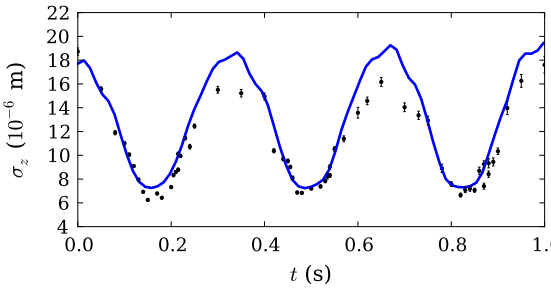

(e) $\theta = \pi/10$, $N = 1.1 \times 10^5$, $t_{\text{drop}} = 6.6$ ms

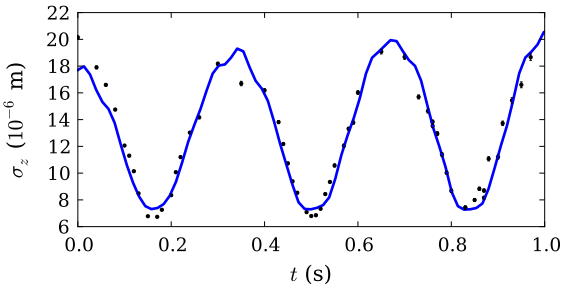

(f) $\theta = \pi/5$, $N = 1.1 \times 10^5$, $t_{\text{drop}} = 6.6$ ms

Figure 6.9: Time evolutions of the width of the 2D Gaussian fits to state $|2\rangle$ measured along the axial orientation of a cigar-shaped trap in a two-component BEC prepared by $\theta = \pi/5$ or $\theta = \pi/10$ pulses. Experiments are carried out with different numbers of atoms and different drop times. Results of the GPE simulations are depicted by a blue line, values obtained from the experiment are the black points. Error bars represent uncertainties of the fits. Optical resolution is set as 6.5 microns. Solid line plots represent the results of simulations performed with $a_{12} = 98.006\, a_0$.

$\frac{a_{12}}{a_0}$	$\frac{\partial f_c}{\partial N}$, Hz	$\frac{\partial f_c}{\partial \theta}$, $\frac{\text{Hz}}{\text{rad}}$	$\frac{\partial f_c}{\partial a_{22}}$, $\frac{\text{Hz}}{a_0}$	$\frac{\partial f_c}{\partial a_{12}}$, $\frac{\text{Hz}}{a_0}$	$\frac{\delta a_{12}}{a_0}$
98.005	1.39×10^{-7}	0.084	0.020	0.63	0.037
98.078	1.57×10^{-7}	0.148	0.062	0.63	0.042
97.961	2.8×10^{-7}	0.084	0.020	0.63	0.046
97.950	2.1×10^{-7}	0.148	0.062	0.63	0.050
98.025	2.8×10^{-7}	0.084	0.020	0.63	0.033
97.986	2.1×10^{-7}	0.148	0.062	0.63	0.042
Weighted mean: $a_{12} = (98.006 \pm 0.016)\, a_0$					

Table 6.1: Final set of results for all a_{12} measurements with all sources of uncertainties. The derivatives of the collective oscillations frequencies are calculated using Eq. 6.3 in order to calculate the uncertainties in each a_{12} measurement.

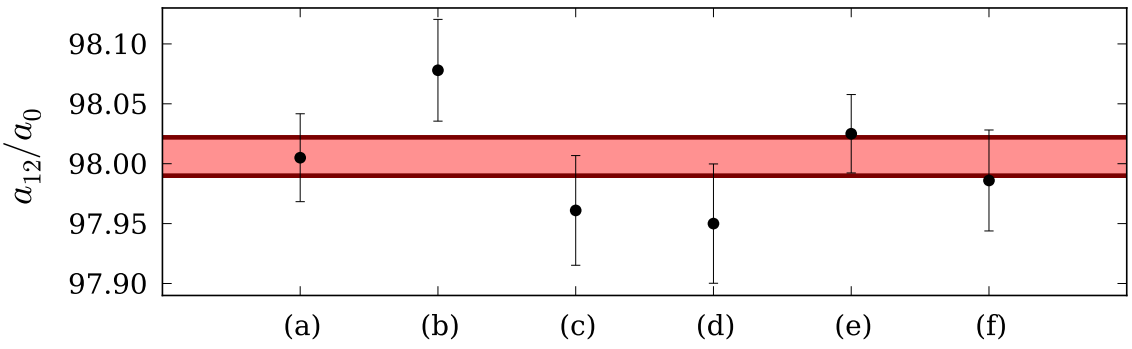

Figure 6.10: Values of intraspecies scattering length a_{12} obtained in different experimental runs, where the labels (a)-(f) are the same as in Fig. Fig. 6.9. Error bars are obtained assuming a 10% two-photon Rabi frequency uncertainty and a 15% total number of atoms uncertainty. Red filled region shows the value of the scattering length and the uncertainty given by the weighted average, $a_{12} = 98.006(16)\, a_0$.

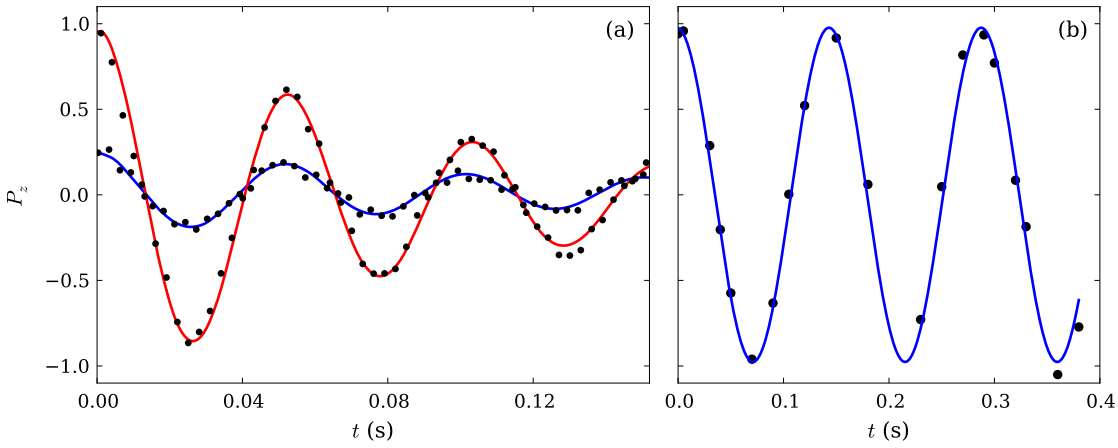

Figure 6.11: (a) Time evolution of the normalized number difference P_z in two Ramsey sequences with $\pi/10$ (sequence I) and $\pi/2$ (sequence II) pulses. Blue and red lines show GPE fits of the data points (black) obtained in sequences I and II, respectively. From the sequence I we find the total number of atoms relying on the measured scattering length a_{12}. From the sequence II we find the value of $a_{22} = 95.44(7)\, a_0$. Major contributions to the systematic uncertainty are an $0.016\, a_0$ error in the value of a_{12} and a 10% error in the preparation pulse area θ. The two-photon detuning is measured with non-condensed atoms (b).

Eq. 2.23, the collisional shifts for the two fringes are approximately $f_1 \propto 2(a_{11} - a_{12})$ and $f_2 \propto (a_{11} - a_{22})$. The normalized difference of the two measured shifts $(f_1 - f_2)/f_1$ should be almost independent of the total number of atoms. In order to find a_{22}, we firstly find the total number of atoms N by fitting the data in the sequence I with the GPE simulated fringe using the known value of a_{12} and, secondly, by fitting the fringe in the sequence II with the simulations using N and keeping a_{22} as a free parameter (Fig. 6.11a). In order to find the two-photon detuning for the GPE simulations, we measured the Ramsey fringe frequency with 1.9×10^4 non-condensed atoms immediately after the measurement of the two fringes with the BEC (Fig. 6.11b).

The major source of uncertainty comes from the a_{12} measurement. According to Eq. 2.23, $\delta a_{22} = 2\delta a_{12} = 0.03 a_0$. Another contributor to the uncertainty is the precision

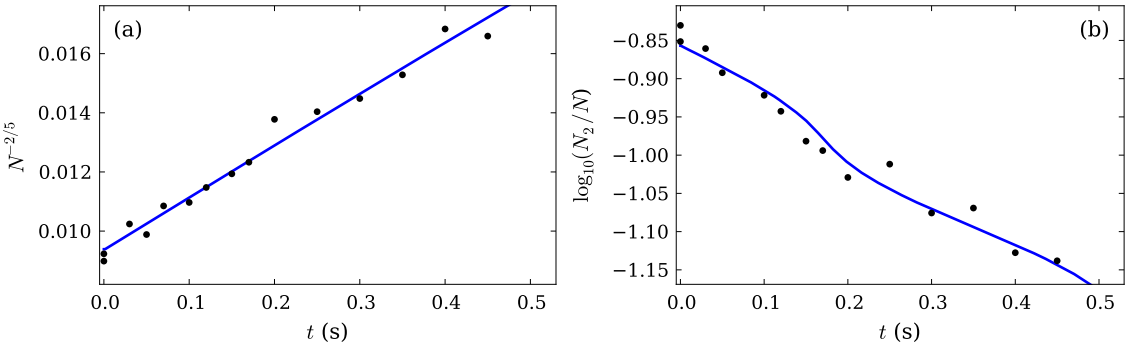

Figure 6.12: Measurement of two-body intraspecies loss rate γ_{22} (a) and interspecies loss rate γ_{12} (b). Black dots are experimental points, solid lines are the results of GPE simulations. The fitted values are $\gamma_{22} = 8.1(3)\times10^{-14}$ cm^3/s, $\gamma_{12} = 1.51(18)\times10^{-14}$ cm^3/s.

of setting the $\pi/2$ pulse (10% error in θ corresponds to $\delta a_{22} = 0.03a_0$). The statistical error is $0.013\,a_0$, and other sources of error, such as uncertainties in the loss terms γ_{ij}, proved to be less than $0.01a_0$. Overall, we state the result of this measurement (after the convergence of all the parameters): $a_{22} = (95.44 \pm 0.07)\,a_0$.

6.6 Two-body loss coefficients

The process of atom loss in a two-component cloud is described by the equations

$$\begin{aligned} \frac{dn_1}{dt} &= -\gamma_{111} n_1^3 - \gamma_{12} n_1 n_2, \\ \frac{dn_2}{dt} &= -\gamma_{22} n_2^2 - \gamma_{12} n_1 n_2, \end{aligned} \tag{6.4}$$

where n_1 and n_2 are the densities of each BEC component; γ_{12} and γ_{22} are two-body loss coefficients, involving inelastic collisions of two atoms in states $|1\rangle$ and $|2\rangle$ and two atoms in state $|2\rangle$, respectively; and γ_{111} is the three-body loss coefficient. The influence of three-body losses in state $|2\rangle$ is negligible compared to two-body losses.

The two-body decay for atoms in state $|2\rangle$ occurs due to spin flips of both colliding atoms:

$$|2\rangle + |2\rangle \rightarrow |F = 2, m_F = 0\rangle + |F = 2, m_F = +2\rangle + 2E_{\text{col}}, \tag{6.5}$$

where the energy per atom $E_{\mathrm{col}} = h \times 748$ Hz released in the collision can be calculated as half the difference between the initial and final Zeeman energies determined using the Breit-Rabi formula (Eq. 3.19). Atoms which change their spin state to $|F = 2, m_F = 0\rangle$ are lost from the magnetic trap. Atoms in state $|F = 2, m_F = +2\rangle$ form a cloud with a non-zero temperature defined by E_{col} and are separated by a Stern-Gerlach force in the dual-state imaging process.

In order to measure γ_{22} we prepare a BEC in state $|1\rangle$ and transfer all of its population to state $|2\rangle$ with a π-pulse. The loss equation then reduces to $dn_2/dt = -\gamma_{22} n_2^2$. This can be solved analytically when the loss rate is less than the lowest frequency of the trap. If this condition is satisfied, the cloud adiabatically follows a Thomas-Fermi profile. Substituting the TF profile for n_2, we obtain for a parabolic trap with a geometrical mean trap frequency $\bar{f}$

$$\frac{dN_2}{dt} = -\frac{(2\pi)^{1/5} 15^{2/5}}{7 a_{22}^{3/5}} \left(\frac{m\bar{f}}{\hbar}\right)^{\frac{6}{5}} \gamma_{22} N^{\frac{7}{5}}. \tag{6.6}$$

The solution is

$$N_2(t)^{-\frac{2}{5}} = N_2(0)^{-\frac{2}{5}} + \left[\frac{2}{5} \frac{(2\pi)^{1/5} 15^{2/5}}{7 a_{22}^{3/5}} \left(\frac{m\bar{f}}{\hbar}\right)^{\frac{6}{5}} \gamma_{22}\right] t. \tag{6.7}$$

It is convenient then to plot a graph of $N_2^{-2/5}$ vs t with γ_{22} given by its slope. As long as the loss rate $N_2^{-1}\, dN_2/dt$ is still comparable with the axial trap frequency, the condensate does not adiabatically follow the trapping potential during the loss process leading to a slight deviation from Eq. 6.7. Due to this reason we fit the experimental data with GPE simulations. The resulting loss coefficient is $\gamma_{22} = 8.1(3) \times 10^{-14}$ cm^3/s (Fig. 6.12a). The loss coefficient γ_{22} was also reported in other papers [19, 43].

The interspecies loss coefficient γ_{12} is obtained by fitting a decay of the population N_2 in a mixture of two BEC components ($N_2 \ll N$) with GPE simulation results. In such a configuration, $n_2^2 \ll n_1 n_2$ and the fitted value of γ_{12} has only a very small dependence on γ_{22}, even though we use its value in our GPE simulations. The obtained loss coefficient is $\gamma_{12} = 1.51(18) \times 10^{-14}$ cm^3/s (Fig. 6.12b). Two-body loss coefficients can be converted to an imaginary part of the scattering lengths by $\mathrm{Im}(a_{ij}) = \gamma_{ij} m/4h$. The value of γ_{12} corresponds to $\mathrm{Im}\, a_{12} = 0.016\, a_0$, in agreement with the theoretical investigations [35].

6.7 Sensitivity to drifts of fundamental constants

According to grand unification models [115], $\delta\beta/\beta \sim 35\delta\alpha/\alpha$, where α is the fine structure constant and $\beta = m_e/m_p$ is the electron to proton mass ratio. Chin and Flambaum suggest [45] that an s-wave scattering length a measured far from Feshbach resonances is sensitive to drifts in β:

$$\frac{\delta a}{a} = \frac{N_v \pi}{2} \frac{(a-\bar{a})^2 + \bar{a}^2}{a\bar{a}} \frac{\delta\beta}{\beta} = K \frac{\delta\beta}{\beta}, \tag{6.8}$$

where N_v is the number of vibrational bound states (e.g., number of nodes of the atomic wavefunction in a molecular van der Waals potential), the mean scattering length $\bar{a} = c(2\mu C_6/\hbar^2)^{1/4}$, whose $c \approx 0.47799$, $\mu = m/2$ is reduced mass of two interacting atoms, and C_6 is the van der Waals molecular potential parameter.

Two colliding atoms in the states of interest here ($|1\rangle \equiv |F=1, m_F=-1\rangle$ and $|2\rangle \equiv |F=2, m_F=1\rangle$ in ^{87}Rb) form a singlet molecular state which has $N_v = 125$ [35, 40]. The reported value of the van der Waals coefficient $C_6 = 4.703(9) \times 10^3$ a.u. $= 2.251(4) \times 10^{-76}$ J $\times$ m^6 [35, 40] gives $\bar{a} = 66.4\, a_0$ resulting in an enhancement factor of $K = 163$. This yields for our precision of measurement $\delta a_{12}/a_{12} = 1.6 \times 10^{-4}$ and an estimated relative sensitivity to the variations in the proton to electron mass ratio of $\delta\beta/\beta = 9.8 \times 10^{-7}$. This value is comparable with the sensitivity $\delta\beta/\beta = 1.5 \times 10^{-6}$ to drifts in β obtained in a quantum scattering interferometer [116]. The use of optically induced Feshbach resonances as suggested in [45], can increase the enhancement factor to $K \sim 10^{12}$ and test β with a relative sensitivity of $\delta\beta/\beta \sim 10^{-16}$. Alternatively, narrow RF-induced Feshbach resonances probably can be used for such measurements (Ch. 7), where the enhancement factors for these can be calculated using the data provided in [38]. The latter can be studied in further investigations.

6.8 Conclusion

A new method for precise measurement of the interspecies scattering length is developed: the error in the number of atoms, the intraspecies scattering length and imperfect mixture

	a_{11}/a_0	a_{12}/a_0	a_{22}/a_0
[21]	100.44	98.09	95.47
[19]	100.4	97.66	95.0
[40]	100.40(10)	98.13(10)	95.68(10)
Our work	100.4	98.006(16)	95.44(7)

Table 6.2: Our scattering lengths measurements compared with previous works

preparation contribute negligibly to the uncertainty of a_{12}. We have measured the inter- and intraspecies scattering lengths and inelastic loss terms at the bias magnetic field of 3.23 G for atoms in a two-component BEC of ^{87}Rb composed of states $|1\rangle \equiv |1,-1\rangle$ and $|2\rangle \equiv |2,+1\rangle$. The final values for the scattering lengths are $a_{12} = 98.006(16)a_0$, $a_{22} = 95.44(7)a_0$, while the value $a_{11} = 100.40a_0$ is fixed and assumed to be error-free. A comparison with previous measurements is presented in Table 6.2. The inelastic loss coefficients obtained are $\gamma_{12} = 1.51(18) \times 10^{-14}\text{cm}^3/\text{s}$, $\gamma_{22} = 8.1(3) \times 10^{-14}$ cm^3/s. The uncertainties of the measurements can be reduced by improving the precision of the BEC preparation, the stability of the microwave setup (the dominant contribution is from the MW switch) and the optical resolution of the imaging system.

Chapter 7

RF-induced Feshbach resonances

The tuning of s-wave scattering lengths in a BEC is required in such applications as spin-squeezing [48] and collisional quantum logic gates [117] and Feshbach resonances are the key tool for tuning collisional interactions. Sometimes the bound state energy cannot be equal to the energy of the incoming channel, and a conventional Feshbach resonance does not exist even when a low-energy bound state exists. In this case, the resonance can be reached by radio-frequency or microwave dressing of the atomic states [58, 57]. RF-dressed Feshbach resonances have previously been observed in the vicinity of a conventional, magnetically tunable Feshbach resonance; however the resonances which cannot be reached by changing bias magnetic fields have not yet been observed. Tunable interactions for the states $|1\rangle \equiv |1,-1\rangle$ and $|2\rangle \equiv |2,+1\rangle$ in ^{87}Rb are of particular interest. Being differentially magnetic field insensitive, the coherent superposition of these states provides long coherence times in trapped non-condensed ensembles [27] and BECs [31]. As such, the possibility to have an accessible way of tuning interspecies scattering lengths is extremely useful for quantum metrology [48] and quantum information processing proposals [117]. It is convenient to use an atom chip for addressing RF-induced Feshbach resonances since the atomic samples are extremely close to the current-carrying wires which can facilitate RF fields with high amplitude.

We detect previously unobserved RF-induced Feshbach resonances for the states $|1\rangle$ and $|2\rangle$ in ^{87}Rb. RF coupling of the incoming channel with the bound states increases

the imaginary part of the scattering length a_{12} and hence the two-body collisional loss coefficient γ_{12} resulting in faster atom number decay. Furthermore, we detect changes in the real part of the s-wave scattering length a_{12} using our previously developed technique (Ch. 6) for its precise measurements. Apart from showing a new possibility of tuning the interspecies scattering length a_{12}, our results provide new information for atomic scattering theory [35, 40].

7.1 Weakly bound states and Feshbach resonances

Following the paper [59], we label molecular bound states in terms of pure Zeeman states $|F, m_F\rangle$ (a-h) which define the molecular state (Fig. 7.1). We label the projection of the total angular momentum by $M_F = m_{F_1} + m_{F_2}$ while the total angular momentum is $\vec{F} = \vec{F}_1 + \vec{F}_2$, where 1 and 2 label the two atoms of the entrance channel or constituents of a weakly bound molecule. Our RF radiation is linearly polarized perpendicular to the quantization magnetic field of our cigar-shaped magnetic trap. In an s-wave collision of two atoms dressed with such RF radiation at nonzero quantization magnetic field, the single-photon selection rule for the projection of the total angular momentum is $\Delta M_F = \pm 1$. Having states $|1, -1\rangle \equiv |c\rangle$ and $|2, +1\rangle \equiv |g\rangle$ in the entrance channel, we can obtain the following molecular bound states using single-photon RF dipole transitions: $|A\rangle \equiv |ch\rangle$, $|B\rangle \equiv |bg\rangle$, $|C\rangle \equiv |cf\rangle$, $|D\rangle \equiv |be\rangle$, $|E\rangle \equiv |af\rangle$, $|F\rangle \equiv |ad\rangle$ (Fig. 7.2). The existence of RF-induced Feshbach resonances is predicted for these levels [58] (Fig. 7.3). When the RF coupling is applied, the resonances are blue-shifted for resonance A and red-shifted for resonances B-F, where the radiation shift is roughly proportional to B_0^2.

7.2 Detection of resonances with inelastic losses

In the experiment, we detect and characterize resonances A, B and C. In the resonances, the imaginary part of the s-wave scattering length has a Lorentzian shape [58]:

$$b \equiv \mathrm{Im}(a_{12}) = b_{\mathrm{bg}} + \frac{1}{k_i} \frac{\frac{1}{4}\gamma_{ib}\gamma_{ba}}{\hbar^2 \left(\omega - \omega_0\right)^2 + \gamma_{ba}^2/4}, \tag{7.1}$$

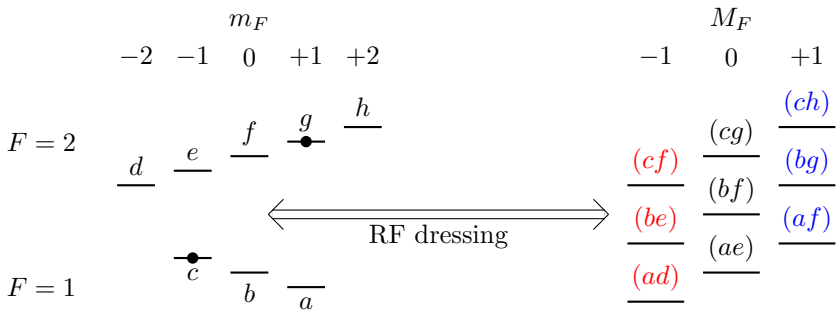

Figure 7.1: Molecular bound states (on the right side) are expressed in terms of constituent atomic states (a–h). We have states c and g in the incoming channel ($M_F = 0$), and therefore a single-photon transition can couple them only with $M_F = -1$ (red) and $M_F = +1$ (blue) molecular levels.

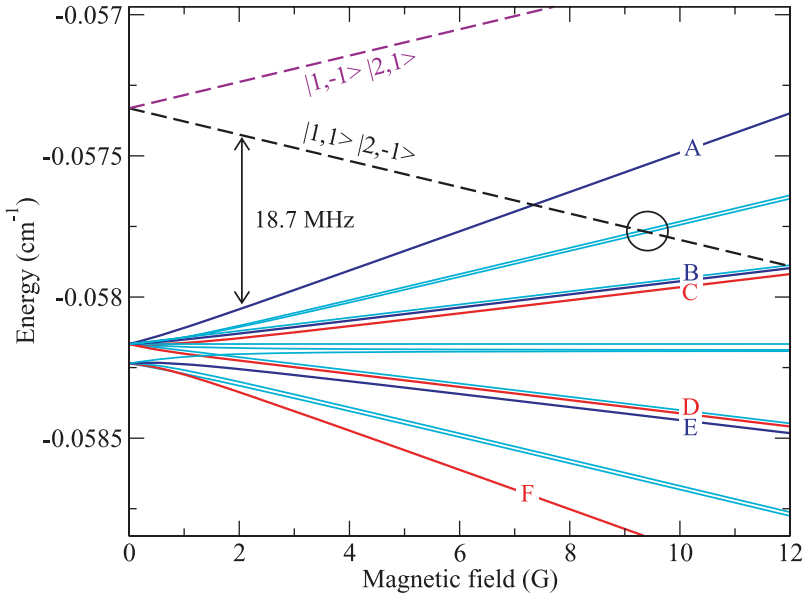

Figure 7.2: Adapted from Fig. 1 in [58]. Dependence of molecular bound state energies on the magnetic field. States labelled with letters A-F are those which can be coupled with the $|1,-1\rangle - |2,+1\rangle$ incoming channel by RF radiation. The blue circle stands for a magnetic Feshbach resonance for states $|1,+1\rangle - |2,-1\rangle$ at 9.1 G.

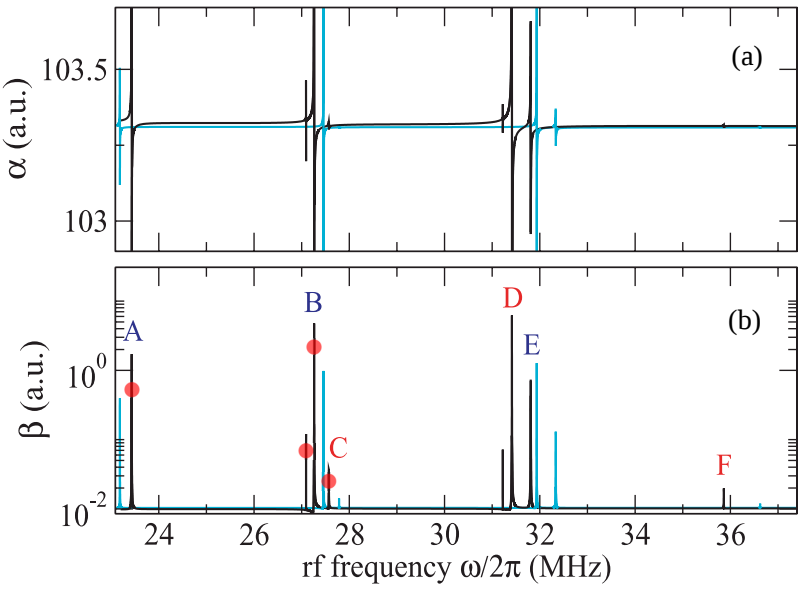

Figure 7.3: Adapted from Fig. 2 in [58]. Real (α) and imaginary(β) parts of the scattering length in the vicinity of RF-induced Feshbach resonances for a bias magnetic field $B = 3.23$ G [58]. The RF field amplitude is 4 G (light blue lines) and 10 G (light black lines). It is clearly visible that apart from the single-photon resonances, A-F, some "prohibited" resonances appear at high RF field amplitudes. We detected four resonances (marked by red circles): A, B, C and one not labelled in the original paper [58].

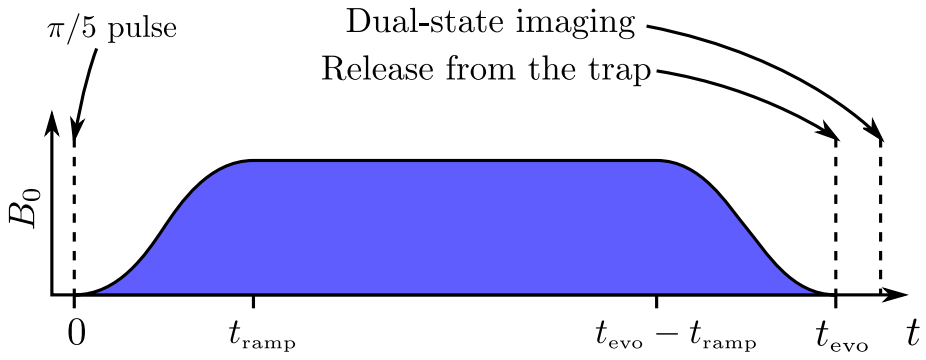

Figure 7.4: Experimental sequence for exciting RF-induced Feshbach resonances. A two-component BEC is prepared by a $\pi/5$ pulse. RF dressing is gradually switched on during a time $t_{\mathrm{ramp}} = 70$ ms, then the two-component BEC evolves at the maximum RF amplitude B_0 during the time $t_{\mathrm{evo}} - 2t_{\mathrm{ramp}}$, and after that the RF amplitude is gradually decreased during t_{ramp}. After this evolution during the time t_{evo}, the BEC is released from the trap and the two components undergo a dual-state imaging process.

where ω is the RF dressing frequency, ω_0 is the centre frequency of the resonance, k_i is the wave vector of the incident channel, b_{bg} is the background values of the imaginary part of the scattering length, γ_{ib} is the matrix element describing interactions of two atoms with an RF field, and γ_{ba} is the matrix element of a spin-dependent interaction potential between the atoms. The value of γ_{ba} is proportional to the interspecies loss rate

$$\gamma_{12} = \frac{4ha_0}{m}\,\mathrm{Im}(a_{12}). \tag{7.2}$$

The two-body loss rate is proportional to the imaginary part of the scattering length b and has a Lorentzian shape with a width at half-maximum $\gamma_{ba}/(\hbar)$ in the frequency domain. The maximum change in b is equal to $\gamma_{ib}/(k_i\gamma_{ba})$. We determine the widths of the resonances $\gamma_{ba}/(2\pi\hbar)$ and their heights $\gamma_{ib}/(k_i\gamma_{ba}a_0)$ from the dependence on the RF magnetic field amplitude B_0 and report the results in the Table 7.1.

In order to detect inelastic two-body losses in the experiment, we prepare a coherent superposition of states $|1\rangle$ and $|2\rangle$ by a $\pi/5$ preparation pulse. This ensures that the total number of atoms in the BEC does not change very much during the evolution. The amplitude of the RF field was smoothly (sinusoidally) increased during the time

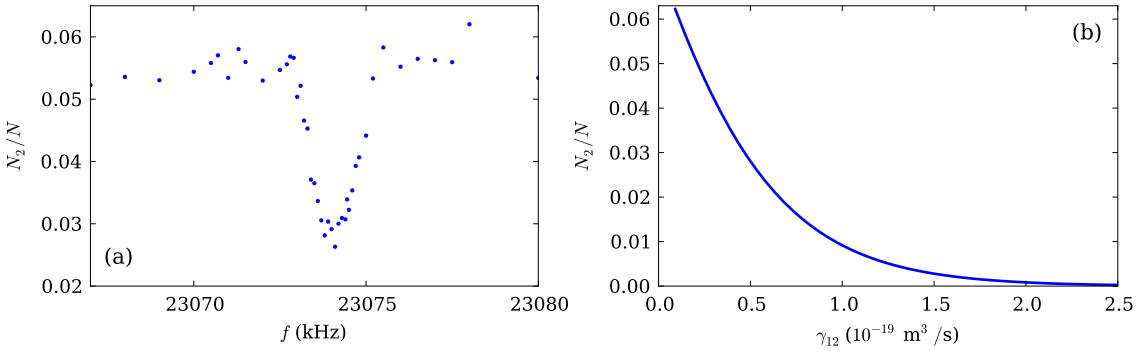

Figure 7.5: In the experiment, we obtain the dependence of N_2/N on the RF frequency (a) by measuring inelastic two-body losses in an RF-induced Feshbach resonance (the plot is obtained for $t_{\text{evo}} = 550$ ms). Using the coupled GPE (Eqs. 2.3) we calculate the fraction N_2/N after 550 ms of evolution time for different values of γ_{12} (b).

t_{ramp} (Fig. 7.4), then held at the maximum value B_0 for the duration $(t_{\text{evo}} - 2t_{\text{ramp}})$ and then smoothly decreased. A value of $t_{\text{ramp}} = 70$ ms is selected so that the RF dressing does not cause shaking of our magnetic trap. The total evolution time t_{evo} is 550 ms. After the release, component $|1\rangle$ is transferred to state $|F = 2, m_F = -1\rangle$ by MW adiabatic passage, and the two BEC components are spatially separated by a Stern-Gerlach force followed by a single absorption image of the two states [22]. The experimental images are processed with a fringe-removal algorithm (Sec. 3.3.5) [79].

For the measurements of the two-body loss coefficient γ_{12}, we detect the population of state $|2\rangle$ relative to the total number of atoms N_2/N (Fig. 7.5a). We perform simulations of the coupled Gross-Pitaevskii equations (Eq. 2.3) at different γ_{12} in order to obtain the dependence $N_2/N(\gamma_{12})$ for 550 ms of evolution and the experimentally measured initial total number of atoms $N = 1.2 \times 10^5$ (Fig. 7.5a). After 50 points of the calculation are obtained, we construct an inverse function $\gamma_{12,\text{th}}(N_2/N)$ interpolating points of the simulations with a cubic spline. The dependence $\gamma_{12,\text{th}}(N_2/N)$ is used to convert experimentally measured fraction N_2/N into the two-body loss coefficient γ_{12} (Fig. 7.6). In Fig. 7.6 we compare the results of our measurements with theoretical predictions provided by T. Tscherbul in private communication. Even though the value

B_0 (G)	γ_{ba} (kHz)	$\gamma_{ib}/(k_i\gamma_{ba}a_0)$
0.118	1.18(10)	0.0392(19)
0.229	3.8(4)	0.065(5)
0.445	4.0(5)	0.075(6)

(a) Resonance A: $f_0 = 23.07407(3)$ MHz

B_0 (G)	γ_{ba} (kHz)	$\gamma_{ib}/(k_i\gamma_{ba}a_0)$
0.118	2.0(4)	0.0205(13)
0.344	2.4(6)	0.075(11)

(b) $f_0 = 27.0448(3)$ MHz

B_0 (G)	γ_{ba} (kHz)	$\gamma_{ib}/(k_i\gamma_{ba}a_0)$
0.118	6.8(1.3)	0.022(2)
0.344	19(7)	0.041(7)

(c) Resonance B: $f_0 = 27.1715(4)$ MHz

B_0 (G)	γ_{ba} (kHz)	$\gamma_{ib}/(k_i\gamma_{ba}a_0)$
0.118	25(5)	0.0208(18)
0.344	9(2)	0.031(4)

(d) Resonance C: $f_0 = 27.4060(12)$ MHz

Table 7.1: Parameters of different RF-induced Feshbach resonances at different magnetic field amplitudes B_0. The resonance centre frequency f_0 stands for the resonance position at the minimum magnetic field amplitude B_0.

of RF magnetic field amplitude B_0 in the theoretical calculations was higher than we can produce in our experiment, the radiation shift due to that is just a small contribution to the unperturbed positions of the resonances.

7.3 Characterization of RF-induced Feshbach resonances with precision scattering length measurements

The real part of the interspecies s-wave scattering length a_{12} in the vicinity of a Feshbach resonance is expressed as [58]:

$$\alpha \equiv \mathrm{Re}(a_{12}) = \alpha_{\mathrm{bg}} - \frac{1}{k_i} \frac{\frac{1}{2}\gamma_{ib}\hbar\left(\omega - \omega_0\right)}{\hbar^2\left(\omega - \omega_0\right)^2 + \gamma_{ba}^2/4}, \tag{7.3}$$

where α_{bg} is the background value of the real part of the scattering length. The change in the real part of the scattering length $\delta\alpha = \alpha - \alpha_{\mathrm{bg}}$ is linked to the change in the imaginary part $\delta b = b - b_{\mathrm{bg}}$ by

$$\delta\alpha = -\delta b \frac{\omega - \omega_0}{\gamma_{ba}/\left(2\hbar\right)}. \tag{7.4}$$

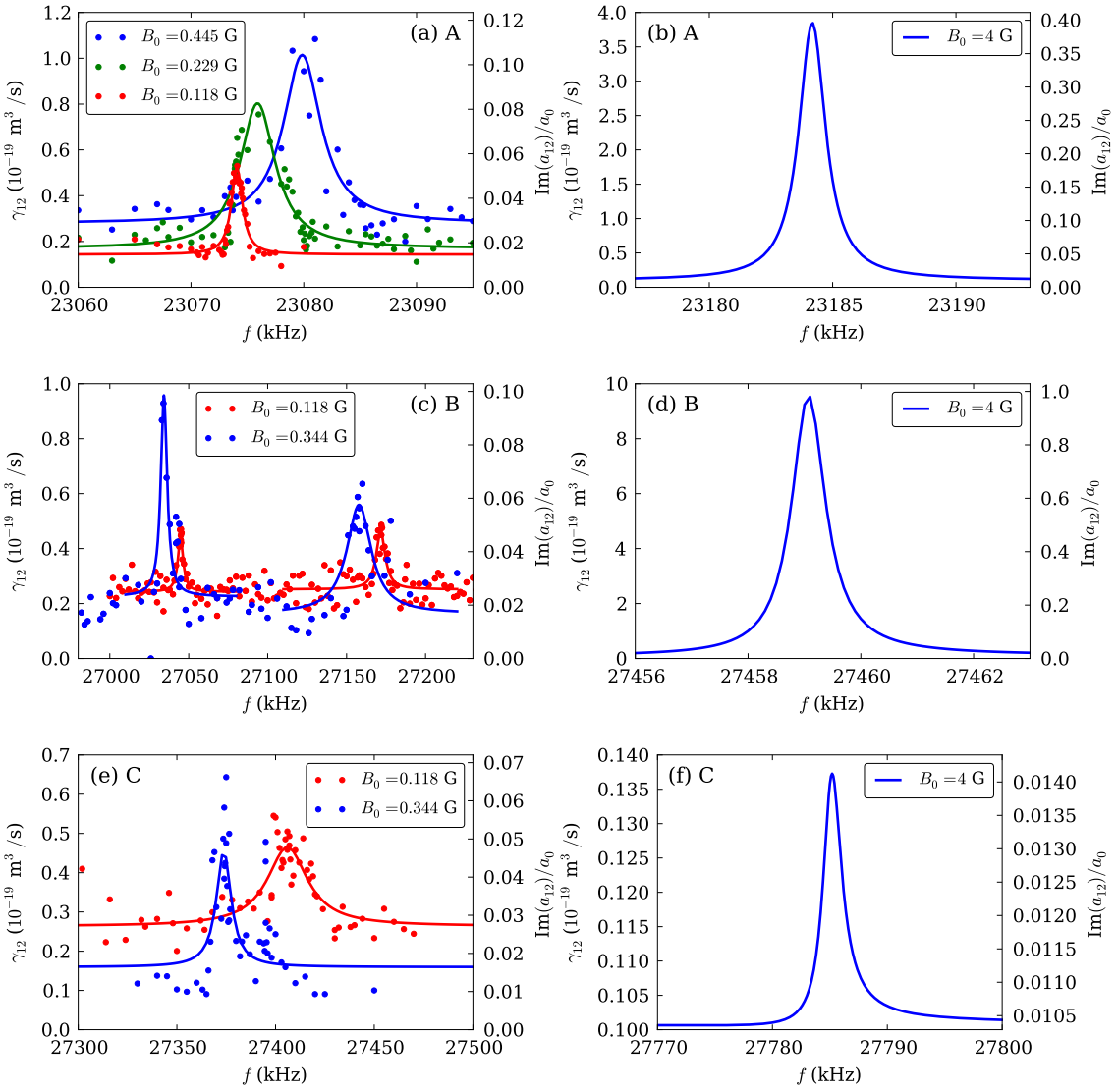

Figure 7.6: RF-induced Feshbach resonances detected with two-body losses. All experimental results are presented in (a) (resonance A), (c) (resonance B) and (e) (resonance C). f is the RF radiation frequency, B_0 is the value of RF magnetic field amplitude. Precise theoretical results calculated at the same bias magnetic field 3.23 G but different RF field amplitude similar to ref. [58] given by T. Tscherbul in private communication for the corresponding resonances are presented in (b) (resonance A), (d) (resonance B) and (f) (resonance C) for comparison. A narrow Feshbach resonance visible on the left side from resonance B (c) is also predicted in the theoretical simulations (Fig. 7.3).

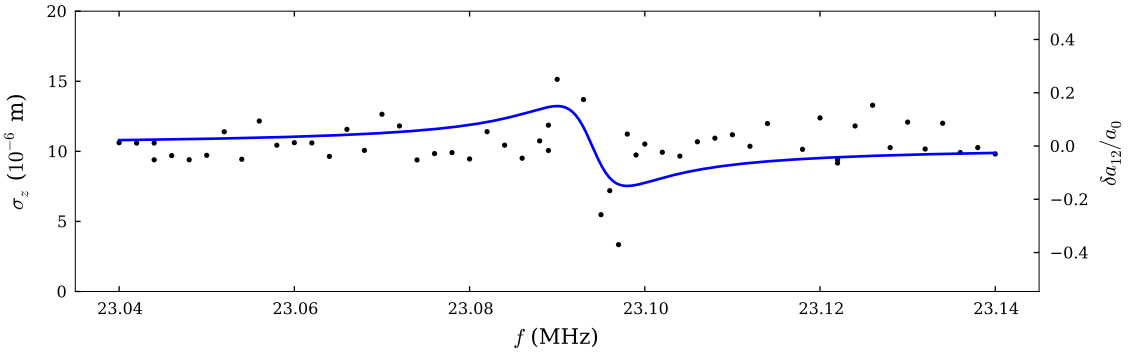

Figure 7.7: Measurement of the change of interspecies scattering length δa_{12} in the vicinity of a Feshbach resonance. The RF field amplitude is 0.89 G. The blue line shows the approximate value of the expected change in scattering length with $\delta b_{\max} = 0.3\, a_0$ and the width of the resonance $\gamma_{ba}/2\hbar = 4$ kHz.

This allows one to estimate the expected changes in $\mathrm{Re}(a_{12})$ resulting from the changes in the loss rate γ_{12}. The maximum change in $\delta\alpha_{\max}$ is expected to be half the maximum change in δb. In other words, the real part of a_{12} in our experiments is changed not more than by $0.03\, a_0$ which is very hard to measure experimentally.

We attempted to detect a change in a_{12} using the collective oscillations technique which is expected to be sensitive to changes in a_{12} by $0.1\, a_0$ in a single shot (Ch. 6, Fig. 6.7). We observe a change in the width of component $|2\rangle$ in a two-component BEC at fixed evolution time $t = 770$ ms and plot it versus the RF radiation frequency, where the RF field amplitude $B_0 = 0.89$ G. As the derivative $\partial\sigma_z/\partial a_{12}$ is negative at this time and the period of the collective oscillations increases with an increase of a_{12} (Fig. 6.3a), an increase in a_{12} increases σ_z. Taking into account $a_0\partial\sigma_z/\partial a_{12} = 19$ μm, we obtain an approximate plot of δa_{12} versus RF frequency (Fig. 7.7). The sign of the changes in a_{12} coincides with theoretical predictions (Fig. 7.3) [58]. The data shows that it is possible to accurately measure δa_{12} near the RF-induced Feshbach resonances provided the experiment is made to be less affected by RF fields of high power.

7.4 Conclusion

In this chapter, we have detected previously predicted RF-induced Feshbach resonances in ^{87}Rb by inelastic losses. The frequencies obtained may allow one to characterize ^{87}Rb interatomic interactions more precisely. Additionally, we have detected signatures of changing the scattering length a_{12} in the vicinity of a Feshbach resonance. Manipulating a_{12} will be useful for spin-squeezing and entanglement experiments.

Chapter 8

Conclusions

In this thesis we described several high-precision measurements using the dynamical evolution of a two-component Bose-Einstein condensate of ^{87}Rb atoms. Interferometric and non-interferometric studies of the dynamics were performed. We observed that the mechanical motion of the BEC components greatly affects the interference contrast leading to periodic dephasing and rephasing. The efficiency of the rephasing was enhanced by synchronous application of a spin echo which allowed us to obtain a coherence time of 2.8 s, the longest coherence time observed for an interacting BEC. We demonstrated that periodic collective oscillations in a two-component BEC allowed us to perform precision measurements of the scattering lengths a_{12} and a_{22} in ^{87}Rb, in which the uncertainty of the a_{12} measurement is 0.016%. In order to be able to tune the scattering length a_{12}, we explored the possibility of using RF-induced Feshbach resonances and detected a previously unobserved but theoretically predicted group of RF-induced Feshbach resonances in ^{87}Rb.

In chapter 2, using a variational principle and starting from the mean-field energy functional, we derived an analytical description of a two-component BEC which has fewer atoms in component $|2\rangle$ than in component $|1\rangle$ (1 denotes the component with the larger scattering length). We found that the period of the collective oscillations in a such system depends on the ratio of the interspecies and intraspecies scattering lengths a_{12}/a_{22} and the smallest (axial) trapping frequency f_z, and it does not depend on the scattering length

a_{22} and the total number of atoms. The analytical description well describes the density and phase dynamics of a lossless BEC at evolution times longer than the period of the collective oscillations, predicting a periodic mean-field rephasing effect.

Chapter 3 described and characterized the experimental apparatus used in our experiments where the optical resolution and imaging laser linewidth were improved. It also described the techniques such as dual state imaging which was also improved in this work and fringe removal algorithm used throughout the thesis.

We developed a new, interferometric technique for the calibration of the total atom number in chapter 4. The value of the calibration coefficient ($k = 1.83(4)$) obtained by this technique coincided with the calibration with the condensation temperature. In order to avoid the necessity of using simulations of coupled Gross-Pitaevskii equations, we derived analytics for the interferometric atom number calibration, using the analytical description of the phase dynamics.

Chapter 5 described our discovery that collective oscillations in a two-component BEC induce a mean-field self-rephasing effect, and the interferometric contrast is restored to 60% after 1 s. The contrast was improved even further by applying a spin-echo technique. This allowed us to obtain a contrast of 75% after 1.5 s of evolution and a coherence time of 2.8 s, the longest coherence time reported for an interacting BEC.

In chapter 6 we used the frequency of collective oscillations in a two-component BEC where the number of atoms in state $|2\rangle \equiv |F = 2, m_F = 1\rangle$ was much less than in state $|1\rangle \equiv |F = 1, m_F = -1\rangle$ in order to measure scattering lengths a_{12} and a_{22} relative to a_{11} in ^{87}Rb. Our results $a_{12} = 98.006(16)\, a_0$ and $a_{22} = 95.44(7)\, a_0$ are close to the latest theoretical predictions. We also measured the two-body loss coefficients $\gamma_{12} = 1.51(18) \times 10^{-14}\text{cm}^3/\text{s}$ and $\gamma_{22} = 8.1(3) \times 10^{-14}$ cm^3/s for these states.

Finally, we have detected predicted, previously unobserved RF-induced Feshbach resonances for states $|1\rangle$ and $|2\rangle$ in ^{87}Rb. The positions of these narrow resonances may provide useful information for careful characterisation of model potentials and precise prediction of the scattering properties of ultracold ^{87}Rb atoms. The RF-induced Feshbach resonances may also be used for quick tuning of the inter-species scattering length which

is required for spin-squeezing experiments.

The research performed can be applied in a wide range of future studies. The predicted coherence time of the two-component condensate that can be obtained in rephasing experiments is 12 s, longer than actually obtained by a factor of 4. This might be limited by the effects of finite temperature ($0 < T \ll T_c$) of the BEC and requires further investigation. Precision measurements of the scattering lengths in ^{87}Rb that take account of finite temperature effects in order to eliminate the systematics can also be performed in future experiments. Precisely measured scattering lengths and two-body loss coefficients can help to find a theoretically predicted, but not yet observed, weak magnetic Feshbach resonance in ^{87}Rb at 2 G. Prospects for using RF-induced Feshbach resonances for tuning inter-atomic interactions and monitoring drifts in fundamental constants can also be studied in the future.

Matter-wave interferometry is a powerful method of precision measurements and a long phase-accumulation time is desirable for improving sensitivity of measurements. Our observations of long coherence time allow to extend phase accumulation times in BEC interferometry. That can be readily applied for precision measurements of AC Stark or AC Zeeman shifts of atomic levels. The latter is particularly interesting as it allows measuring the effects beyond the rotating-wave approximation, such as a Bloch-Siegert shift. Notably, nonlinear dynamics in a BEC interferometer can provide a protocol [118] (not yet present) with super-Heisenberg scaling of the measurement uncertainty which can be used for ultrahigh precision magnetometry.

Bibliography

[1] M. H. Anderson, J. R. Ensher, M. R. Matthews, C. E. Wieman, and E. A. Cornell. Observation of Bose-Einstein condensation in a dilute atomic vapor. *Science*, 269(5221):198–201, 1995.

[2] K. B. Davis, M. O. Mewes, M. R. Andrews, N. J. van Druten, D. S. Durfee, D. M. Kurn, and W. Ketterle. Bose-Einstein condensation in a gas of sodium stoms. *Phys. Rev. Lett.*, 75(22):3969–3973, Nov 1995.

[3] D. E. Pritchard. Cooling neutral atoms in a magnetic trap for precision spectroscopy. *Phys. Rev. Lett.*, 51(15):1336–1339, Oct 1983.

[4] W. Hänsel, P. Hommelhoff, T. W. Hänsch, and J. Reichel. Bose-Einstein condensation on a microelectronic chip. *Nature*, 413(6855):498–501, 2001.

[5] H. Ott, J. Fortagh, G. Schlotterbeck, A. Grossmann, and C. Zimmermann. Bose-Einstein condensation in a surface microtrap. *Phys. Rev. Lett.*, 87(23):230401, Nov 2001.

[6] J. Fortágh and C. Zimmermann. Magnetic microtraps for ultracold atoms. *Rev. Mod. Phys.*, 79(1):235–289, Feb 2007.

[7] D. M. Stamper-Kurn, M. R. Andrews, A. P. Chikkatur, S. Inouye, H.-J. Miesner, J. Stenger, and W. Ketterle. Optical confinement of a Bose-Einstein condensate. *Phys. Rev. Lett.*, 80(10):2027–2030, Mar 1998.

[8] S. Doret, Colin Connolly, Wolfgang Ketterle, and John Doyle. Buffer-Gas cooled Bose-Einstein condensate. *Physical Review Letters*, 103(10):103005, September 2009.

[9] C. J. Pethick and H. Smith. *Bose-Einstein condensation in dilute gases*. Cambridge, 2008.

[10] L. Pitaevskii and S. Stringari. *Bose-Einstein condensation*. Oxford University Press, 2003.

[11] S. Stringari. Collective excitations of a trapped Bose-condensed gas. *Physical Review Letters*, 77(12):2360, 1996.

[12] S. Burger, K. Bongs, S. Dettmer, W. Ertmer, K. Sengstock, A. Sanpera, G. V. Shlyapnikov, and M. Lewenstein. Dark solitons in Bose-Einstein condensates. *Phys. Rev. Lett.*, 83(25):5198–5201, Dec 1999.

[13] L. Khaykovich, F. Schreck, G. Ferrari, T. Bourdel, J. Cubizolles, L. D. Carr, Y. Castin, and C. Salomon. Formation of a matter-wave bright soliton. *Science*, 296(5571):1290–1293, 2002.

[14] C. J. Myatt, E. A. Burt, R. W. Ghrist, E. A. Cornell, and C. E. Wieman. Production of two overlapping Bose-Einstein condensates by sympathetic cooling. *Phys. Rev. Lett.*, 78(4):586–589, Jan 1997.

[15] M. R. Matthews, D. S. Hall, D. S. Jin, J. R. Ensher, C. E. Wieman, E. A. Cornell, F. Dalfovo, C. Minniti, and S. Stringari. Dynamical response of a Bose-Einstein condensate to a discontinuous change in internal state. *Phys. Rev. Lett.*, 81(2):243–247, Jul 1998.

[16] Yu. Kagan, E. L. Surkov, and G. V. Shlyapnikov. Evolution and global collapse of trapped Bose condensates under variations of the scattering length. *Phys. Rev. Lett.*, 79(14):2604–2607, Oct 1997.

[17] D. S. Hall, M. R. Matthews, J. R. Ensher, C. E. Wieman, and E. A. Cornell. Dynamics of component separation in a binary mixture of Bose-Einstein condensates. *Phys. Rev. Lett.*, 81(8):1539–1542, Aug 1998.

[18] A. Sinatra, P. O. Fedichev, Y. Castin, J. Dalibard, and G. V. Shlyapnikov. Dynamics of two interacting Bose-Einstein condensates. *Phys. Rev. Lett.*, 82(2):251–254, Jan 1999.

[19] K. M. Mertes, J. W. Merrill, R. Carretero-González, D. J. Frantzeskakis, P. G. Kevrekidis, and D. S. Hall. Nonequilibrium dynamics and superfluid ring excitations in binary Bose-Einstein condensates. *Phys. Rev. Lett.*, 99(19):190402, Nov 2007.

[20] D. S. Hall, M. R. Matthews, C. E. Wieman, and E. A. Cornell. Measurements of relative phase in two-component Bose-Einstein condensates. *Phys. Rev. Lett.*, 81(8):1543–1546, Aug 1998.

[21] D. M. Harber, H. J. Lewandowski, J. M. McGuirk, and E. A. Cornell. Effect of cold collisions on spin coherence and resonance shifts in a magnetically trapped ultracold gas. *Phys. Rev. A*, 66(5):053616, 2002.

[22] R. P. Anderson, C. Ticknor, A. I. Sidorov, and B. V. Hall. Spatially inhomogeneous phase evolution of a two-component Bose-Einstein condensate. *Phys. Rev. A*, 80(2):023603, 2009.

[23] G.-B. Jo, Y. Shin, S. Will, T. A. Pasquini, M. Saba, W. Ketterle, D. E. Pritchard, M. Vengalattore, and M. Prentiss. Long phase coherence time and number squeezing of two Bose-Einstein condensates on an atom chip. *Phys. Rev. Lett.*, 98(3):030407, Jan 2007.

[24] H. J. Lewandowski, J. M. McGuirk, D. M. Harber, and E. A. Cornell. Decoherence-driven cooling of a degenerate spinor Bose gas. *Phys. Rev. Lett.*, 91(24):240404, 2003.

[25] P. Treutlein, P. Hommelhoff, T. Steinmetz, T. W. Hänsch, and J. Reichel. Coherence in microchip traps. *Phys. Rev. Lett.*, 92(20):203005, May 2004.

[26] M. Gustavsson, E. Haller, M. J. Mark, J. G. Danzl, G. Rojas-Kopeinig, and H.-C. Nägerl. Control of interaction-induced dephasing of Bloch oscillations. *Phys. Rev. Lett.*, 100(8):080404, 2008.

[27] C. Deutsch, F. Ramirez-Martinez, C. Lacroûte, F. Reinhard, T. Schneider, J. Fuchs, F. Piéchon, F. Laloë, J. Reichel, and P. Rosenbusch. Spin self-rephasing and very long coherence times in a trapped atomic ensemble. *Phys. Rev. Lett.*, 105(2):020401, 2010.

[28] E. L. Hahn. Spin echoes. *Phys. Rev.*, 80(4):580–594, Nov 1950.

[29] B. Opanchuk, M. Egorov, S. Hoffmann, A. I. Sidorov, and P. D. Drummond. Quantum noise in three-dimensional BEC interferometry. arXiv:1105.5493 (2011).

[30] A. Sinatra, Y. Castin, and E. Witkowska. Coherence time of a Bose-Einstein condensate. *Phys. Rev. A*, 80(3):033614, Sep 2009.

[31] M. Egorov, R. P. Anderson, V. Ivannikov, B. Opanchuk, P. Drummond, B. V. Hall, and A. I. Sidorov. Long-lived periodic revivals of coherence in an interacting Bose-Einstein condensate. *Phys. Rev. A*, 84(2):021605(R), Aug 2011.

[32] M. R. Matthews, B. P. Anderson, P. C. Haljan, D. S. Hall, M. J. Holland, J. E. Williams, C. E. Wieman, and E. A. Cornell. Watching a superfluid untwist itself: recurrence of Rabi oscillations in a Bose-Einstein condensate. *Phys. Rev. Lett.*, 83(17):3358–3361, 1999.

[33] N. R. Newbury, C. J. Myatt, and C. E. Wieman. s -wave elastic collisions between cold ground-state ^{87}Rb atoms. *Phys. Rev. A*, 51(4):R2680–R2683, Apr 1995.

[34] J. M. Vogels, C. C. Tsai, R. S. Freeland, S. J. J. M. F. Kokkelmans, B. J. Verhaar, and D. J. Heinzen. Prediction of Feshbach resonances in collisions of ultracold rubidium atoms. *Phys. Rev. A*, 56(2):R1067–R1070, Aug 1997.

[35] E. G. M. van Kempen, S. J. J. M. F. Kokkelmans, D. J. Heinzen, and B. J. Verhaar. Interisotope determination of ultracold rubidium interactions from three high-precision experiments. *Phys. Rev. Lett.*, 88(9):093201, Feb 2002.

[36] Roahn Wynar, R. S. Freeland, D. J. Han, C. Ryu, and D. J. Heinzen. Molecules in a Bose-Einstein condensate. *Science*, 287(5455):1016–1019, 2000.

[37] J. L. Roberts, James P. Burke, N. R. Claussen, S. L. Cornish, E. A. Donley, and C. E. Wieman. Improved characterization of elastic scattering near a Feshbach resonance in ^{85}Rb. *Phys. Rev. A*, 64(2):024702, Jul 2001.

[38] J. Y. Seto, R. J. Le Roy, J. Vergès, and C. Amiot. Direct potential fit analysis of the X $^1\Sigma_g{}^+$ state of Rb_2: Nothing else will do! *J. Chem. Phys.*, 113(8):3067–3076, August 2000.

[39] A. Widera, F. Gerbier, S. Fölling, T. Gericke, O. Mandel, and I. Bloch. Precision measurement of spin-dependent interaction strengths for spin-1 and spin-2 ^{87}Rb atoms. *New J. Phys.*, 8(8):152, 2006.

[40] B. J. Verhaar, E. G. M. van Kempen, and S. J. J. M. F. Kokkelmans. Predicting scattering properties of ultracold atoms: Adiabatic accumulated phase method and mass scaling. *Phys. Rev. A*, 79(3):032711, 2009.

[41] S. J. J. M. F. Kokkelmans, private communication (June 2010).

[42] S. Tojo, Y. Taguchi, Y. Masuyama, T. Hayashi, H. Saito, and T. Hirano. Controlling phase separation of binary Bose-Einstein condensates via mixed-spin-channel Feshbach resonance. *Phys. Rev. A*, 82(3):033609, Sep 2010.

[43] S. Tojo, T. Hayashi, T. Tanabe, T. Hirano, Y. Kawaguchi, H. Saito, and M. Ueda. Spin-dependent inelastic collisions in spin-2 Bose-Einstein condensates. *Phys. Rev. A*, 80(4):042704, Oct 2009.

[44] A. Sinatra and Y. Castin. Binary mixtures of Bose-Einstein condensates: phase dynamics and spatial dynamics. *Eur. Phys. J. D*, 8(3):319–332, 2000.

[45] C. Chin and V. Flambaum. Enhanced sensitivity to fundamental constants in ultracold atomic and molecular systems near Feshbach resonances. *Phys. Rev. Lett.*, 96(23):230801, 2006.

[46] G. Reinaudi, T. Lahaye, Z. Wang, and D. Guéry-Odelin. Strong saturation absorption imaging of dense clouds of ultracold atoms. *Optics Letters*, 32(21):3143, 2007.

[47] M. F. Riedel, P. Böhi, Y. Li, T. W. Hänsch, A. Sinatra, and P. Treutlein. Atom-chip-based generation of entanglement for quantum metrology. *Nature Phys.*, 464(7292):1170–1173, 2010.

[48] C. Gross, T. Zibold, E. Nicklas, J. Estève, and M. K. Oberthaler. Nonlinear atom interferometer surpasses classical precision limit. *Nature*, 464(7292):1165–1169, 2010.

[49] J. Szczepkowski, R. Gartman, M. Witkowski, L. Tracewski, M. Zawada, and W. Gawlik. Analysis and calibration of absorptive images of Bose-Einstein condensate at nonzero temperatures. *Rev. Sci. Instrum.*, 80(053103), 2009.

[50] D. Döring, G. McDonald, J. E. Debs, C. Figl, P. A. Altin, H.-A. Bachor, N. P. Robins, and J. D. Close. Quantum-projection-noise-limited interferometry with coherent atoms in a ramsey-type setup. *Phys. Rev. A*, 81(4):043633, Apr 2010.

[51] M. Kitagawa and M. Ueda. Squeezed spin states. *Phys. Rev. A*, 47(6):5138–5143, Jun 1993.

[52] S. Dimopoulos, P. W. Graham, J. M. Hogan, M. A. Kasevich, and S. Rajendran. Atomic gravitational wave interferometric sensor. *Phys. Rev. D*, 78(12):122002, Dec 2008.

[53] Y. C. Liu, Z. F. Xu, G. R. Jin, and L. You. Spin squeezing: Transforming one-axis twisting into two-axis twisting. *Phys. Rev. Lett.*, 107(1):013601, Jun 2011.

[54] E. Tiesinga, B. J. Verhaar, and H. T. C. Stoof. Threshold and resonance phenomena in ultracold ground-state collisions. *Phys. Rev. A*, 47(5):4114–4122, May 1993.

[55] S. Inouye, M. R. Andrews, J. Stenger, H.-J. Miesner, D. M. Stamper-Kurn, and W. Ketterle. Observation of Feshbach resonances in a Bose-Einstein condensate. *Nature*, 392:151–154, 1998.

[56] F. K. Fatemi, K. M. Jones, and P. D. Lett. Observation of optically induced Feshbach resonances in collisions of cold atoms. *Phys. Rev. Lett.*, 85(21):4462–4465, Nov 2000.

[57] D. J. Papoular, G. V. Shlyapnikov, and J. Dalibard. Microwave-induced Fano-Feshbach resonances. *Phys. Rev. A*, 81(4):041603(R), 2010.

[58] T. V. Tscherbul, T. Calarco, I. Lesanovsky, R. V. Krems, A. Dalgarno, and J. Schmiedmayer. RF-field-induced Feshbach resonances. *Physical Review A*, 81(5):050701, 2010.

[59] A. Kaufman, R. Anderson, Thomas Hanna, E. Tiesinga, P. Julienne, and D. Hall. Radio-frequency dressing of multiple Feshbach resonances. *Physical Review A*, 80(5), 2009.

[60] Y-J Lin, K Jiménez-García, and I B Spielman. Spin-orbit-coupled Bose-Einstein condensates. *Nature*, 471(7336):83–6, 2011.

[61] Y. Kawaguchi, H. Saito, and M. Ueda. Can spinor dipolar effects be observed in Bose-Einstein condensates? *Phys. Rev. Lett.*, 98(11):110406, Mar 2007.

[62] M. Vengalattore, J. Guzman, S. R. Leslie, F. Serwane, and D. M. Stamper-Kurn. Periodic spin textures in a degenerate $F = 1$ ^{87}Rb spinor Bose gas. *Phys. Rev. A*, 81(5):053612, May 2010.

[63] D. M. Weld, H. Miyake, P. Medley, D. E. Pritchard, and W. Ketterle. Thermometry and refrigeration in a two-component Mott insulator of ultracold atoms. *Phys. Rev. A*, 82(5):051603, Nov 2010.

[64] R.P. Anderson. *Non-equilibrium dynamics and relative phase evolution of two-component Bose-Einstein condensates.* PhD thesis, Swinburne university of technology, Melbourne, Australia, 2009.

[65] M. Erhard. *Experimente mit mehrkomponentigen Bose-Einstein-Kondensaten*. PhD thesis, Universität Hamburg, Hamburg, Germany, 2004.

[66] Y. Li, P. Treutlein, J. Reichel, and A. Sinatra. Spin squeezing in a bimodal condensate: spatial dynamics and particle losses. *The European Physical Journal B*, 68(3):365, 2009.

[67] B. D. Esry, Chris H. Greene, James P. Burke, Jr., and John L. Bohn. Hartree-Fock Theory for Double Condensates. *Phys. Rev. Lett.*, 78(19):3594–3597, May 1997.

[68] H. Pu and N. P. Bigelow. Properties of two-species Bose condensates. *Phys. Rev. Lett.*, 80(6):1130–1133, 1998.

[69] M. R. Andrews, D. M. Kurn, H.-J. Miesner, D. S. Durfee, C. G. Townsend, S. Inouye, and W. Ketterle. Propagation of sound in a Bose-Einstein condensate. *Phys. Rev. Lett.*, 79(4):553–556, Jul 1997.

[70] L. Salasnich, A. Parola, and L. Reatto. Effective wave equations for the dynamics of cigar-shaped and disk-shaped Bose condensates. *Physical Review A*, 65(4):043614, 2002.

[71] Z. Dutton and C. W. Clark. Effective one-component description of two-component Bose-Einstein condensate dynamics. *Phys. Rev. A*, 71(6):063618, 2005.

[72] A. Görlitz, J. M. Vogels, A. E. Leanhardt, C. Raman, T. L. Gustavson, J. R. Abo-Shaeer, A. P. Chikkatur, S. Gupta, S. Inouye, T. Rosenband, and W. Ketterle. Realization of Bose-Einstein condensates in lower dimensions. *Phys. Rev. Lett.*, 87(13):130402, Sep 2001.

[73] D. S. Petrov, G. V. Shlyapnikov, and J. T. M. Walraven. Regimes of quantum degeneracy in trapped 1D gases. *Phys. Rev. Lett.*, 85(18):3745–3749, Oct 2000.

[74] P. Massignan and M. Modugno. One-dimensional model for the dynamics and expansion of elongated Bose-Einstein condensates. *Phys. Rev. A*, 67(2):023614, Feb 2003.

[75] A. Kamchatnov and V. Shchesnovich. Dynamics of Bose-Einstein condensates in cigar-shaped traps. *Phys. Rev. A*, 70(2):023604, 2004.

[76] L. Young-S., L. Salasnich, and S. Adhikari. Dimensional reduction of a binary Bose-Einstein condensate in mixed dimensions. *Phys. Rev. A*, 82(5):053601, 2010.

[77] V. M. Pérez-García, H. Michinel, J. I. Cirac, M. Lewenstein, and P. Zoller. Low energy excitations of a Bose-Einstein condensate: a time-dependent variational analysis. *Phys. Rev. Lett.*, 77(27):5320–5323, Dec 1996.

[78] S. Whitlock. *Bose-Einstein condensates on a magnetic film atom chip*. PhD thesis, Swinburne university of technology, Melbourne, Australia, 2007.

[79] C. F. Ockeloen, A. F. Tauschinsky, R. J. C. Spreeuw, and S. Whitlock. Detection of small atom numbers through image processing. *Phys. Rev. A*, 82:061606, Dec 2010.

[80] B. V. Hall, S. Whitlock, F. Scharnberg, P. Hannaford, and A. Sidorov. A permanent magnetic film atom chip for Bose-Einstein condensation. *J. Phys. B*, 39(1):27, 2006.

[81] M. Olshanii. Atomic scattering in the presence of an external confinement and a gas of impenetrable bosons. *Phys. Rev. Lett.*, 81(5):938–941, 1998.

[82] S.-G. Peng, H. Hu, X.-J. Liu, and P. D. Drummond. Confinement-induced resonances in anharmonic waveguides. *Phys. Rev. A*, 84:043619, Oct 2011.

[83] C. G. Gray, G. Karl, and V. A. Novikov. Direct use of variational principles as an approximation technique in classical mechanics. *Am. J. Phys.*, 64(9):1177–1184, September 1996.

[84] L. Landau. *Mechanics*. Pergamon Press, Oxford New York, 1976.

[85] D. A. Steck. Rubidium 87 D line data, 2003.

[86] G. Breit and I. I. Rabi. Measurement of nuclear spin. *Phys. Rev.*, 38(11):2082–2083, 1931.

[87] W. Ketterle and N. J. van Druten. Bose-Einstein condensation of a finite number of particles trapped in one or three dimensions. *Phys. Rev. A*, 54(1):656–660, Jul 1996.

[88] S. Giorgini, L. P. Pitaevskii, and S. Stringari. Condensate fraction and critical temperature of a trapped interacting Bose gas. *Phys. Rev. A*, 54(6):R4633–R4636, Dec 1996.

[89] R. Smith, R. Campbell, N. Tammuz, and Z. Hadzibabic. Effects of interactions on the critical temperature of a trapped Bose gas. *Phys. Rev. Lett.*, 106(25):250403, 2011.

[90] M. Houbiers, H. T. C. Stoof, and E. A. Cornell. Critical temperature of a trapped Bose gas: mean-field theory and fluctuations. *Phys. Rev. A*, 56(3):2041–2045, Sep 1997.

[91] M. Holzmann, W. Krauth, and M. Naraschewski. Precision Monte Carlo test of the Hartree-Fock approximation for a trapped Bose gas. *Phys. Rev. A*, 59(4):2956–2961, Apr 1999.

[92] P. Arnold and B. Tomášik. T_c for trapped dilute Bose gases: A second-order result. *Phys. Rev. A*, 64(5):053609, Oct 2001.

[93] M. J. Davis and P. B. Blakie. Critical temperature of a trapped Bose gas: comparison of theory and experiment. *Phys. Rev. Lett.*, 96(6):060404, Feb 2006.

[94] O. Zobay. Phase transition of trapped interacting Bose gases. *Laser Physics*, 19(4):700–724, 2009.

[95] W. Ketterle, D.S. Durfee, and D.M. Stamper-Kurn. *Making, probing and understanding Bose-Einstein condensates*. IOS Press, Amsterdam, 1999. In Bose-Einstein condensation in atomic gases, Proceedings of the International School of Physics "Enrico Fermi", Course CXL, edited by M. Inguscio, S. Stringari and C.E. Wieman.

[96] F. Gerbier, J. H. Thywissen, S. Richard, M. Hugbart, P. Bouyer, and A. Aspect. Experimental study of the thermodynamics of an interacting trapped Bose-Einstein condensed gas. *Phys. Rev. A*, 70(1):013607, 2004.

[97] R. P. Smith, N. Tammuz, R. L. D. Campbell, M. Holzmann, and Z. Hadzibabic. Condensed fraction of an atomic Bose gas induced by critical correlations. *Phys. Rev. Lett.*, 107(19):190403, Nov 2011.

[98] P. R. Berman. *Atom Interferometry*. Academic Press, San Diego, 1997.

[99] A. D. Cronin, J. Schmiedmayer, and D. E. Pritchard. Optics and interferometry with atoms and molecules. *Rev. Mod. Phys.*, 81(3):1051–1129, 2009.

[100] J. Grond, U. Hohenester, I. Mazets, and J. Schmiedmayer. Atom interferometry with trapped Bose-Einstein condensates: impact of atom-atom interactions. *New J. Phys.*, 12(6):065036, 2010.

[101] T. Schumm, S. Hofferberth, L. M. Andersson, S. Wildermuth, S. Groth, I. Bar-Joseph, J. Schmiedmayer, and P. Krüger. Matter-wave interferometry in a double well on an atom chip. *Nature Phys.*, 1:57–62, 2005.

[102] G.-B. Jo, Y. Shin, S. Will, T. A. Pasquini, M. Saba, W. Ketterle, D. E. Pritchard, M. Vengalattore, and M. Prentiss. Long phase coherence time and number squeezing of two Bose-Einstein condensates on an atom chip. *Phys. Rev. Lett.*, 98(3):030407, 2007.

[103] M. Lewenstein and L. You. Quantum phase diffusion of a Bose-Einstein condensate. *Phys. Rev. Lett.*, 77(17):3489–3493, Oct 1996.

[104] M. Gustavsson, E. Haller, M. J. Mark, J. G. Danzl, R. Hart, A. J. Daley, and H.-C. Nägerl. Interference of interacting matter waves. *New J. Phys.*, 12(6):065029, 2010.

[105] Y. Li, Y. Castin, and A. Sinatra. Optimum spin squeezing in Bose-Einstein condensates with particle losses. *Phys. Rev. Lett.*, 100(21):210401, May 2008.

[106] G. Kleine Büning, J. Will, W. Ertmer, E. Rasel, J. Arlt, C. Klempt, F. Ramirez-Martinez, F. Piéchon, and P. Rosenbusch. Extended coherence time on the clock transition of optically trapped rubidium. *Phys. Rev. Lett.*, 106(24):240801, Jun 2011.

[107] M. F. Andersen, A. Kaplan, and N. Davidson. Echo spectroscopy and quantum stability of trapped atoms. *Phys. Rev. Lett.*, 90(2):023001, 2003.

[108] D. Oblak, J. Appel, P. J. Windpassinger, U. B. Hoff, N. Kjærgaard, and E. S. Polzik. Echo spectroscopy of atomic dynamics in a Gaussian trap via phase imprints. *Eur. Phys. J. D*, 50(1):67–73, 2008.

[109] P. A. Altin, G. McDonald, D. Döring, J. E. Debs, T. H. Barter, J. D. Close, N. P. Robins, S. A. Haine, T. M. Hanna, and R. P. Anderson. Optically trapped atom interferometry using the clock transition of large ^{87}Rb Bose-Einstein condensates. *New J. Phys.*, 13(6):065020, 2011.

[110] A. Sinatra, E. Witkowska, J.-C. Dornstetter, Y. Li, and Y. Castin. Limit of spin squeezing in finite-temperature Bose-Einstein condensates. *Phys. Rev. Lett.*, 107(6):060404, Aug 2011.

[111] M. J. Steel and M. J. Collett. Quantum state of two trapped Bose-Einstein condensates with a Josephson coupling. *Phys. Rev. A*, 57(4):2920–2930, Apr 1998.

[112] J. Merrill. Characterization of inelastic losses from Bose-Einstein condensates in the $|2, 1\rangle$ state of ^{87}Rb. Bachelor thesis, 2006. Amherst College.

[113] O. V. Sinkin, R. Holzlöhner, J. Zweck, and C. R. Menyuk. Optimization of the split-step Fourier method in modeling optical-fiber communications systems. *J. Lightw. Techn.*, 21(1):61–68, 2003.

[114] B. Opanchuk. https://github.com/Manticore/beclab. Simulator of two-component BEC dynamics by solving coupled GPE equations or using truncated Wigner approximation.

[115] W. J. Marciano. Time variation of the fundamental "constants" and Kaluza-Klein theories. *Phys. Rev. Lett.*, 52(7):489–491, Feb 1984.

[116] R. A. Hart, X. Xu, R. Legere, and K. Gibble. A quantum scattering interferometer. *Nature*, 446(7138):892–5, 2007.

[117] P. Treutlein, T. W. Hänsch, J. Reichel, A. Negretti, M. A. Cirone, and T. Calarco. Microwave potentials and optimal control for robust quantum gates on an atom chip. *Phys. Rev. A*, 74(2):022312, Aug 2006.

[118] Sergio Boixo, Animesh Datta, Matthew Davis, Steven Flammia, Anil Shaji, and Carlton Caves. Quantum metrology: Dynamics versus entanglement. *Physical Review Letters*, 101(4):040403, July 2008.

Publications of the author

M. Egorov, R. P. Anderson, V. Ivannikov, B. Opanchuk, P. Drummond, B. V. Hall, and A. I. Sidorov. Long-lived periodic revivals of coherence in an interacting Bose-Einstein condensate. *Phys. Rev. A*, 84(2):021605(R), Aug 2011.

B. Opanchuk, M. Egorov, S. Hoffmann, A. Sidorov, and P. Drummond. Quantum noise in three-dimensional BEC interferometry. *In press*, arXiv:1105.5493, 2011.